ETH zürich

André Ludwig

Attosecond and Strong-Field Ionization Dynamics in Atoms and Molecules

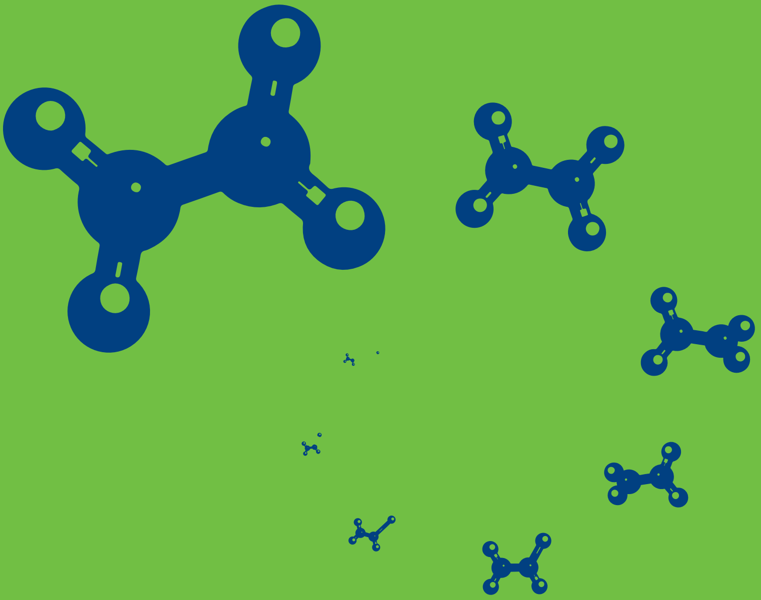

Diss. ETH No. 23279

DISS. ETH NO. 23279

ATTOSECOND AND STRONG-FIELD IONIZATION DYNAMICS IN ATOMS AND MOLECULES

A thesis submitted to attain the degree of

DOCTOR OF SCIENCES of ETH ZURICH

(Dr. sc. ETH Zurich)

presented by

ANDRE LUDWIG

Dipl.-Phys., Philipps-Universität Marburg

born on 07.02.1985

citizen of Germany

accepted on the recommendation of

Prof. Dr. Ursula Keller, examiner
Prof. Dr. Thomas Pfeifer, co-examiner
PD Dr. Lukas Gallmann, co-examiner

2016

Contents

List of Figures

List of Symbols and Acronyms

Symbols

$\boldsymbol{A}$	vector potential
$\boldsymbol{B}$	magnetic field
c	speed of light in vacuum
$\boldsymbol{E}$	electric field
γ	Keldysh parameter
I	intensity of electromagnetic field
I_0	peak intensity of electromagnetic field
I_p	ionization potential
$\boldsymbol{k}$	wave vector
n	refractive index
$\boldsymbol{p}$	electron momentum
φ_CEP	carrier envelope phase
τ_FWHM	full width at half maximum duration
U_p	ponderomotive energy
ω	angular frequency
W	ionization rate

Acronyms

AIMS	ab initio multiple spawning
AOM	acousto-optic modulator
AOPDF	acousto-optic programmable dispersive filter
AP	attosecond pulse
APPLN	aperiodic periodically poled lithium niobate
APT	attosecond pulse train
ATAS	attosecond transient absorption spectroscopy
ATI	above-threshold ionization
CCD	charge-coupled device
CEP	carrier-envelope phase
CMA	central momentum approximation
COM	center of mass
CPA	chirped pulse amplification
CTMC	classical trajectory Monte Carlo
cw	continuous wave
DOG	double optical gating
DPSSL	diode-pumped solid-state laser
EMG	exponentially modified Gaussian function
ePIE	extended ptychographic iterative engine
EWP	electron wave packet
FROG	frequency-resolved optical gating
FROG-CRAB	frequency-resolved optical gating for complete reconstruction of attosecond bursts
FWHM	full width at half maximum
GD	group delay
GDD	group delay dispersion
HH	high-order harmonic
HHG	high-order harmonic generation
IR	infrared
KLM	Kerr lens mode-locking

LSGPA	least-squares generalized projections algorithm
MCP	micro-channel plate
MIR	mid-infrared
NIR	near-infrared
OPA	optical parametric amplification
OPCPA	optical parametric chirped pulse amplification
PCGPA	principal component generalized projections algorithm
PG	polarization gating
PMD	photoelectron momentum distribution
PPLN	periodically poled lithium niobate
QB	quantum beat
QPM	quasi-phase matching
RABBITT	reconstruction of attosecond beating by interference of two-photon transitions
SAP	single attosecond pulse
SESAM	semiconductor saturable absorber mirror
SHG	second-harmonic generation
SNR	signal-to-noise ratio
SPIDER	spectral phase interferometry for direct electric-field reconstruction
SPM	self-phase modulation
SRSI	self-referenced spectral interferometry
TDSE	time-dependent Schrödinger equation
TOD	third-order dispersion
TOF	time-of-flight spectrometer
UHV	ultra-high vacuum
VMIS	velocity map imaging spectrometer
VUV	vacuum ultraviolet
XUV	extreme ultraviolet

Publications

Parts of this thesis are published in the following journal and conference papers.

Journal Papers

1. L. Gallmann, J. Herrmann, R. Locher, M. Sabbar, A. Ludwig, M. Lucchini, and U. Keller, Invited Article: “Resolving Intra-Atomic Electron Dynamics with Attosecond Transient Absorption Spectroscopy,” Mol. Phys. 111 (14-15), 2243 (2013)

2. R. Boge, C. Cirelli, A. S. Landsman, S. Heuser, A. Ludwig, J. Maurer, M. Weger, L. Gallmann, and U. Keller, “Probing Nonadiabatic Effects in Strong-Field Tunnel Ionization,” Phys. Rev. Lett. 111 (10), 103003 (2013)

3. M. Weger, J. Maurer, A. Ludwig, L. Gallmann, and U. Keller, “Transferring the Attoclock Technique to Velocity Map Imaging,” Opt. Express 21 (19), 21981 (2013)

4. M. Lucchini, J. Herrmann, A. Ludwig, R. Locher, M. Sabbar, L. Gallmann, and U. Keller, “Role of Electron Wavepacket Interference in the Optical Response of Helium Atoms,” New J. Phys. 15 (10), 103010 (2013)

5. R. Locher, M. Lucchini, J. Herrmann, M. Sabbar, M. Weger, A. Ludwig, L. Castiglioni, M. Greif, M. Hengsberger, L. Gallmann, and U. Keller, “Versatile Attosecond Beamline in a Two-Foci Configuration for Simultaneous Time-Resolved Measurements,” Rev. Sci. Instrum. 85 (1), 013113 (2014)

6. A. S. Landsman, M. Weger, J. Maurer, R. Boge, A. Ludwig, S. Heuser, C. Cirelli, L. Gallmann, and U. Keller, “Ultrafast Resolution of Tunneling Delay Time,” Optica 1 (5), 343 (2014)

7. A. Ludwig, J. Maurer, B. W. Mayer, C. R. Phillips, L. Gallmann, and U. Keller, "Breakdown of the Dipole Approximation in Strong-Field Ionization," Phys. Rev. Lett. 113 (24), 243001 (2014)
8. J. Herrmann, M. Lucchini, S. Chen, M. Wu, A. Ludwig, L. Kasmi, K. J. Schafer, L. Gallmann, M. B. Gaarde, and U. Keller, "Multiphoton Transitions for Delay-Zero Calibration in Attosecond Spectroscopy," New J. Phys. 17 (1), 013007 (2015)
9. M. Lucchini, A. Ludwig, L. Kasmi, L. Gallmann, and U. Keller, "Semi-Classical Approach to Compute RABBITT Traces in Multi-Dimensional Complex Field Distributions," Opt. Express 23 (7), 8867 (2015)
10. M. Lucchini, A. Ludwig, T. Zimmermann, L. Kasmi, J. Herrmann, A. Scrinzi, A. S. Landsman, L. Gallmann, and U. Keller, "Anisotropic Emission in Quantum Beat Spectroscopy of Helium Excited States," Phys. Rev. A 91 (6), 063406 (2015)
11. M. Lucchini, L. Castiglioni, L. Kasmi, P. Kliuiev, A. Ludwig, M. Greif, J. Osterwalder, M. Hengsberger, L. Gallmann, and U. Keller, "Light-Matter Interaction at Surfaces in the Spatiotemporal Limit of Macroscopic Models," Phys. Rev. Lett. 115 (13), 137401 (2015)
12. M. Lucchini, M. H. Brügmann, A. Ludwig, L. Gallmann, U. Keller, and T. Feurer, "Ptychographic Reconstruction of Attosecond Pulses," Opt. Express 23 (23), 29502 (2015)
13. A. Ludwig, M. Lucchini, E. Liberatore, J. Herrmann, L. Kasmi, L. Gallmann, U. Rothlisberger, and U. Keller, "Ultrafast Fragmentation Dynamics of Ethylene Cation $C_2H_4^+$," in preparation
14. A. Ludwig, M. Lucchini, L. Kasmi, M. Volkov, L. Gallmann, and U. Keller, "Gouy Phase Shift in Attosecond Ionization Time Measurements," in preparation
15. M. Lucchini, S. A. Sato, J. Herrmann, A. Ludwig, M. Volkov, L. Kasmi, K. Yabana, Y. Shinohara, L. Gallmann, and U. Keller, "Direct Observation of Sub-Cycle Electron Dynamics in Polycrystalline Diamond," in preparation

Conference Papers

1. A. Ludwig, J. Herrmann, M. Sabbar, R. Locher, M. Weger, M. Lucchini, L. Gallmann, and U. Keller, “High Harmonic Generation and Attoscience” — Poster (Best Poster Award), *Summer School of Ultrafast Laser Science and Applications (SSCS)*, Menorca, Spain, June 10–15, 2012
2. A. Ludwig, M. Weger, J. Maurer, L. Gallmann, and U. Keller, “Attoclock Measurements with Velocity Map Imaging Spectrometer” — Poster, *National Centres of Competence in Research: Molecular Ultrafast Science and Technology (NCCR MUST) Annual Meeting*, Engelberg, Switzerland, January 8–10, 2013
3. M. Lucchini, J. Herrmann, A. Ludwig, M. Sabbar, R. Locher, L. Gallmann, and U. Keller, “Optical response of electron wave-packet interference revisited” — Talk, *Conference on Lasers and Electro-Optics/Europe - European Quantum Electronics Conference (CLEO/Europe - EQEC)*, Munich, Germany, May 12–16, 2013
4. L. Gallmann, A. Landsman, M. Weger, J. Maurer, R. Boge, A. Ludwig, S. Heuser, C. Cirelli, and U. Keller, “Tunneling Time in Ultrafast Science is Real and Probabilistic” — Talk, *Conference on Lasers and Electro-Optics/Europe - European Quantum Electronics Conference (CLEO/Europe - EQEC)*, Munich, Germany, May 12–16, 2013
5. J. Herrmann, M. Lucchini, A. Ludwig, M. Sabbar, R. Locher, L. Gallmann, and U. Keller, “Probing Electron Wave-packet Interference” — Talk, *Conference on Lasers and Electro-Optics (CLEO)*, San Jose, California, USA, June 8–13, 2013
6. J. Maurer, A. Landsman, M. Weger, R. Boge, A. Ludwig, S. Heuser, C. Cirelli, L. Gallmann, and U. Keller, “Tunneling Time in Ultrafast Science is Real and Probabilistic” — Talk, *Conference on Lasers and Electro-Optics (CLEO)*, San Jose, California, USA, June 8–13, 2013
7. A. S. Landsman, J. Maurer, A. Ludwig, C. Cirelli, R. Boge, M. Weger, S. Heuser, L. Gallmann, and U. Keller, “Ultrafast resolution of tunneling time” — Poster, *4th International Conference on Attosecond Physics (ATTO)*, Paris, France, July 8–12, 2013
8. R. Boge, C. Cirelli, A. S. Landsman, S. Heuser, A. Ludwig, J. Maurer, M. Weger, L. Gallmann, and U. Keller, “Probing non-adiabatic effects in srong-field ionization” — Poster, *4th International Conference on Attosecond Physics (ATTO)*, Paris, France, July 8–12, 2013
9. M. Lucchini, J. Herrmann, A. Ludwig, M. Sabbar, R. Locher, L. Gallmann, and U. Keller , “Role of electron wave-packet interference in the optical response of helium” — Poster, *4th International Conference on Attosecond Physics (ATTO)*, Paris, France, July 8–12, 2013
10. A. Ludwig, M. Weger, J. Maurer, R. Boge, S. Heuser, A. Landsman, C. Cirelli, L. Gallmann, and U. Keller, “VMIS attoclock measurements reveal real tunneling time in helium” — Talk, *4th International Conference on Attosecond Physics (ATTO)*, Paris, France, July 8–12, 2013
11. J. Herrmann, A. Ludwig, M. Lucchini, L. Gallmann, and U. Keller, “Multiphoton transitions on attosecond timescale” — Poster, *National Centres of Competence*

in Research: Molecular Ultrafast Science and Technology (NCCR MUST) Annual Meeting, Engelberg, Switzerland, January 8–10, 2014

12. A. Ludwig, M. Lucchini, J. Herrmann, L. Gallmann, and U. Keller, "Extending the attoline towards molecular dynamics" — Poster, *National Centres of Competence in Research: Molecular Ultrafast Science and Technology (NCCR MUST) Annual Meeting*, Engelberg, Switzerland, January 8–10, 2014

13. A. Ludwig, J. Maurer, B. W. Mayer, C. R. Phillips, L. Gallmann, and U. Keller, "Exploring characteristics of strong-field ionization dynamics in the mid-infrared regime" — Poster, *Conference on Lasers and Electro-Optics (CLEO)*, San Jose, California, USA, June 8–13, 2014

14. C. Hofmann, A. S. Landsman, R. Boge, S. Heuser, C. Cirelli, M. Weger, A. Ludwig, J. Maurer, L. Gallmann, and U. Keller, "Studying Momentum Distributions in all Aspects Reveals Important Insight" — Poster, *Conference on Lasers and Electro-Optics (CLEO)*, San Jose, California, USA, June 8–13, 2014

15. L. Gallmann, J. Herrmann, M. Lucchini, S. Chen, M. Wu, A. Ludwig, L. Kasmi, K. J. Schafer, M. B. Gaarde, and U. Keller, "Quarter-Laser-Cycle Oscillations in Attosecond Transient Absorption for Robust Delay Zero Calibration" — Poster, *Conference on Lasers and Electro-Optics (CLEO)*, San Jose, California, USA, June 8–13, 2014

16. J. Maurer, A. Ludwig, B. W. Mayer, C. R. Phillips, L. Gallmann, and U. Keller, "Breakdown of dipole approximation in strong field ionization" — Postdeadline Talk, *Conference on Lasers and Electro-Optics (CLEO)*, San Jose, California, USA, June 8–13, 2014

17. J. Herrmann, M. Lucchini, S. Chen, M. Wu, A. Ludwig, L. Kasmi, K. J. Schafer, L. Gallmann, M. B. Gaarde, and U. Keller, "Multiphoton Transitions for Robust Delay-Zero Calibration in Attosecond Transient Absorption" — Talk, *19th International Conference on Ultrafast Phenomena*, Okinawa, Japan, July 7–11, 2014

18. C. Hofmann, A. S. Landsman, R. Boge, S. Heuser, C. Cirelli, M. Weger, A. Ludwig, J. Maurer, L. Gallmann, and U. Keller, "Studying Momentum Distributions in all Aspects Reveals Important Insight" — Poster, *International Workshop on Atomic Physics*, Dresden, Germany, November 24–28, 2014

19. A. Ludwig, M. Lucchini, L. Kasmi, J. Herrmann, T. Zimmermann, L. Gallmann, and U. Keller, "Attosecond Quantum Beat Spectroscopy on Helium" — Poster, *National Centres of Competence in Research: Molecular Ultrafast Science and Technology (NCCR MUST) Annual Meeting*, Engelberg, Switzerland, January 12–14, 2015

20. M. Lucchini, J. Herrmann, A. Ludwig, L. Kasmi, M. Volkov, S. Sato, K. Yabana, Y. Shinohara, L. Gallmann, and U. Keller, "Attosecond transient absorption of polycrystalline diamond" — Talk, *National Centres of Competence in Research: Molecular Ultrafast Science and Technology (NCCR MUST) Annual Meeting*, Engelberg, Switzerland, January 12–14, 2015

21. J. Maurer, A. Ludwig, B. W. Mayer, C. R. Phillips, L. Gallmann, and U. Keller, "Breakdown of the dipole approximation in strong field ionization" — Talk,

National Centres of Competence in Research: Molecular Ultrafast Science and Technology (NCCR MUST) Annual Meeting, Engelberg, Switzerland, January 12–14, 2015

22. L. Kasmi, M. Lucchini, P. Kliuiev, L. Castiglioni, A. Ludwig, M. Hengsberger, J. Osterwalder, L. Gallmann, and U. Keller, "Probe-induced time delays in single photon emission from a Copper (111) surface" — Talk, *Conference on Lasers and Electro-Optics/Europe - European Quantum Electronics Conference (CLEO/Europe - EQEC)*, Munich, Germany, June 21–25, 2015

23. M. Lucchini, T. Zimmermann, A. Ludwig, L. Kasmi, J. Herrmann, A. Landsman, L. Gallmann, and U. Keller, "Time-resolved study of helium excited states performed with attosecond quantum-beat spectroscopy" — Talk, *Conference on Lasers and Electro-Optics/Europe - European Quantum Electronics Conference (CLEO/Europe - EQEC)*, Munich, Germany, June 21–25, 2015

24. A. Ludwig, J. Maurer, B. W. Mayer, C. R. Phillips, L. Gallmann, and U. Keller, "Breakdown of dipole approximation in strong-field ionization" — Talk, *Conference on Lasers and Electro-Optics/Europe - European Quantum Electronics Conference (CLEO/Europe - EQEC)*, Munich, Germany, June 21–25, 2015

25. M. Lucchini, M. Brügmann, A. Ludwig, L. Gallmann, U. Keller, and T. Feurer, "Reconstruction of attosecond pulses by ptychography" — Poster, *5th International Conference on Attosecond Physics (ATTO)*, Saint-Sauveur, Québec, Canada, July 6–10, 2015

26. M. Lucchini, S. A. Sato, J. Herrmann, A. Ludwig, M. Volkov, L. Kasmi, K. Yabana, Y. Shinohara, L. Gallmann, and U. Keller, "Direct observation of sub-cycle electron dynamics in polycrystalline diamond" — Poster, *5th International Conference on Attosecond Physics (ATTO)*, Saint-Sauveur, Québec, Canada, July 6–10, 2015

27. L. Kasmi, M. Lucchini, L. Castiglioni, P. Kliuiev, A. Ludwig, M. Greif, M. Hengsberger, J. Osterwalder, L. Gallmann, and U. Keller, "Probe field in photoemission delay measurements on a Cu(111)-Surface: validity of macroscopic laws on atomic and attosecond scales" — Talk, *5th International Conference on Attosecond Physics (ATTO)*, Saint-Sauveur, Québec, Canada, July 6–10, 2015

28. L. Kasmi, M. Lucchini, L. Castiglioni, P. Kliuiev, A. Ludwig, M. Greif, M. Hengsberger, J. Osterwalder, L. Gallmann, and U. Keller, "IR-transient-grating induced phase on photoemission delays from Copper(111) surface" — Poster, *Ultrafast Dynamic Imaging of Matter (UDIM)*, Grindelwald, Switzerland, March 8–12, 2015

29. M. Lucchini, T. Zimmermann, A. Ludwig, L. Kasmi, J. Herrmann, A. Landsman, L. Gallmann, and U. Keller, "Attosecond quantum-beat spectroscopy of helium excited states" — Poster, *Ultrafast Dynamic Imaging of Matter (UDIM)*, Grindelwald, Switzerland, March 8–12, 2015

30. J. Maurer, A. Ludwig, B. W. Mayer, C. R. Phillips, L. Gallmann, and U. Keller, "Breakdown of the dipole approximation in strong field ionization" — Talk, *Ultrafast Dynamic Imaging of Matter (UDIM)*, Grindelwald, Switzerland, March 8–12, 2015

31. J. Maurer, B. W. Mayer, C. R. Phillips, A. Ludwig, L. Gallmann, and U. Keller, "Rescattering dynamics in strong-field ionization of atomic and molecular targets beyond the dipole approximation" — Talk, *Conference on Extremely High Intensity Laser Physics*, Heidelberg, Germany, July 21–24, 2015
32. J. Maurer, B. W. Mayer, C. R. Phillips, A. Ludwig, L. Gallmann, and U. Keller, "Rescattering dynamics in strong-field ionization of atomic and molecular targets beyond the dipole approximation" — Talk, *11th Conference on Super Intense Laser-Atom Physics (SILAP)*, Bordeaux, France, September 7–10, 2015
33. L. Gallmann, C. R. Phillips, B. Mayer, A. Ludwig, J. Maurer, and U. Keller, "Exploring the long-wavelength limit of the electric dipole approximation" — Invited Talk, *International Conference on Extreme Light (ICEL)*, Bucharest, Romania, November 23–27, 2015

Abstract

Recent developments in laser technology have paved the way for a new field of research called attosecond science. Laser sources delivering ultrashort pulses with durations on the order of femtoseconds have shed new light on the dynamics on atomic and molecular timescales. Furthermore, the application of intense femtosecond pulses in strong-field ionization of atoms has led to the discovery of high-order harmonic generation, in essence a frequency up-conversion process and the basis of attosecond experiments.

The field of attosecond science focuses on control and analysis of electron dynamics in atoms, molecules, and solids by using coherent subfemtosecond pulses in the extreme-ultraviolet spectral range. This thesis presents studies on strong-field and attosecond ionization dynamics in representative atomic and molecular systems ranging from noble gases to basic hydrocarbons.

First, we report on an experiment on the strong-field ionization of noble gases by mid-infrared laser pulses. Non-dipole effects were predicted to emerge for peak intensities on the order of $10^{13}\,\mathrm{W/cm^2}$ in this long-wavelength regime of strong-field ionization. We analyze photoelectron momentum distributions acquired with a velocity map imaging spectrometer. We find evidence for an influence of the magnetic field component of the laser pulse during ionization, visible as asymmetries along the propagation direction. This asymmetry is essentially a shift of the peak of the electron momentum distribution caused by the combined laser field and Coulomb potential. It is a sign of the breakdown of the dipole approximation in strong-field ionization and challenges the theoretical treatment of ionization dynamics at long wavelengths.

The second part of this work is centered around the characterization and application of attosecond pulses in pump-probe experiments. We present and benchmark a new iterative FROG-CRAB algorithm called ptychographic reconstruction of attosecond pulses. This method is capable of retrieving the complete temporal properties of attosecond pulses but performs far better and imposes much lower demands on the delay sampling and the signal-to-noise ratio of the experimental photoelectron spectrogram in comparison to commonly used reconstruction schemes.

Third, we present results from the application of attosecond pulses to an attosecond quantum beat spectroscopy experiment on excited states in helium. Our spectrally tailored excitation pulse minimizes direct ionization and thus allows unperturbed access to the quantum beat signal even in the region of temporal overlap of the two applied pulses. A comparison with calculations of the time-dependent Schrödinger equation complies with the observed oscillations and reveals a previously neglected anisotropy in some of the quantum beats. We show that this anisotropy can be used to control the photoemission direction by varying the carrier envelope phase of the probe pulse.

The fourth study, a pump-probe experiment based on fragment ion detection, allows us to examine ultrafast isomerization and dissociation dynamics of the ethylene cation ${C_2H_4}^+$. This sheds new understanding on the dynamics of the excited nuclear wave packets on their natural timescale of few femtoseconds. We attribute the dynamics in the ion yields to transitions between different potential surfaces in the vicinity of conical intersections. Ultimately, we show the control of the dissociation to ${C_2H_3}^+$ and ${C_2H_2}^+$ on an ultrafast timescale.

Kurzfassung

Jüngste Entwicklungen in der Lasertechnologie haben einem neuen Forschungsgebiet, der Attosekunden-Wissenschaft, den Weg bereitet. Laser, die ultrakurze Pulse mit Pulsdauern in der Grössenordnung von Femtosekunden liefern, haben Einblicke in Dynamiken auf atomaren und molekularen Zeitskalen ermöglicht. Darüber hinaus hat die Anwendung von intensiven Femtosekundenpulsen in der Starkfeldionisation von Atomen zur Entdeckung der Erzeugung hoher Harmonischer geführt, die im Wesentlichen einen Frequenz-Umwandlungsprozess und die Basis von Attosekunden-Experimenten darstellt.

In der Attosekunden-Wissenschaft werden kohärente Pulse mit subfemtosekunden Pulsdauern im extrem-ultravioletten Bereich genutzt, um Elektronendynamiken in Atomen, Molekülen und Festkörpern zu kontrollieren und zu untersuchen. In der vorliegenden Arbeit präsentieren wir Ergebnisse in den Bereichen der Starkfeld- und Attosekunden-Ionisationsdynamiken am Beispiel von repräsentativen atomaren und molekularen Systemen, von Edelgasen bis hin zu einfachen Kohlenwasserstoffen.

Zuerst berichten wir von einem Experiment im Bereich der Starkfeldionisation von Edelgasen durch Laserpulse im mittleren Infrarotbereich. Für diesen langwelligen Bereich der Starkfeldionisation wurde das Aufkommen von Nicht-Dipol-Effekten bei Spitzenintensitäten in der Grössenordnung von 10^{13} W/cm^2 vorhergesagt. Wir untersuchen Photoelektronen-

Impulsverteilungen, die mit Hilfe eines *Velocity-Map-Imaging*-Spektrometers aufgenommen wurden. In diesen Impulsverteilungen sehen wir den Einfluss der Magnetfeldkomponente des Laserpulses während der Ionisation, erkennbar an Asymmetrien entlang der Ausbreitungsrichtung des Laserstrahls. Diese Asymmetrien kommen durch die Verlagerung der Spitzen der Impulsverteilungen zu Stande, verursacht durch das kombinierte Laserfeld- und Coulomb-Potential. Sie sind ein Zeichen des Zusammenbruchs der Dipolnäherung in der Starkfeldionisation und fordern die theoretische Beschreibung von Ionisationsprozessen bei langen Wellenlängen heraus.

Im zweiten Teil dieser Arbeit geht es um die Charakterisierung und Anwendungen von Attosekundenpulsen in Anrege-Abfrage-Experimenten. Wir präsentieren und vergleichen eine neue iterative FROG-CRAB-Methode, genannt ptychographische Rekonstruktion von Attosekundenpulsen. Diese Methode ermöglicht es, Attosekundenpulse zeitlich vollständig zu charakterisieren. Dabei zeichnet sich unser Algorithmus durch eine weit bessere Leistung aus und setzt weit geringere Ansprüche in Bezug auf die Schrittweite und das Signal-Rausch-Verhältnis des gemessenen Photoelektronen-Spektrogramms im Vergleich zu anderen weit verbreiteten Rekonstruktionsmethoden voraus.

Im dritten Teil dieser Arbeit stellen wir die Ergebnisse eines Experimentes vor, in dem wir Attosekundenpulse für die Quantenschwebungsspektroskopie von angeregten Zuständen in Helium verwenden. Unsere spektral angepassten Anregepulse minimieren den Beitrag durch direkte Ionisation und ermöglichen uns so ungehinderten Zugriff auf das Quantenschwebungssignal sogar im Bereich der zeitlichen Überlappung beider involvierter Pulse. Ein Vergleich mit Berechnungen auf Basis der zeitabhängigen Schrödingergleichung ergibt eine sehr gute Übereinstimmung der beobachteten Oszillationen und deckt eine Anisotropie in einigen der Quantenschwebungen auf, die in früheren Studien vernachlässigt wurde. Wir zeigen, dass sich auf Basis dieser Anisotropie die Emissionsrichtung mit Hilfe der Träger-Einhüllenden-Phase des Abfragepulses kontrollieren lässt.

Im vierten Teil dieser Arbeit, einem Anrege-Abfrage-Experiment basierend auf der Detektion von Fragment-Ionen, geht es um Messungen der ultraschnellen Isomerisations- und Dissoziations-Dynamiken des Ethylen-Kations ${C_2H_4}^+$. Mit diesem Experiment erreichen wir Einblicke in die Dynamiken von angeregten nuklearen Wellenpaketen auf ihrer natürlichen Zeitskala von wenigen Femtosekunden. Wir ordnen die Dynamiken in den Ionen-Signalen der verschiedenen Fragmente Übergängen zwischen Potentialflächen in der Nähe von konischen Schnittpunkten zu. Zum Schluss zeigen wir, dass wir die Dissoziation zu ${C_2H_3}^+$ und ${C_2H_2}^+$ auf ultrakurzen Zeitskalen kontrollieren können.

Chapter 1

Introduction

Exploring processes at the limits of measureable time and length scales has always been at the center of natural science. Beyond mans' natural reference frame of meter (m) and second (s), a fascinating world opens up reaching from cosmological scales down to molecular, atomic and electronic scales. This ranges on one side of the scale from at least 10^{26} m and 10^{17} s [1] right down to the Ångström ($1\,\text{Å} = 10^{-10}\,\text{m}$) and the femtosecond ($1\,\text{fs} = 10^{-15}\,\text{s}$) to tens of attoseconds ($1\,\text{as} = 10^{-18}\,\text{s}$). Ultrafast dynamics on the shortest timescales are of fundamental interest, they constitute the initial step of all physical and chemical reactions that enable life.

Historically, mechanical clocks served as first tool for the observation of processes faster than a second. Later, electronic devices based on semiconductor technology opened the way for measuring even below one nanosecond. In parallel to the development of chronometric devices, photography froze the motion of fast objects for short time frames on the order of milli- to microseconds. This was done by combining short exposure times with bright flashes of light. It allowed the first direct imaging of fast movements as demonstrated by Eadweard Muybridge's 1878 photography of a galloping horse [2] and Harold Edgerton's 1960s image of a bullet piercing through an apple [3]. Still, this approach was limited to timescales far away from those relevant for atoms and molecules.

It was the invention of the laser in 1960 by Theodore Maiman [4], quickly followed by the development of pulsed laser sources, that started a story of success. The short pulses emitted by mode-locked lasers enabled the measurement of processes on the order of pico- and femtoseconds. This was based on the same principle as flash photography. In so-called pump-probe experiments, a first laser pulse triggers a process, e.g., a physical or chemical reaction, and a second laser pulse arriving with a controlled delay probes the dynamics at different instances in time. Pump-probe experiments allow us to observe signatures of absorption or emission in the probe pulse spectrum as well as photoelectron or photoion detection.

In 1999, Ahmed Zewail was awarded the Nobel Prize in Chemistry "for his studies of the transition states of chemical reactions using femtosecond spectroscopy" [5]. He pioneered the application of short laser pulses for the investigation of chemical processes on a sub-picosecond timescale and opened the field of research called femtochemistry. It was at the end of the 1980s that along with coworkers he performed the first pump-probe measurements on the photoinduced dissociation of cyanogen iodide (ICN). This allowed them to measure a reaction time of 200 fs [6]. Since the advent of femtochemistry, advances in laser technology improved the temporal resolution of pump-probe experiments to far below 100 fs. Today, optical laser pulses can reach pulse durations as short as 2 fs [7].

The pulse duration of laser pulses cannot be shorter than the period of the constituting field. Thus, pulses with durations below 1 fs require a carrier frequency of several electronvolts and are no longer achievable with central wavelengths in the optical regime. Frequency up-conversion processes like high-order harmonic generation became necessary in order to pass this limit and achieve pulses with sub-femtosecond durations.

At the end of the 1980s the discovery of the intriguing properties of high-order harmonic generation [8, 9] was made. This paved the way for the conversion of conventional laser pulses into synchronized coherent light bursts with photon energies in the range of a few to several hundred electronvolts and intrinsic sub-femtosecond pulse durations. These properties make harmonic radiation the ideal tool for studies of atomic, molecular, and electron dynamics.

The combination of attosecond/extreme ultraviolet (XUV) and infrared (IR) pulses in pump-probe experiments has led to stunning results on previously inaccessible timescales and set the foundation for the field of research called attosecond science. Among those results are the direct observation of valence electron dynamics [10], ionization time delays in atoms [11], charge migration in molecules [12, 13], reconstruction of electron wave packets [14] and of electron dynamics in solids [15, 16, 17].

Focusing of an intense ultrashort laser pulse leads to peak intensities on the order of $10^{14}\,\mathrm{W/cm^2}$. At these intensities, the associated electric field potential of the pulse causes an effective distortion of the binding Coulomb potential of the atom or molecule and thus gives rise to ionization. Apart from attosecond science, studies in this so-called strong-field ionization regime have led to numerous remarkable results as the outgoing photoelectron wave packet carries signatures of the Å-scale structure and sub-cycle dynamics in atoms and molecules [18, 19, 20].

In this thesis, we combine a study of strong-field ionization driven by long-wavelength pulses with the application of harmonic radiation in a pump-probe experiment to atomic and molecular systems. The strong-field ionization experiments were motivated by the tendency to use the generation of high-order harmonics in the soft X-ray regime around the water-window, which can be achieved in a table-top experiment based on long-wavelength driving sources [21, 22, 23]. For these generation wavelengths, the commonly applied dipole approximation in the theoretical description of the ionization process was predicted to break down at moderate intensities [24, 25, 26]. Existing studies in this field where based on circular polarization, assumed a negligible influence of the Coulomb potential [27] and were thus not applicable to the case of high-order harmonic generation. We therefore used a state-of-the-art mid-infrared source in order to investigate non-dipole effects in strong-field ionization for the important case of linear polarization.

We then turn to applications of high-order harmonic generation in our existing attosecond beamline (the attoline) driven by near-infrared pulses. In this case we concentrate on pump-probe experiments involving charged particle detection, i.e., photoelectron and photoion spectroscopy.

Here, our initial experiment in attosecond science starts with the temporal characterization of attosecond pulses. This is based on an XUV-IR cross-correlation photoelectron measurements. It also builds on reconstruction algorithms that usually impose certain requirements on the measured photoelectron spectrogram. This especially affects the pump-probe delay sampling and the signal-to-noise ratio. We present a new method for the complete temporal reconstruction of attosecond pulses that largely overcomes these limitations. We call this ptychographic reconstruction of attosecond pulses. We characterize the performance of this new algorithm and compare it to two widely applied methods, namely to the principal components generalized projection algorithm and to the least-squares generalized projection algorithm.

In a second experiment, we apply attosecond pulses in the attoline to perform quantum beat spectroscopy of helium excited states. We demonstrate that attosecond quantum beat spectroscopy, based on charged particle detection, constitutes a powerful tool that allows access to the angular content of the excited electron wave packets. In contrast to earlier studies based on broadband single attosecond pulses [28] we profit from tailored XUV pulses below the ionization threshold in order to reduce direct ionization and achieve unperturbed access to the interesting region of temporal pump-probe overlap.

Finally, we focus on ultrafast dynamics in molecules, especially on isomerization and dissociation processes in the prototype system ethylene C_2H_4. Ultrafast isomerization is known to play a key role in the human eye. The first step of vision occurs when the retinal molecule ($C_{20}H_{28}O$) embedded in the protein rhodopsin undergoes a cis-trans isomerization within 200 fs after absorption of one photon in the visible [29, 30]. We therefore investigate the role of conical intersections in the isomerization and dissociation after photoexcitation of the ethylene cation ${C_2H_4}^+$ in a pump-probe experiment. We extract the timescales of different relaxation channels and demonstrate the control of the dissociation leading to ${C_2H_3}^+$ and ${C_2H_2}^+$.

This thesis is structured as follows: In Chapter 2, we introduce the basic physical concepts. We give an overview over different ionization regimes, introduce properties of ultrashort laser pulses and their application in high-order harmonic generation and attosecond measurement techniques.

In Chapter 3 we present the two experimental setups that were used for the studies presented in this work. This includes the mid-infrared source together with the velocity map imaging spectrometer used for the strong-field experiments and the chirped pulse amplification system delivering pulses in the near-infrared used for the high-order harmonic generation. It also covers the attosecond beamline.

In Chapter 4 we discuss and explore the long-wavelength limit of the electric dipole approximation in the theoretical description of ionization processes. We show, that the magnetic field component of the mid-IR pulses has a non-negligible effect on the ionization process. This causes a shift of the peak of the momentum distribution opposite to the beam propagation direction.

In Chapter 5 we introduce and characterize the new algorithm for the complete temporal reconstruction of attosecond pulses based on ptychography. The reconstruction scheme is able to retrieve the complete amplitude and phase of the attosecond pulses. It requires considerably lower demands on the delay sampling and the signal to noise ratio in attosecond streaking measurements.

In Chapter 6 we apply a spectrally tailored attosecond pulse train in an attosecond quantum beat spectroscopy study of helium excited states. We compare our experimental results with calculations of the time-dependent Schrödinger equation and discover an anisotropy of the quantum beat signal that was previously neglected in a similar study.

In Chapter 7 we present investigations of the ultrafast fragmentation dynamics of the ethylene cation $C_2H_4{}^+$ in an XUV-pump-IR-probe scheme. We show that we can use the IR pulse to control the fragmentation channels on an ultrafast timescale.

Finally, we summarize all results in Chapter 8 and give an outlook on possible future studies and applications based on the advancements developed and presented in the frame of this thesis.

Chapter 2

Tools in Strong-Field & Attosecond Science

The fundamental requirement for the studies presented in this work reside in the availability of ultrashort laser pulses on the femtosecond timescale. These femtosecond pulses can either directly be applied in the experiment in case of strong-field ionization studies or they provide the basis of high-order harmonic generation delivering attosecond pulses with frequencies in the extreme ultraviolet (XUV) regime in the frame of attosecond experiments.

In this chapter we will review the foundations of experimental studies on the femto- and attosecond timescale in terms of basic light-matter interactions, the properties of femtosecond laser pulses and their application to high-order harmonic generation (HHG) as well as concomitant tools in attosecond science. Atomic units ($\hbar = e = m_e = 1$) are used throughout this thesis unless stated otherwise.

2.1 Atoms in Laser Fields

The exposure of an atom to a laser field can lead to the removal of a bound electron and thus to ionization. Phenomenologically, this ionization process can be described by different mechanisms depending on the photon energy ω and the intensity I of the laser field. Figure 2.1 illustrates these mechanisms ranging from single-photon to tunnel ionization.

The simplest case is single-photon ionization which can take place if the

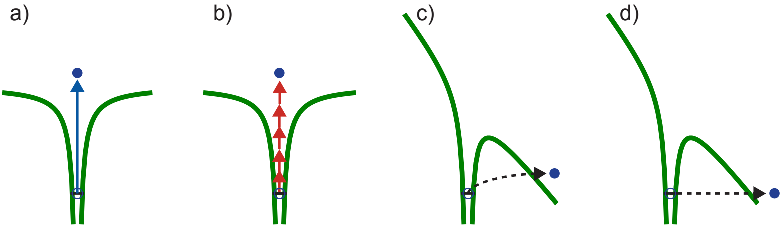

Figure 2.1: Illustration of the different ionization regimes that lead to the transition of a bound electron in a Coulomb potential to a continuum state: a) Single-photon ionization, b) Multi-photon ionization, c) non-adiabatic tunnel ionization, and d) tunnel ionization.

photon energy is larger than the ionization potential of the atom $\omega \geq I_\mathrm{p}$. This process was first described by Albert Einstein in his description of the photoelectric effect [31]. Here, the absorption of one single photon leads to ionization of the atom and emission of an electron with the kinetic excess energy $E_\mathrm{el} = \omega - I_\mathrm{p}$ (Fig. 2.1a)).

At higher intensities I of the laser field, ionization may still occur even if the photon energy is insufficient to overcome the ionization potential. Ionization in this regime of small photon energies and high intensities is called strong-field ionization regime which includes the mechanisms Fig. 2.1b) to d). In contrast to the case of single-photon ionization, the ionization rate in this regime increases non-linearly with the intensity of the field.

One fundamental mechanism in strong-field ionization is multi-photon absorption (Fig. 2.1b)) [32]. Here, the simultaneous absorption of more than one photon provides the energy necessary to overcome the ionization potential and leads to ionization and the release of an electron with energy $E_\mathrm{el} = N\omega - I_\mathrm{p} - U_\mathrm{p}$, with integer N, $N\omega \geq I_\mathrm{p}$, and the ponderomotive energy U_p as a measure for the average kinetic energy of an electron quivering in an oscillating electric field:

$$U_\mathrm{p} = \frac{I}{4\omega^2}. \tag{2.1}$$

The second fundamental mechanism in strong-field ionization can be best understood in a quasi-static field picture (Fig. 2.1 d)). Here, the strong electric field leads to a bending of the Coulomb potential of the atom and the formation of a potential barrier through which the electron might tunnel into the continuum. In this so-called tunnel ionization, the ionization probability depends highly on the barrier and thus on the peak electric field forming it (see Chapter 4 for details on the ionization rate).

A common criterion to distinguish the regimes of multi-photon and tunnel ionization is the Keldysh parameter [33]

$$\gamma = \sqrt{\frac{I_\mathrm{p}}{2U_\mathrm{p}}} = \omega\sqrt{\frac{2I_\mathrm{p}}{I}}, \tag{2.2}$$

The Keldysh parameter separates the two strong-field ionization regimes as asymptotic limits. For $\gamma \gg 1$, ionization is dominated by multiphoton ionization whereas for $\gamma \ll 1$ mostly tunnel ionization takes place. The intermediate regime for $\gamma \approx 1$ is called non-adiabatic tunneling regime (Fig.2.1c)) where the electron acquires energy under the barrier.

The emergence of ultrashort light pulses in a variety of wavelengths and intensities has enabled targeted studies on individual aspects of the different ionization regimes. Today, dynamics in single-photon ionization of atoms and molecules can be investigated with the help of harmonic radiation and attosecond pulses (Sec. 2.3) whereas strong-field ionization phenomena can directly be explored by laser pulses at wavelengths from the visible to the mid-infrared (MIR) [34, 18, 19, 35, 36, 37, 38].

2.2 Femtosecond Laser Pulses

Few years after the invention of the laser [4], the method of mode-locking was proposed [39] and realized [40] which set the basis for the development of femtosecond laser sources. Mode-locking is the technique that locks all cavity modes in a laser to oscillate with a defined phase relation. This phase-locking leads to constructive interference and the emission of a train of laser pulses with a pulse spacing T_rep equal to the optical cavity length divided by the speed of light (Fig. 2.2). Different active and passive mode-locking techniques based on acousto-optic modulators (AOMs), Kerr lens mode-locking (KLM) [41, 42] or semiconductor saturable absorber mirrors (SESAMs) [43, 44] have been established and contributed

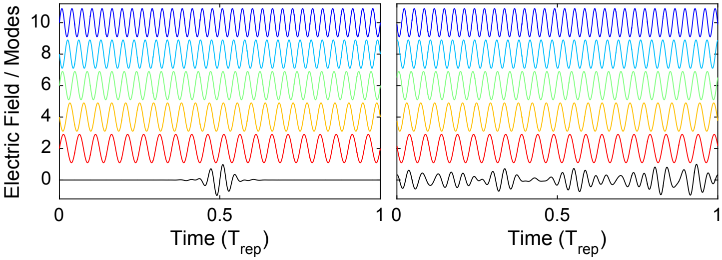

Figure 2.2: Principle of mode-locking. Left: Locking the phases of the cavity modes (colored lines) leads to constructive interference and the formation of a pulse that oscillates in the cavity. Right: For random phases, no pulse formation is observed.

to the rapid development of lasers capable of delivering pulses with durations in the pico- to femtosecond range.

Up to now, KLM applied in Ti:sapphire lasers leads to the shortest pulses directly from an oscillator, with pulse durations down to 5.5 fs [45]. The development of these femtosecond laser sources led to the foundation of today's ultrafast science with studies of dynamics in atoms and molecules on previously inaccessible timescales.

When approaching the few-cycle limit of laser pulses, i.e., the limit where the number of cycles of the electric field under the envelope approaches one, the influence of the carrier-envelope phase (CEP) becomes significant. The CEP is a measure for the offset of the peak of the electric field with respect to the pulse envelope. In Figure 2.3, we show two laser pulses with identical pulse envelopes but for two different values of the CEP, $\varphi_{\mathrm{CEP}} = 0$ and $\varphi_{\mathrm{CEP}} = \pi/2$.

The CEP value of individual emitted pulses reflects the phase slip per roundtrip of the pulses in the cavity, caused by dispersion in air and the optical elements of the laser. In general, this phase slip per roundtrip is not constant and the outgoing pulses thus exhibit varying CEPs. Some experiments like those involving single attosecond pulses require identical waveforms of the laser pulses and thus stabilization of the CEP. Therefore, a variety of schemes allow the detection of this parameter. Among those schemes the most common is the f-to-$2f$ interferometer that uses the beating of a fundamental frequency f with a frequency-doubled component

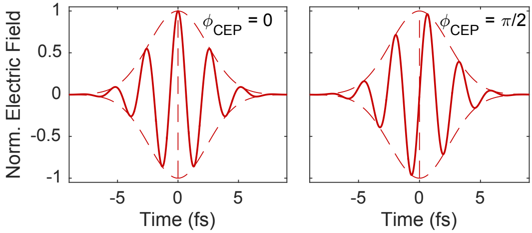

Figure 2.3: Electric field of a laser pulse for a CEP value of 0 and $\pi/2$, visible as an offset of the electric field peak from the peak of the envelope, depicted as dashed line.

$2f' = f$ in an octave spanning spectrum. CEP-stabilized laser systems as those used in this thesis for attosecond experiments, contain a closed-loop stabilization system that adjusts the dispersion in the cavity and the amplification stages in order to achieve the output of a train of waveform-identical femtosecond pulses.

The electric field of a laser pulse with a Gaussian envelope function $f(t)$ can usually be approximated in time domain by

$$\begin{aligned} \boldsymbol{E}(t) &= \boldsymbol{E}_0 f(t) e^{\mathrm{i}\omega t + \varphi_{\mathrm{CEP}}} + c.c. \\ f(t) &= e^{-\ln(4)t^2/\tau_{\mathrm{FWHM}}{}^2} \end{aligned} \tag{2.3}$$

Here, $\boldsymbol{E}_0$ with $|\boldsymbol{E}_0| = \sqrt{I_0}$ is the peak electric field, τ_{FWHM} is the full width at half maximum (FWHM) pulse duration in intensity and φ_{CEP} the carrier-envelope phase.

When propagating through dispersive media, this description of an ideal pulse based on a constant frequency does not hold any longer. Dispersion in air or other media causes different phase velocities of different frequency components constituting the pulse and thus to a so-called chirp, accompanied by a temporal stretching to pulse durations longer than the Fourier limit. Propagation through a medium with "normal" dispersion leads to a pulse where the low-frequency components arrive at the leading edge and the high-frequency components at the trailing edge of the pulse, a so-called up-chirp.

This effect can best be described in the frequency domain representation of the pulse

$$\tilde{E}(\omega) = \tilde{E}_0 \tilde{f}(\omega) e^{\mathrm{i}\varphi(\omega)} + c.c. \tag{2.4}$$

A pulse traveling through a dispersive medium of length L with refractive index $n(\omega)$ experiences the dispersion as change in its phase

$$\varphi'(\omega) = \varphi(\omega) + \frac{\omega}{c} n(\omega) L. \tag{2.5}$$

The phase of the pulse $\varphi(\omega)$ can be developed in a Taylor series around the central frequency ω_0 in order to identify the different contributions:

$$\begin{aligned} \varphi(\omega) = \varphi_0 &+ \frac{\mathrm{d}\varphi}{\mathrm{d}\omega}(\omega - \omega_0) \\ &+ \frac{1}{2}\frac{\mathrm{d}^2\varphi}{\mathrm{d}\omega^2}(\omega - \omega_0)^2 \\ &+ \frac{1}{6}\frac{\mathrm{d}^3\varphi}{\mathrm{d}\omega^3}(\omega - \omega_0)^3 \\ &+ \dots \end{aligned} \tag{2.6}$$

Here, the zeroth order φ_0 affects the CEP, the first order $\mathrm{d}\varphi/\mathrm{d}\omega$ is the group delay (GD), the second order $\mathrm{d}^2\varphi/\mathrm{d}\omega^2$ is the group delay dispersion (GDD), and the third order $\mathrm{d}^3\varphi/\mathrm{d}\omega^3$ is called third-order dispersion (TOD). Changes of the second or higher order affect the temporal properties of the laser pulse. For example, a positive value of the GDD corresponds to an up-chirp as discussed above and leads to a symmetric temporal broadening of the pulse whereas an increase in the TOD leads to an asymmetric broadening.

For some applications, like the theoretical description of a charge in the oscillating electric field, it is more convenient to describe the laser field by its vector potential

$$\boldsymbol{A}(t) = \int_t^\infty \boldsymbol{E}(t')\mathrm{d}t'. \tag{2.7}$$

We introduce this representation as it will be used in the next sections for the description of attosecond streaking.

2.3 High-Order Harmonic Generation

High-order harmonic generation (HHG) is a frequency up-conversion process driven by ultrashort intense laser pulses during the interaction with

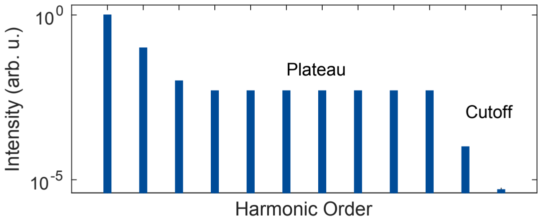

Figure 2.4: Illustration of the typical intensity distribution of a high-order harmonic spectrum. After an initial strong decrease in intensity for low harmonic orders, the intensity stabilizes on a plateau which extends up to the cutoff energy.

atoms, pioneered at the end of the 1980s by McPherson and L'Huillier [8, 9, 46]. They focused intense laser pulses into a gas target and observed the emergence of an intensity plateau in the sharp harmonic peaks reaching into the XUV spectral range (Fig. 2.4). The appearance of peaks limited to odd harmonics of the fundamental laser frequency was well understood within the dipole approximation whereas the intensity behavior first seemed surprising but led to the idea to apply this effect in a table-top source for light pulses in the XUV regime.

2.3.1 Single-Atom Response

A simple picture to understand HHG in gas phase is the so-called three-step or simple man's model [47], a semi-classical model that describes

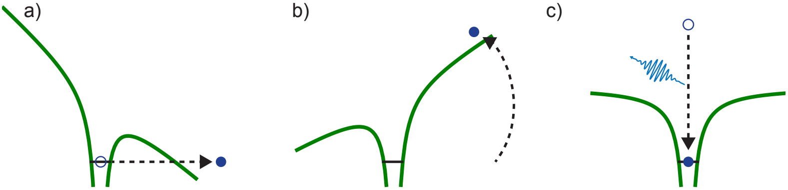

Figure 2.5: The three-step model in high-order harmonic generation: a) The combined Coulomb and laser potential forms a barrier through which the electron may tunnel into the continuum. b) The oscillating electric field accelerates the electron wave packet away and then back to the ion. c) Recollision with the ion leads to recombination to the bound state and emission of a photon carrying the excess energy.

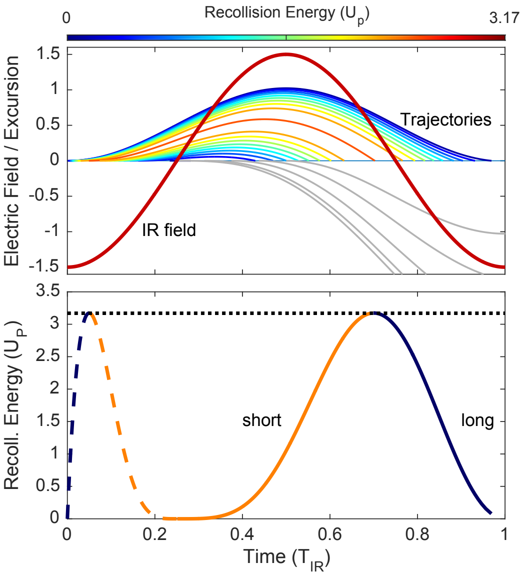

Figure 2.6: Upper panel: Schematics of the electron trajectories (colored lines) in a linearly polarized laser field (red line) for different times of ionization. The color of each trajectory depicts its recollision energy. Electrons, that undergo ionization before the peak of the field are driven away from the ion and thus do not recollide (gray trajectories). Lower panel: Recollision energies of the electrons as function of their ionization (dashed) and recombination (solid) time. Two types of trajectories can contribute to the harmonic emission, the so-called short and long trajectories.

the single-atom response to a strong laser field leading to the emission of high-energy photons. In the first step, the Coulomb potential of the atom is bend by the electric field of the laser pulse such that it forms a barrier through which the electron may tunnel into the continuum (Fig. 2.5a)). Next, the oscillating electric field accelerates the ionized electron wave packet first away and then back to the ion (Fig. 2.5b)) where it can undergo recombination to the bound state while emitting the excess energy as photon with $\omega = I_\mathrm{p} + E_\mathrm{kin}$ (Fig. 2.5c)).

In this process, the phase of ionization determines the recollision energy as depicted in Fig. 2.6. It can immediately be seen that two types of trajectories contribute to each energy, the so-called short and long trajectories denoted by the time spent in the continuum. Since the process

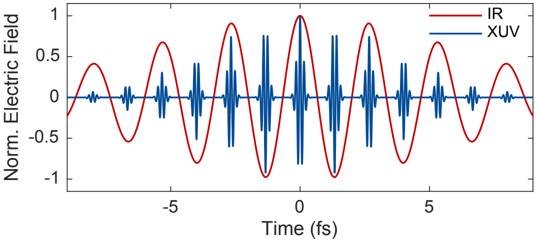

Figure 2.7: In high-order harmonic generation, attosecond pulses are emitted every half-cycle of the generating laser field and form an intrinsically phase-locked pulse train. This corresponds to a periodic structure in frequency domain consisting of peaks at odd multiples of the driving field's photon energy.

described by the three-step model is repeated every half-cycle of the driving infrared (IR) field, it leads to the emission of photon bursts intrinsically phase-locked to the generating field with half of its period (Fig. 2.7). This periodicity in the time domain constitutes the well-known comb-like harmonic structure in the frequency domain with a spacing of $2\omega_{\mathrm{IR}}$ between two adjacent harmonic peaks (see Fig. 2.8 upper panels).

As mentioned above, the experimental intensity behavior of a typical high-order harmonic spectrum exhibits a plateau of constant intensity (Fig. 2.4). This plateau follows a strong decrease in intensity for lower orders and can reach up to harmonics of several hundred eV photon energy until reaching a sharp edge, known as the cutoff energy. The exact shape of the harmonic spectrum can be reproduced by a model taking into account the ionization and recombination dipole moments. Still, the phenomenological expression for the cutoff energy following [48]

$$\omega_{\mathrm{cut}} = I_{\mathrm{p}} + 3.17U_{\mathrm{p}} \tag{2.8}$$

as function of the ionization potential I_{p} of the atom and the ponderomotive energy U_{p} (see Eq. 2.1) is reproduced surprisingly well in our simple semi-classical analysis of the contributing trajectories visible as maximal recollision energy (Fig. 2.6). In the experiment, the cutoff energy can be increased by generation with longer wavelengths or by using a two-color field, e.g., in a heterodyne mixing scheme [49].

A full quantum-mechanical description of the HHG process followed in 1994 introduced by Lewenstein et al. as solution of the time-dependent Schrödinger equation (TDSE) [50].

2.3.2 Phase-Matching

The application of high-order harmonic generation in the experiment requires the constructive interference of harmonic emission stemming from different atoms in the interaction region. This condition can be formulated based on the wave vectors of the generating an emitted fields. Thus, for the generation of the qth harmonic with photon energy $q\omega_{\mathrm{IR}}$ the phase-mismatch between the generating and emitted field has to vanish [51]:

$$\Delta \boldsymbol{k} = q\boldsymbol{k}_{\mathrm{IR}} - \boldsymbol{k}_q = \Delta \boldsymbol{k}_{\mathrm{g}} + \Delta \boldsymbol{k}_{\mathrm{d}} + \Delta \boldsymbol{k}_{\mathrm{i}} = 0 \tag{2.9}$$

The first term $\Delta \boldsymbol{k}_{\mathrm{g}}$ stems from the focusing geometry that introduces a shift in the wavefront along the focus, the Gouy phase shift. The contribution $\Delta \boldsymbol{k}_{\mathrm{d}}$ reflects the dispersion in the target gas and the free electron plasma in the interaction region and the term $\Delta \boldsymbol{k}_{\mathrm{i}}$ describes the intrinsic intensity-dependent dipole phase that can be seen as the phase of the wave packet acquired during its trajectory.

In the experiment, the phase-matching condition can usually be fulfilled for the short trajectories by placing the gas-target after the focus and adjusting the intensity of the generating pulses and the gas pressure in the target [52]. In this configuration, phase-matching is achieved in a significant volume and leads to the emission of high-order harmonics with small divergence and a positive chirp that can conveniently be compensated by transmission through an aluminum (Al) foil exhibiting negative GDD in the XUV spectral region.

2.4 Single Attosecond Pulse Generation

In 2001 Agostini and coworkers demonstrated experimentally, that the harmonic emission stemming from the HHG process corresponds to a train of pulses with durations around 250 as [53]. This observation paved the way for the application of APTs in studies on the attosecond timescale.

Despite the large amount of experimental studies that were enabled by the availability of APTs, some applications require the generation of

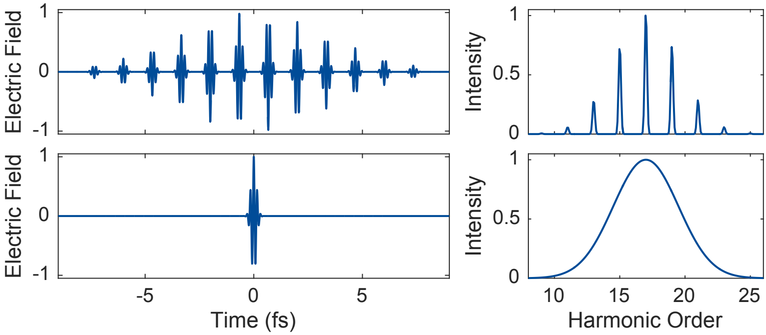

Figure 2.8: Sketch of an APT (upper panels) and a SAP (lower panels) in time (left) and frequency domain (right). The half-IR-cycle periodicity of the bursts in the case of the attosecond pulse train leads to the comb-like harmonic structure in frequency domain with a spacing of $2\omega_{\mathrm{IR}}$ between two consecutive harmonics whereas the single attosecond pulse exhibits a broad continuous spectrum.

SAPs in order to exploit their intrinsic time-duration [12], their associated broad continuous spectrum [28] or to overcome the inherent periodicity of attosecond pulse trains [54] (Fig. 2.8).

The isolation of SAPs has first been demonstrated by Hentschel et al. [55] by means of amplitude gating. This method is based on the spectral selection of photons in the cutoff region that stem from the emission during one central half-cycle around the peak electric field of the generating laser pulse. Since this breakthrough, different techniques have been established in order to limit or separate the generation of attosecond pulses from one single half-cycle of the IR field, namely polarization gating (PG) [56], double optical gating (DOG) [57], ionization gating [58, 59] or spatiotemporal gating like the attosecond lighthouse technique [60, 61, 62].

In contrast to amplitude and intensity gating where the usable spectral range is limited to the cutoff region of the HHG spectrum, the PG method, DOG and the attosecond lighthouse technique produce broad XUV spectra covering the plateau and the cutoff [63].

Parts of the work in this thesis are based on SAP generation by means of polarization gating that will here be introduced in detail. The method of polarization gating is based on the strong dependence of HHG on the

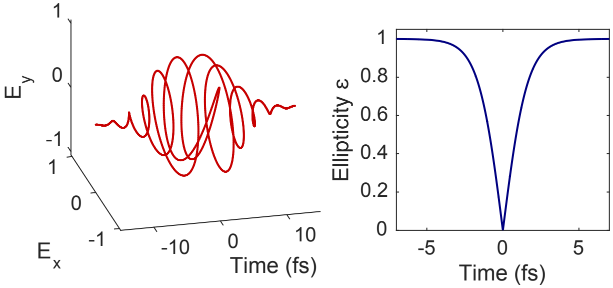

Figure 2.9: Representation of the driving field's polarization state used in the polarization gating technique. The leading and trailing edges of the pulse exhibit circular polarization ($\varepsilon \approx 1$) whereas the central part consists of a short window with linear polarization ($\varepsilon \approx 0$). The harmonic generation is effectively limited to the central half-cycle with ellipticities below 0.1.

ellipticity of the generating field which drops drastically for ellipticities above 0.1 [64, 65]. In order to exploit this dependency, the generating IR pulse is prepared in a polarization state with mostly circular polarization and a small time window exhibiting linear polarization.

In practice, the generating IR pulse is transmitted through a combination of a thick birefringent quartz and a consecutive quarter-wave plate. The orientation of the quartz plate is chosen such that its ordinary axis includes an angle of 45° with respect to the linear polarization direction of the IR field. After the quartz plate the laser pulse consists of three parts: two linearly polarized leading and trailing edges with perpendicular polarization directions to each other as well as an elliptically polarized central part.

Transmission through the successive quarter-wave plate acting on this polarization state results in a pulse with leading and trailing circularly polarized parts and a short linearly polarized region in the center (Fig. 2.9). Focused into a gas jet, this laser pulse leads to harmonic emission limited to the central linear part during one half-cycle of the driving field.

It can be shown that the PG scheme requires IR pulse durations as short as 5 fs in order to yield efficient generation of isolated attosecond pulses [66]. The use of pulses with a longer duration demands an increased thickness of the quartz plate and lead to a significantly reduced

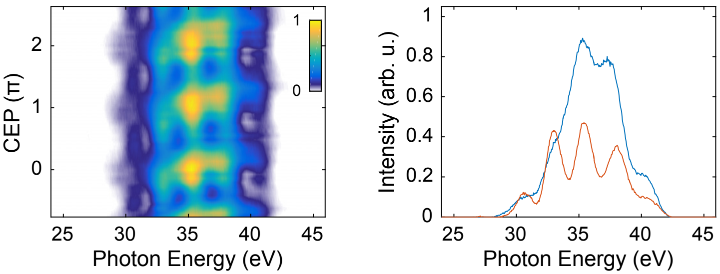

Figure 2.10: Experimental CEP scan: Measured photon spectra as a function of the generating pulse's CEP. The spectra change from a continuous to a discrete shape with a periodicity in the CEP of π. Right panel: Lineouts for CEP values of 0 and $\pi/2$. For the generation of single attosecond pulses, the CEP is adjusted such that the spectrum is maximal continuous.

intensity in the linearly polarized region and thus a reduced HHG efficiency.

The PG technique also requires the electric field of the driving field to peak during the central, linearly polarized part of the pulse and thus needs a stabilized and precisely controlled CEP. A deviation from this optimal CEP value leads to the generation of more than one photon burst and thus to a periodic structure in the XUV spectrum. This effect can be seen in a so-called CEP scan in which the XUV photon spectrum is recorded as function of the driving field's CEP revealing a transition from a continuous to a periodic spectrum and back. A typical measured CEP scan is shown in Fig. 2.10. The CEP optimization for the generation of single attosecond pulses can also be achieved based on CEP scan photoelectron measurements and a contrast analysis [67].

2.5 Characterization of Attosecond Pulses

Attosecond pulses and pulse trains can be described by a complex spectral field with a certain amplitude and phase, in the same way as optical laser pulses. The only observable directly accessible in the experiment is their intensity spectrum, the amplitude to the square, which lacks the phase information of the underlying pulses. A temporal reconstruction and characterization of attosecond pulses thus relies on measurement schemes that

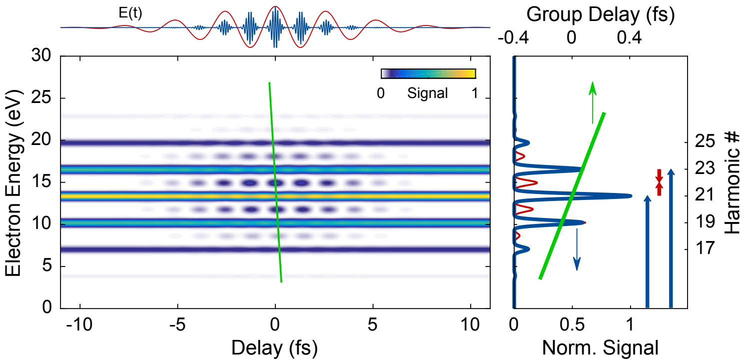

Figure 2.11: Calculated delay-dependent photoelectron spectrogram after ionization with an attosecond pulse train in presence of an IR field with an intensity of $10^{11}\,\mathrm{W/cm^2}$. For negative delays, the APT arrives first. The presence of the IR field leads to the formation of sidebands that show an oscillatory behavior. Top: The XUV (blue) and IR field (red) in time domain for the delay $\tau = 0\,\mathrm{fs}$. Right panel: The XUV spectral intensity consisting of odd harmonics is shown together with the positive attochirp as GD of the spectral components. The formation of sidebands is illustrated as pathways including the absorption of one XUV and one IR photon and the absorption of one XUV and the emission of one IR photon.

allow the extraction of this phase information prior to determination of the pulse durations. Here, we will present two schemes that are capable of revealing the spectral phase of attosecond pulse trains and single attosecond pulses, and highlight their application in the extraction of attosecond delays in ionization processes.

2.5.1 Attosecond RABBITT

The reconstruction of attosecond beating by interference of two-photon transitions (RABBITT) is based on a photoelectron measurement after the ionization of a target by an APT in the presence of a time-delayed IR field. A two-photon process involving one XUV and one IR photon is used to ionize ground state electrons to the same final energy through two pathways, the absorption of one XUV photon and one IR photon or the absorption of one XUV photon and the emission of one IR photon:

$$E_{2q} = \omega_{2q-1} + \omega_{\mathrm{IR}} = \omega_{2q+1} - \omega_{\mathrm{IR}} \tag{2.10}$$

Here, $2q+1$ and $2q-1$ with integer q are labels for the odd harmonic orders and $2q$ stands for the even sideband order.

In a quantum picture, this two-photon process leads to the interference of different quantum paths with the same final state of energy E_{2q} reflecting the phase difference. As a result, the photoelectron spectrum exhibits sidebands between the main harmonic lines that are oscillating as a function of the XUV-IR delay with a frequency of twice the fundamental IR frequency. The RABBITT scheme requires low IR intensities and can thus be described using second-order perturbation theory [53] which results in a calculated sideband amplitude of

$$S_{2q}(\tau) \propto \cos(2\omega_{\mathrm{IR}}\tau + \varphi_{2q-1} - \varphi_{2q+1} + \Delta\varphi_{\mathrm{atom}}) \tag{2.11}$$

with the IR frequency ω_{IR}, the XUV-IR delay τ, the phases of the neighboring harmonics φ_{2q-1} and φ_{2q+1} and the atomic phase contribution $\Delta\varphi_{\mathrm{atom}}$. The latter is comparably small and can usually be calculated for atoms with high precision. The IR phase $2\omega_{\mathrm{IR}}\tau$ drives the oscillation as function of the delay and allows the fitting of the integrated sideband signal with Eq. 2.11 to extract the delay-independent phases. It can be seen that the extraction of two neighboring sideband phases φ_{2q} and φ_{2q+2} is sufficient to directly reconstruct the phase of the harmonic $2q+1$.

Figure 2.11 shows a calculated RABBITT trace together with the underlying APT and IR field (convention: for negative delays, the APT arrives first). The positive attochirp (low frequencies at the leading edges of the attosecond pulses) results in a visible negative tilt in the appearance of the sideband peaks (green line) which is used to calculate the attochirp of the APT.

The tilt can easily be understood in the picture where the sideband peaks appear at delays where the respective frequency components of the attosecond pulses (APs) in the train overlap with peaks of the IR electric field. As these delay positions are given twice per IR period T_{IR}, the resulting period of the sideband oscillations is $T_{\mathrm{IR}}/2$. For a fixed delay, the higher frequency components of the up-chirped APs arrive later and thus overlap with a later part of the IR field. The lower frequency components will reach the same overlap for larger delays. This picture explains the shift of the high-energy sideband peaks to smaller and the low-energy sideband peaks to larger delays.

It should be noted, that the RABBITT technique does not allow the complete temporal reconstruction of the APT due to the fact that the resulting spectrogram only reflects the average of all attosecond pulses in the pulse train. Still, the RABBITT technique can be used to characterize the attochirp of the APT if the atomic properties of the target gas are well known.

It also allows for the extraction of attosecond timing information of a target under investigation by comparing its sideband phases with a reference system. For this, one can either measure two gaseous species at the same time in a coincidence spectrometer [68] or use a refocusing geometry and a spatially separated reference measurement which allows the extension to solid state systems [17]. Due to the fact that the exact time-zero in a pump-probe experiment is not accessible with attosecond precision, absolute phases and timing information remain hidden and only relative statements can be made.

2.5.2 Attosecond Streaking

Even though the experimental technique in attosecond streaking is quite similar to RABBITT, the underlying method for extracting information on the attosecond pulse in this scheme is different. In contrast to RABBITT, attosecond streaking is based on the ionization of a target with a SAP and the consecutive streaking of the resulting electron wave packet in an intense IR field.

A typical streaking trace is shown in Fig. 2.12, calculated for the same parameters as the RABBITT trace in Fig. 2.11 but for a SAP and an IR intensity of $3 \times 10^{12}\,\mathrm{W/cm^2}$. The broad photoelectron energy distribution shows an oscillatory behavior out of phase with the IR vector potential (shown as red line). The increase in signal on the falling slopes of the oscillations stems from the up-chirp of the attosecond pulse (convention: for negative delays the SAP arrives first). Due to experimental limitations, typical streaking traces are acquired at much lower resolution in energy and delay.

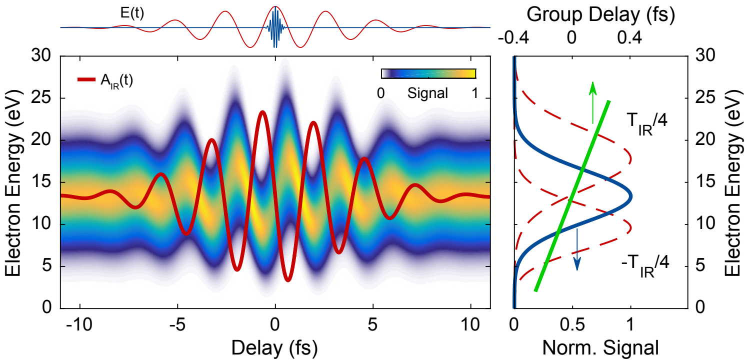

Figure 2.12: Calculated delay-dependent photoelectron spectrogram after ionization with a single attosecond pulse in presence of an IR field with an intensity of $3 \times 10^{12}\,\mathrm{W/cm^2}$. For negative delays, the SAP arrives first. The presence of the IR field leads to a shift of the final momentum distribution following the vector potential $\boldsymbol{A}$ (shown as overlay). Top: The XUV (blue) and IR field (red) in time domain for the delay $\tau = 0\,\mathrm{fs}$. Right panel: The continuous XUV spectral intensity is shown together with the positive attochirp as GD of the spectral components. The increased signal on the falling slopes of the streaking trace is a signature of the positive chirp.

Single-photon ionization of an atom with an XUV pulse results in a replication of its spectral amplitude and phase in terms of an electron wave packet shifted in energy by the ionization potential of the atom:

$$E_{\mathrm{el}} = \omega - I_{\mathrm{p}} \tag{2.12}$$

Without IR field, the unperturbed intensity spectrum of the electron wave packet does not grant insight into the underlying temporal structure. If we now apply a gating function, e.g., an IR field capable of interacting with the wave packet on the same timescale, this interaction allows to unveil the complete temporal properties as we will show in the following.

In an electric field, the canonical momentum of an electron is conserved:

$$\boldsymbol{P} = \boldsymbol{p}(t) - \boldsymbol{A}(t) \tag{2.13}$$

The asymptotic momentum of an electron wave packet ionized in presence of an IR field thus reflects the vector potential at the time of ionization:

$$\boldsymbol{p}_\mathrm{f}(\tau) = \boldsymbol{p}_0 - \boldsymbol{A}(\tau) = \boldsymbol{p}_0 + \Delta\boldsymbol{p}(\tau) \tag{2.14}$$

Here, $\boldsymbol{p}_0$ depicts the initial momentum resulting from ionization by the XUV pulse, $\boldsymbol{p}_\mathrm{f}$ with $|\boldsymbol{p}_\mathrm{f}| = \sqrt{2E_\mathrm{el}}$ is the final momentum of the electron wave packet at the detector after the IR pulse has passed, and τ is the time of ionization. This allows us to write the momentum at any time after ionization based on the final momentum as

$$\boldsymbol{p}(t) = \boldsymbol{p}_\mathrm{f}(\tau) + \boldsymbol{A}(t). \tag{2.15}$$

It is possible to derive a semi-classical description of the photoelectron spectrogram (the so-called streaking trace) based on the time-dependent Schrödinger equation for the ionization of an atom in a combined XUV and non-ionizing IR field to the following equation [69, 70, 71]:

$$S(\boldsymbol{p}_\mathrm{f}, \tau) = \left| \int_{-\infty}^{\infty} E_\mathrm{X}(t-\tau) d(\boldsymbol{p}_\mathrm{f} + \boldsymbol{A}(t)) e^{\mathrm{i}\varphi(\boldsymbol{p}_\mathrm{f},t)} e^{\mathrm{i}(\boldsymbol{p}_\mathrm{f}^2/2+I_\mathrm{p})t} \mathrm{d}t \right|^2 \tag{2.16}$$

$$\varphi(\boldsymbol{p}_\mathrm{f}, t) = -\int_{t}^{\infty} \left(\boldsymbol{p}_\mathrm{f} \cdot \boldsymbol{A}(t') + \frac{1}{2}\boldsymbol{A}^2(t') \right) \mathrm{d}t', \tag{2.17}$$

with the XUV field $E_\mathrm{X}(t)$, the XUV-IR delay τ, the dipole matrix element d for the transition from the bound to the continuum state with momentum $\boldsymbol{p}_\mathrm{f} + \boldsymbol{A}(t)$ and the ionization potential I_p.

Under the assumption, that the polarization directions of the XUV and IR field are parallel, as it is the case for a typical streaking experiment, and that the dipole transition matrix element is constant in the energy range under consideration, i.e., $d \approx 1$, Eq. 2.16 and 2.17 simplify to

$$S(p_\mathrm{f}, \tau) \approx \left| \int_{-\infty}^{\infty} E_\mathrm{X}(t-\tau) e^{\mathrm{i}\varphi(p_\mathrm{f},t)} e^{\mathrm{i}(p_\mathrm{f}^2/2+I_\mathrm{p})t} \mathrm{d}t \right|^2 \tag{2.18}$$

$$\varphi(p_\mathrm{f}, t) = -\int_{t}^{\infty} \left(p_\mathrm{f} A(t') + \frac{1}{2}A^2(t') \right) \mathrm{d}t'. \tag{2.19}$$

The dependency of $\varphi(p_\mathrm{f}, t)$ on the final momentum can be released by replacing the streaked photoelectron momentum based on Eq. 2.14 with

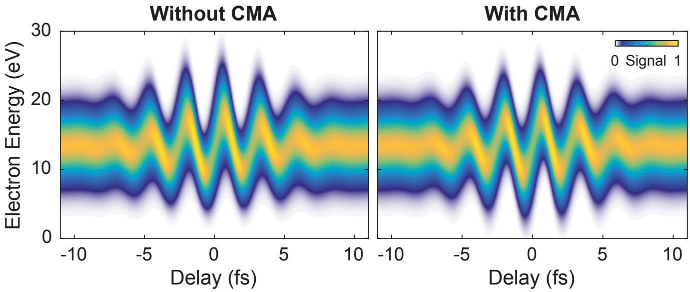

Figure 2.13: Comparison of streaking spectrograms calculated for the same parameters for the cases without (left) and with (right) application of the central momentum approximation. The CMA leads to a symmetric streaking around the central part of the unstreaked photoelectron distribution.

the initial momentum after ionization $p_\mathrm{f} = p_\mathrm{c} - A(t)$ where p_c depicts the single value central momentum of the unstreaked momentum distribution. This approximation is the so-called central momentum approximation (CMA) which is valid for low streaking amplitudes, if the bandwidth of the unstreaked photoelectron momentum distribution is small compared to it's central momentum [72]. The influence of the CMA on the spectrogram is demonstrated in Fig. 2.13, visible as change in the symmetry of the streaking along the energy axis.

The application of the CMA leads us to the final expression for the spectrogram:

$$S(p_\mathrm{f},\tau) \approx \left| \int_{-\infty}^{\infty} E_\mathrm{x}(t-\tau) e^{\mathrm{i}\varphi(t)} e^{\mathrm{i}(p_\mathrm{f}^2/2+I_\mathrm{p})t} \mathrm{d}t \right|^2 \tag{2.20}$$

$$\varphi(t) \approx -\int_{t}^{\infty} \left(p_\mathrm{c} A(t') - \frac{1}{2} A^2(t') \right) \mathrm{d}t'. \tag{2.21}$$

It now becomes evident, that Eq. 2.20 with $\omega = p_\mathrm{f}^2/2 + I_\mathrm{p}$ resembles

$$S(\omega,\tau) \approx \left| \int_{-\infty}^{\infty} P(t-\tau) G(t) e^{\mathrm{i}\omega t} \mathrm{d}t \right|^2 , \tag{2.22}$$

which represents the form of a typical frequency-resolved optical gating (FROG) trace [73] with $P(t) = E_\mathrm{x}(t)$ being the pulse and the IR acting as a pure phase gate $G(t) = e^{\mathrm{i}\varphi(t)}$ on the electron wave packet in the continuum.

This derivation including the CMA is the basis of most algorithms capable of reconstructing an attosecond streaking trace and thus enabling the temporal characterization of attosecond pulses and also the streaking IR field. It disentangles the pulse and gate functions, removes their dependence on the final energy and can be expressed as a Fourier transform of the delay-dependent product $E_\mathrm{x}(t-\tau)G(t)$.

2.5.3 FROG-CRAB Reconstruction

The frequency-resolved optical gating for complete reconstruction of attosecond bursts (FROG-CRAB) was introduced by Mairesse et al. [74] as method to use attosecond streaking for the complete temporal reconstruction of the attosecond pulse. The similarity of the fundamental structure of a streaking trace with Eq. 2.22 allows the direct application of well-established blind FROG algorithms with the specialty, that in case of FROG-CRAB, the pulse and the gate are completely independent. Furthermore, the streaking amplitude often does not vanish at the edges of the measured streaking trace.

Numerically, the spectrogram Eq. 2.22 can be represented as

$$S(\omega, \tau) = S_{nm}, \tag{2.23}$$

with $n \in [1, N]$ and $m \in [1, M]$ sampled at equidistant steps along the delay and energy axis, respectively. This matrix represents the Fourier transform of the signal matrix in time domain $\tilde{S}_{nm}$ along the pulse-time axis $S_n = \mathrm{fft}[\tilde{S}_n]$.

The goal of all iterative FROG-CRAB algorithms is to find a representation of $P(t)$ and $G(t)$ that reproduces the measured spectrogram I_{nm} at best. In order to achieve convergence to this solution, two constraints are applied at each iteration of the reconstruction: The amplitude of the reconstructed spectrogram is replaced by the measured amplitude

$$S_{nm} = \sqrt{I_{nm}} \exp(\mathrm{i} \arg[S_{nm}]), \tag{2.24}$$

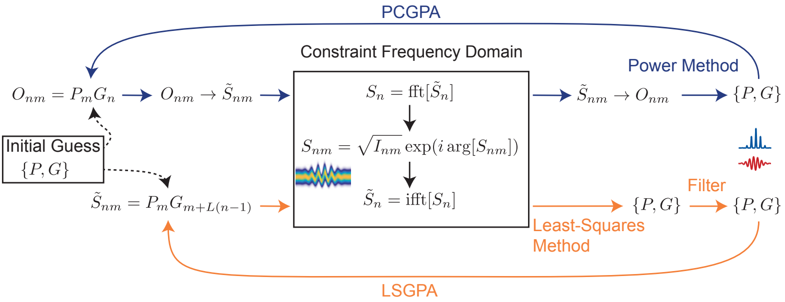

Figure 2.14: Sketch of the iterative steps used for the temporal reconstruction of attosecond pulses in a FROG-CRAB scheme based on PCGPA and LSGPA. PCGPA: Starting with an initial guess, the outer product of pulse and gate forms the matrix O_{nm} that represents a row-shifted version of the signal matrix $\tilde{S}_{nm}$. After column-wise Fourier transform, the amplitude of the frequency domain representation of the spectrogram matrix S_{nm} is replaced by the experimentally measured one. The back-transform to the time domain and the inverse row-shifting operation is the basis for the calculation of the new pulse and gate using the power method. LSGPA: The signal matrix is directly calculated based on the pulse and the gate. The frequency domain constraint is followed by the calculation of the new pulse and gate by means of the least-squares method. Before using the resulting gate in the next iteration, the fast non-physical oscillations have to be filtered by smoothing which effectively couples the different subsets of the gate together.

which can be seen as the experimental or frequency domain constraint. Secondly, in time domain $P(t)$ and $G(t)$ have to be valid choices to produce a spectrogram based on Eq. 2.22. This can be seen as the physical constraint.

One of the most common iterative reconstruction algorithms used for FROG and FROG-CRAB is the PCGPA [75, 76, 77]. It is a blind FROG algorithm that is based on the properties of the outer product of the pulse and the gate and requires a squared spectrogram $M \times M$ matrix with sampling steps that fulfill the Fourier relation $\delta\omega\delta\tau = 2\pi/M$ between the sampling step size in energy $\delta\omega$ and in delay $\delta\tau$. Figure 2.14 shows the iterative scheme of the PCGPA and of the alternative reconstruction algorithm LSGPA that will be discussed later.

Initial guesses for the reconstruction can directly be obtained from the measured spectrogram: For the pulse, the Fourier transform of the unstreaked photoelectron spectrum assuming a flat phase represents a good starting point. The initial guess for the vector potential can simply be obtained by extracting the center of mass (COM) of the streaking trace in momentum for all delays, $p_{\mathrm{com}}(\tau)$, and calculating the vector potential based on Eq. 2.14:

$$A(\tau) = p_{\mathrm{c}} - p_{\mathrm{com}}(\tau). \tag{2.25}$$

In every iteration of the PCGPA the signal matrix is calculated based on the outer product between pulse and gate $O_{nm} = P_m G_n$ which can be converted into the correct delay representation by applying a row-shift to every row of the matrix. Based on this signal matrix, the complex frequency domain representation of the spectrogram is obtained by Fourier transforming along the vertical pulse-time axis. Next, the frequency domain constraint (Eq. 2.24) is applied by replacing the amplitude of the calculated complex spectrogram with the square-root of the measured spectrogram in intensity. After an inverse back-transform to the time domain and the application of the inverse row-shift, the outer product representation of the signal matrix is used to calculate the new pulse and gate as the principal eigenvectors of $OO^\dagger$ and $O^\dagger O$ using the power method [77].

The advantage of the PCGPA algorithm is the easy and fast implementation based on the simple algebraic operations and the robust convergence. The disadvantage is the requirement of a square matrix fulfilling the conditions for the time and frequency step widths. As a consequence, an experimental trace usually has to be resampled and interpolated before providing it to the algorithm. This interpolation can lead to non-physical artifacts in the reconstruction and has especially proven to be unreliable for single-attosecond pulses of shortest duration and for those exhibiting a small satellite pulse [72]. Another intrinsic assumption of the PCGPA is the periodicity along the delay axis which is often not fulfilled for an experimental streaking trace due to a limited acquisition window.

The LSGPA has been introduced by Gagnon et al. [72] as an alternative to overcome the assumption of periodicity and the oversampling issue of the PCGPA by relaxing the time-frequency-step constraint and allowing the delay step width to be an integer multiple of the Fourier relation step width $\delta\omega\delta\tau = 2\pi L/M$ with $L \in [1, 2, \dots]$ and a $N \times M$ spectrogram matrix.

In its essence, the LSGPA is based on a signal matrix where the rows are calculated based on different sub-sets of the gate. The application of the frequency domain constraint is performed in the same way as for the PCGPA. Afterwards, the calculation of a new pulse and gate pair is based on the least-squares method minimizing the least-squares error between the new and the previous signal matrix. In this step, effectively L subsets of the gate are calculated based on L subsets of the pulse and the signal matrix, visible as fast oscillations in the new gate. These unphysical fast oscillations have to be averaged out before using the gate for the calculation of the next signal matrix and pulse. This averaging is implemented as separate smoothing of the amplitude and phase along the delay axis which effectively couples the different subsets of the gate with each other. This last step is the most sensitive part of the LSGPA reconstruction as too little or too much smoothing prevents convergence of the algorithm.

For both algorithms PCGPA and LSGPA, a good convergence is typically reached after few thousand iterations. The time for reconstruction on a modern computer is mainly defined by the speed of the Fourier transform and thus directly depending on the size of the matrix. For a matrix with 1024 points along the energy axis, the algorithms running for 20000 iterations take about 10 minutes for the LSGPA and about 30 minutes for the PCGPA. Both algorithms are capable of retrieving the full XUV spectrum in amplitude and phase and at the same time the IR waveform.

In chapter 5, we introduce a novel scheme for the temporal reconstruction of attosecond pulses that is based on time-domain ptychography. With this technique, called attosecond ePIE, the constraints on the sampling steps along the delay axis are reduced even further and convergence is achieved in minimal time with a large tolerance on noise in the experimental streaking trace. We present an introduction to this technique as well as a comparison with the established algorithms PCGPA and LSGPA.

Chapter 3

Experimental Setups

The experimental studies presented in this thesis have been conducted with the help of two different setups. The measurements on strong-field ionization in the long-wavelength limit were driven by a purpose-built mid-infrared optical parametric chirped pulse amplification (OPCPA) system in combination with a velocity map imaging spectrometer (VMIS) optimized for high electron energies. The experiments with attosecond pulses and high-order harmonic generation (HHG) have been carried out at the attoline, our versatile attosecond pump-probe beamline driven by a commercial Ti:sapphire chirped pulse amplification (CPA) system. This chapter is used to introduce both experimental setups as they form the foundation of all results presented in this thesis.

3.1 Momentum Spectroscopy in the Mid-Infrared

3.1.1 Mid-Infrared Source

In contrast to high-intensity sources in the near-infrared (NIR) and their broad commercial availability, table-top mid-infrared (MIR) laser systems that allow high peak intensities on the order of $10^{13}\,\mathrm{W/cm^2}$ are still subject to intense research and development. The most promising path to achieve few-cycle pulses at wavelengths above $3\,\mu\mathrm{m}$ is the OPCPA. Here, we present a brief overview of the OPCPA system that was developed in order to perform the strong-field ionization experiments in the long-

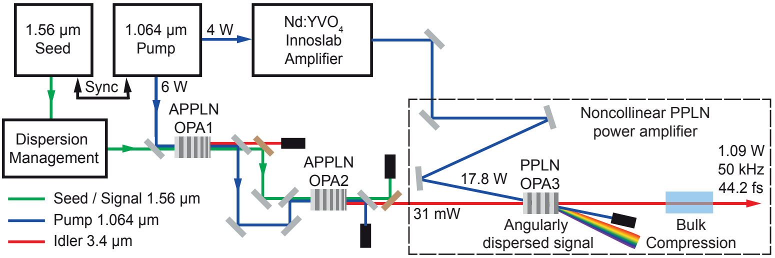

Figure 3.1: Scheme of the OPCPA based on three quasi-phasematched OPAs pumped at 1064 nm wavelength. The dashed rectangle depicts the power amplifier stage with consecutive compression of the amplified idler. Adapted from [78].

wavelength regime presented in Chapter 4. It delivers sub-four-cycle pulses with a pulse energy of 21.8 μJ and a duration of 44 fs at a central wavelength of 3.4 μm and 50 kHz repetition rate.

The system is based on a series of three quasi-phase matching (QPM) optical parametric amplification (OPA) stages pumped at a wavelength of 1064 nm with a seed wavelength of 1560 nm (Fig. 3.1). The seed is first spectrally broadened in a dispersion compensated fiber and then chirped in a pulse shaper in 4f-geometry and a silicon prism pair. The first two OPA stages constitute the pre-amplifiers and are realized in a collinear geometry based on apodized aperiodic periodically poled lithium niobate (APPLN) gratings whereas the power amplification of the 2nd stage idler pulses is based on a non-collinear geometry and a periodically poled

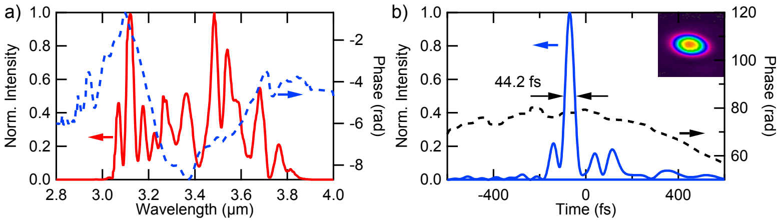

Figure 3.2: Spectral a) and temporal b) characteristics of the OPCPA pulses based on a SHG-FROG [73]. The spectral bandwidth is 800 nm centered around 3.4 μm wavelength. The corresponding pulse duration has been reconstructed to be 44.2 fs. Adapted from [78].

lithium niobate (PPLN) crystal. The resulting amplified idler pulses exhibit a bandwidth of 800 nm and are compressed to the final pulse duration by transmission through a 5-cm bulk sapphire rod. The final spectral and temporal profile of the amplified pulses is shown in Fig. 3.2.

More details on the OPCPA system can be found in [78, 79] and recent developments covering the extension to amplification in the frequency domain are presented in [80].

3.1.2 Velocity Map Imaging Spectrometer

The velocity map imaging technique was first introduced by Eppink and Parker in 1997 [82, 83]. It enables the measurement of complete photoelectron momentum distributions (PMDs) which are projections of the full three-dimensional momentum distributions along one dimension. It is based on an electrostatic lens consisting of three electrodes, namely repeller, extractor and ground. For a well-defined geometry and electric potential of all three electrodes, the resulting electric field distribution is capable of projecting the momentum vector of all electrons or ions within a certain focal volume onto an image plane. A detector in this plane is then used to amplify and visualize the imaged charges by means of a micro-channel plate (MCP) and a phosphor screen.

A sketch of the VMIS used in our lab can be seen in Fig. 3.3. It consists of a ultra-high vacuum (UHV) chamber containing an inner compartment with mu-metal shielding for the vertical field-free flight tube. On the right-hand side, an entrance window allows the coupling of the laser beam into the chamber. Inside, it is focused into the interaction region by means of a back-reflecting concave mirror on a movable mounting. The target gas is released into the chamber through an effusive gas nozzle that is integrated into the repeller electrode [84]. This configuration leads to an enhanced target gas density which improves the acquisition rate.

After ionization of the target gas by the incoming laser pulses, the resulting PMD is imaged onto the detector by means of an electrostatic lens. The exact geometry and electrostatic potential of the three electrodes has been calculated and optimized with help of the software SIMION. At typical potentials of $-3 \ldots -13\,\mathrm{kV}$ for the repeller and $-2.6 \ldots -11.5\,\mathrm{kV}$ for

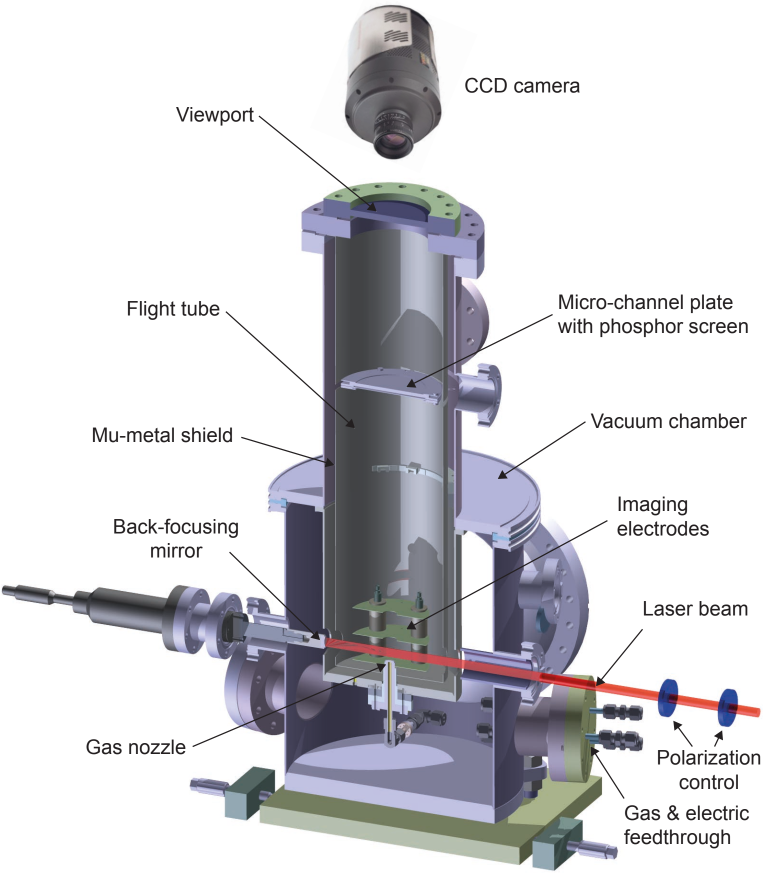

Figure 3.3: Rendering of the VMIS used in the strong-field experiments presented in this thesis. A back-focusing geometry is used to focus the incoming laser beam into the interaction region where it ionizes the target gas released into the chamber by a gas nozzle integrated into the repeller plate. The combination of three electrodes is used to image the resulting photoelectron momentum distribution onto a micro-channel plate with consecutive phosphor screen. The viewport on top of the device is used to digitize the projected distribution on the phosphor screen with the help of a CCD camera. Adapted from [81].

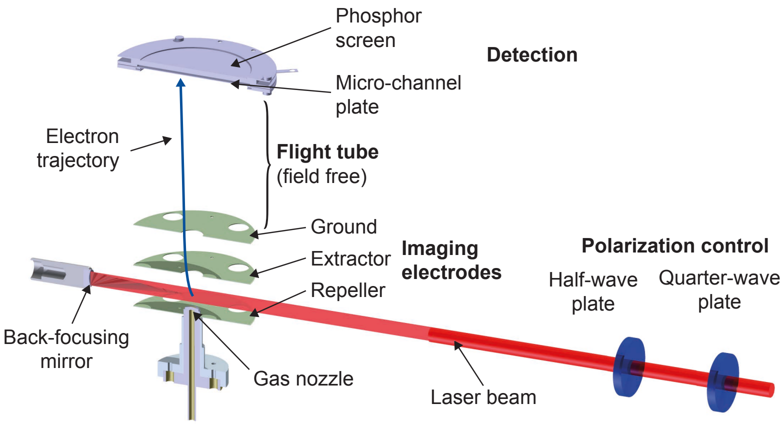

Figure 3.4: Detailed view of the interaction region and the imaging electrodes as cut through the device. The laser pulses are focused into the center between the repeller and the extractor plate, about 3 mm above the gas nozzle, from where the electrons start their trajectory towards the detector. The quarter- and half-wave plates are used for polarization control and tomographic imaging for the reconstruction of the full three-dimensional momentum distribution.

the extractor electrode with the third plate on ground potential, momentum imaging of electrons up to $p = 2\,\text{a.u.}$ can be achieved. This is equivalent to a kinetic energy of about 54 eV. The micro-channel plate is used to amplify the signal of the impinging charges and the integrated phosphor screen allows the photographic imaging through the viewport on the top of the VMIS. The calibration of the VMIS is performed with the help of momentum distribution resulting from above-threshold ionization (ATI) in linear polarization and the well-defined signature stemming from absorption of $N, N+1, N+2, \ldots$ photons.

A detailed view of the interaction region, the gas nozzle and the electrodes is shown in Fig. 3.4 as cut through the setup. In combination with the control of the polarization of the ionizing pulses, the setup can be used for tomographic imaging of the three-dimensional PMD [85, 86]. We therefore use a computer-controlled quarter- and half-wave plate on the outside of the chamber to turn the polarization in steps of 2° and acquire projections of the resulting momentum distribution along multiple directions spanning 180°. These projections can then be used in a filtered back-projection algorithm to reconstruct the full three-dimensional PMD [87].

The maximal electron energy observed in the experiment scales with the ponderomotive energy U_p. Thus, longer wavelengths lead to much higher electron momenta and require the adjustment of the imaging geometry. To switch between high-resolution velocity map imaging of a small momentum space suitable for experiments at wavelengths of 800 nm and lower resolution momentum imaging up to high electron energies ($E_\mathrm{el} > 0.5\,\mathrm{a.u.}$), the distance between the MCP and the focal region can be adapted. Typical experimental photoelectron momentum distributions can be found in Chapter 4.

The VMIS presented in this section has proven to be a versatile tool for strong-field experiments at wavelengths of 800 nm [88, 38] and those at 3.4 μm presented in this thesis. More details on the setup and the tomographic imaging can be found in [81].

3.2 Attosecond Spectroscopy

3.2.1 Laser System

The laser system that supplies the attoline with infrared (IR) femtosecond pulses consists of a CEP-stabilized titanium-doped sapphire (Ti:sapphire) oscillator (Femtolasers Femtosource Rainbow) and a consecutive two-stage chirped pulse amplification (CPA) system delivering pulses with energies up to 10 mJ at 1 kHz repetition rate. A scheme of the setup is presented in Fig. 3.5. The Ti:sapphire oscillator is pumped by a 3 W continuous wave (cw) diode-pumped solid-state laser (DPSSL) at 532 nm wavelength where an acousto-optic modulator (AOM) introduced into the pump beam is used to modulate the pump power in order to achieve the fast loop carrier-envelope phase (CEP) stabilization of the system. The oscillator delivers 7-fs pulses based on Kerr lens mode-locking (KLM) with about 2.8 nJ pulse energy at a repetition rate of 77 MHz. These pulses are stretched to about 7 ps pulse duration before entering the first amplification stage consisting of ten passes through a Ti:sapphire crystal pumped by a Q-switched Nd:YLF laser with 20 W of average power.

During the first four passes, the full 77 MHz pulse train is amplified

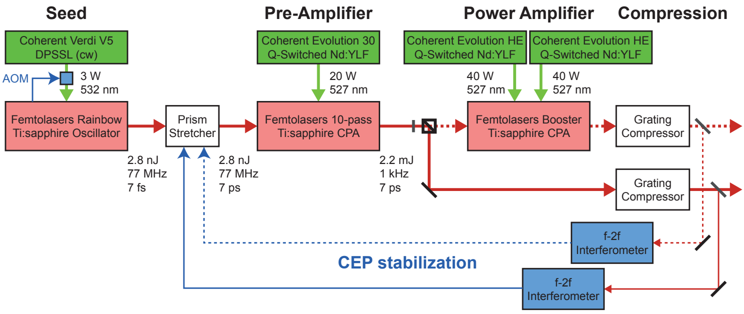

Figure 3.5: Overview of the laser system used for high-order harmonic generation and pump-probe experiments. It consists of a Ti:sapphire oscillator and a two-stage chirped pulse amplification system that delivers up to 10 mJ pulses at 1 kHz repetition rate and a pulse duration of 25 fs. In order to deliver CEP-stabilized pulses it uses a fast loop acting on the pump of the oscillator and a f-to-$2f$ CEP detection after the grating compressor with a feedback to the prism stretcher.

and then guided through a combination of a Pockels cell and an acousto-optic programmable dispersive filter (AOPDF) (Fastlite DAZZLER) acting as a pulse picker and pulse shaper. The amplification in the last six passes is performed on a reduced pulse train with 1 kHz repetition rate. The output pulses of up to 2.2 mJ can either be used as seed of the power amplification stage or coupled out towards the experiment. The power amplification stage uses a cryogenically cooled Ti:sapphire crystal pumped by 2×40 W at 527 nm wavelength and delivers pulses with up to 13 mJ of pulse energy before compression. The output pulses of the amplification stages are compressed by means of a transmission grating compressor to their final duration of 25 fs.

The whole laser system, from the oscillator to the compressed output of the amplification stages, is designed to be used in a CEP stabilized mode. The oscillator possesses the so-called fast-loop acting on the modulation of the pump power with the help of the AOM to stabilize the phase-slip per roundtrip in the cavity to $\pi/2$. The amplification stages require further control of the CEP to compensate for slow drifts. Therefore, a part of the compressed output beams is guided into an f-to-$2f$ interferometer capable of extracting the CEP value based on the interference of a part of the fundamental spectrum f and a part based on the second harmonic of

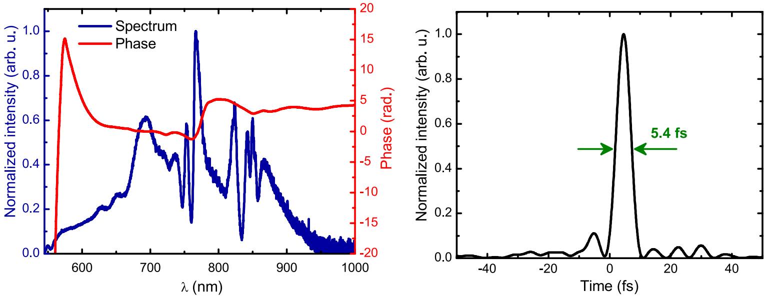

Figure 3.6: Spectral and temporal properties of the laser pulses after filamentation and compression by several bounces on chirped mirrors. The characterization has been performed with the SPIDER technique [89]. In this pulse compression scheme, we reach pulse durations of 5.4 fs, close to the Fourier limit. Adapted from [90].

the long-wavelength region of the spectrum f' with $2f' = f$. The extracted CEP value can be used in a closed-loop operation by applying a change in the dispersion of the prism-stretcher based on a piezo-electric actuator.

For some applications, the pulses delivered by the laser system have to be compressed in time to a duration of few femtoseconds. In order to achieve the spectral bandwidth necessary to support such short pulse durations, we exploit the spectral broadening due to self-phase modulation (SPM) during the interaction of the pulses with a gaseous environment. We therefore focus the laser pulses into two meter-long gas cells typically filled with argon gas at pressures around 500 mbar.

The propagation in the gas cells leads to two complementary nonlinear effects around the focus: the Kerr effect causes self-focusing of the beam in the region of high intensity due to the nonlinear contribution $n_2 I$ to the refractive index

$$n(I) = n_0 + n_2 I. \tag{3.1}$$

At the same time, the emerging plasma density due to the ionization of the gas leads to defocusing of the beam. The interplay of both mechanisms results in an extended range of interaction of the high-intensity beam with the gas and thus to efficient SPM and spectral broadening, called filamentation.

The pulses after spectral broadening feature a strong chirp that can be compensated by several bounces on chirped mirrors in order to reach the compressed pulse duration of 5.4 fs (Fig. 3.6) suitable for the generation of single attosecond pulses employing the polarization gating (PG) technique.

Details on pulse characterization techniques for optical pulses, namely frequency-resolved optical gating (FROG) and spectral phase interferometry for direct electric-field reconstruction (SPIDER), can be found in [73, 89]. Additionally, the newer self-referenced spectral interferometry (SRSI) technique [91] is applied in our lab supporting the characterization of pulses with durations down to 4 fs.

3.2.2 The attoline Setup

The attoline is a versatile XUV-IR-pump-probe beamline allowing for the simultaneous measurement in two different interaction regions by means of refocusing of the beams. Figure 3.7 shows the overall setup composed of a series of vacuum chambers that will be discussed in two sections: the front part consists of the high-order harmonic generation and the preparation of the pump and probe pulses whereas the second part contains the experimental chambers and the analysis of the extreme ultraviolet (XUV) radiation. More details can be found in [90].

All the vacuum chambers of the attoline are designed and connected in a differential pumping scheme that allows a high pressure of 2×10^{-3} mbar in the generation chamber under load during HHG and at the same time pressures as low as 5×10^{-8} mbar in the first experimental chamber and below 10^{-10} mbar in the 2nd experimental chamber as required for experiments on solid state surface dynamics.

The first four compartments are shown in detail in Fig. 3.8. The incoming laser beam is split up into a high-intensity part for the high-order harmonic generation and a part that is used for the time-delayed IR pulses in pump-probe experiments. We first pass the generation beam through a combination of a quartz and a quarter-wave plate as required for the generation of single-attosecond pulses with the PG technique. By turning the quartz plate, the polarization state of the generating IR pulses can be

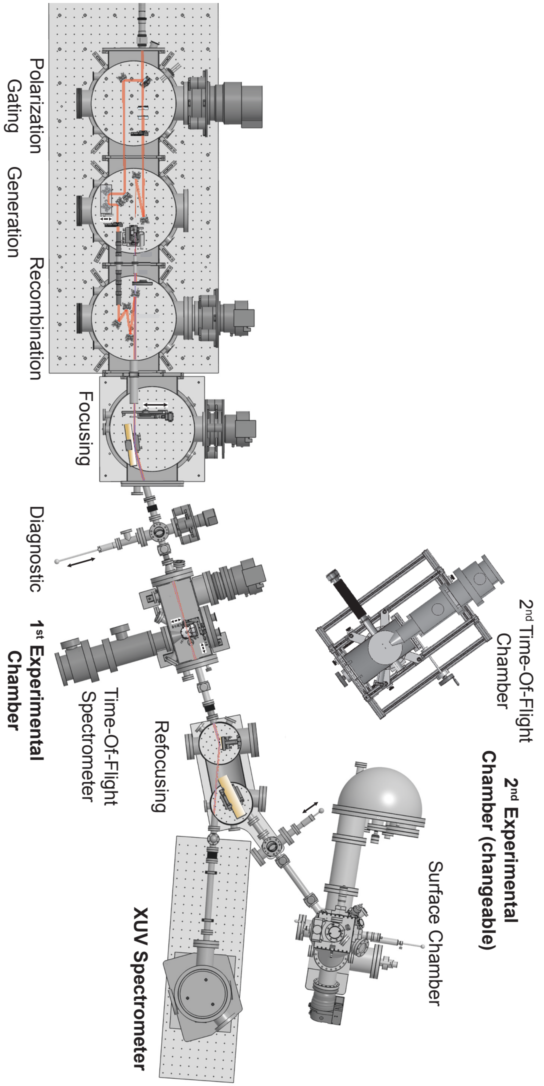

Figure 3.7: Overview over the different compartments of the attoline. Details are given in the text. Adapted from [90].

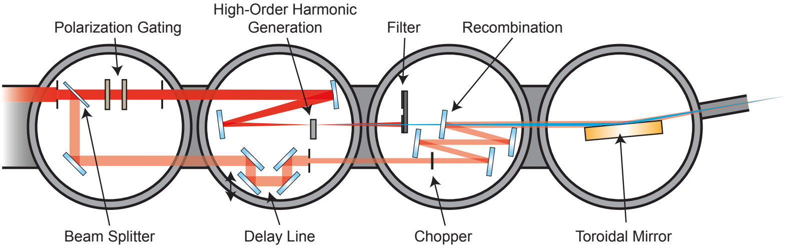

Figure 3.8: Detailed view of the first four vacuum chambers of the attoline. The first one is used to split up the incoming IR pulses into a high-intensity part for the HHG and a low-intensity part for pump-probe experiments. The polarization gating is implemented in the generation beam path before focusing into the target gas cell. The resulting harmonic radiation is recombined with the time-delayed IR pulses and then focused by a toroidal mirror into the experimental region.

adjusted to choose between the generation of attosecond pulse trains or single attosecond pulses.

After passing through a motorized iris for intensity control, the pulses are focused into a point in front of the target gas cell that is filled with few mbar of a noble gas, where the HHG takes place. Phase-matching of the short trajectories (see Sec. 2.3.2) can be achieved by adjusting the position of the gas target along the beam, by changing the gas pressure and the pulse intensity. The intrinsic attochirp of the harmonic radiation is compensated by transmission through an aluminum foil with a thickness of 100 nm which possesses a negative GDD in the XUV spectral region [92]. At the same time, this metallic filter is used to block the residual IR from the generation.

Besides the aluminum foil, different metallic filters can be applied in order to shape the XUV spectrum to fit specific experimental needs. Figure 3.9 shows the transmissions for selected metals as a function of the photon energy.

After the filter, the freely propagating harmonic beam passes through a drilled mirror which is used to recombine the XUV beam with the divergence-matched IR beam. The pulses in the IR beam arrive at the same time as the XUV pulses, variable by a piezo-electric delay stage with a resolution of about 20 as.

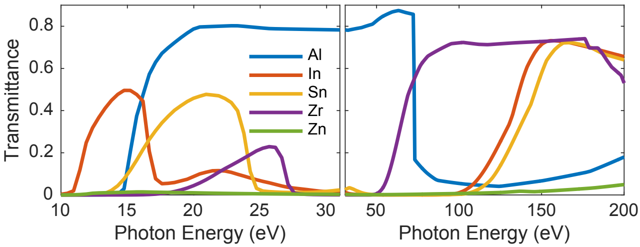

Figure 3.9: Transmittance for the metals aluminum (Al), indium (In), tin (Sn), zirconium (Zr), and zinc (Zn) in the VUV and XUV range for a thickness of 100 nm. Typical metal filters applied in the experiment are aluminum for blocking the residual IR and tin for shaping the XUV spectrum. Data taken from [93].

The whole interferometric part of the attoline is placed on a temperature-stabilized base plate in order to minimize temporal drifts in the pump-probe overlap. Furthermore, it has recently been extended with an active interferometric stabilization based on a co-propagating cw laser beam with a wavelength of 473 nm [68].

The last chamber of the attoline front-end contains the toroidal mirror that is used to focus the collinearly propagating attosecond XUV and femtosecond IR pulses into the first experimental region. Additionally, it accommodates an optional calibrated photo diode to measure the XUV pulse energy and an imaging MCP used to visualize the XUV spatial beam profile.

An insertable mirror on the way to the experimental chamber enables us to couple out the IR pulses in order to set and observe the overlap of the pump and probe pulses in the focal plane and to determine the coarse adjustment of the temporal overlap.

The first experimental vacuum chamber hosts a time-of-flight spectrometer (TOF) (Kaesdorf ETF11) used for gas-phase photoelectron/photoion experiments. The target gas is released into the UHV chamber by an effusive nozzle positioned just above the focus of the XUV and IR beams and the TOF collects the charged particles resulting from ionization with the help of an electrostatic lens and guides them to the detection MCP. The signal is read out by a digital timing unit (Fast ComTec P7889) for

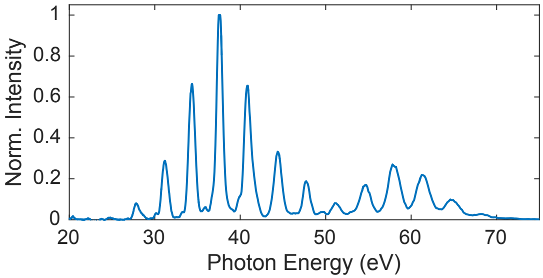

Figure 3.10: Typical XUV high-order harmonic spectrum for generation in argon after transmission through an aluminum filter.

the electrons or a digitizer card (Agilent U1071A) for the ions. A repeller electrode ensures the efficient collection of the ions.

The gas nozzle in the first interaction region can be replaced by a piezo-driven pulsed gas cell used for gas-phase transient absorption experiments or by a thin solid-state target for transient absorption experiments.

After the first interaction region, we use a spherical mirror to focus the XUV pulses into the entrance slit of the XUV spectrometer consisting of a grating (450 grooves/mm) and a CCD camera (Princeton Instruments PIXIS-XO 400B). A typical XUV spectrum can be seen in Fig. 3.10.

One key feature of the attoline is the possibility to re-image the first focus into a second interaction region that can be used for experiments on solid-state targets [90] or in a second gas-phase experiment. In this configuration, two simultaneous measurements can be carried out among those one usually serves as reference for a second less-known system under investigation. Thereby, photoionization-delay experiments based on the reconstruction of attosecond beating by interference of two-photon transitions (RABBITT) technique (Sec. 2.5.1) on, e.g., solid state targets with a noble gas reference experiment in the first chamber can be realized [17, 94]. To guide the beam into the second chamber, the spherical mirror in front of the spectrometer can be removed from the beam. Thereby, a second toroidal mirror refocuses the XUV and IR pulses into the interaction region of a mobile end station located next to the optical table (Fig. 3.7).

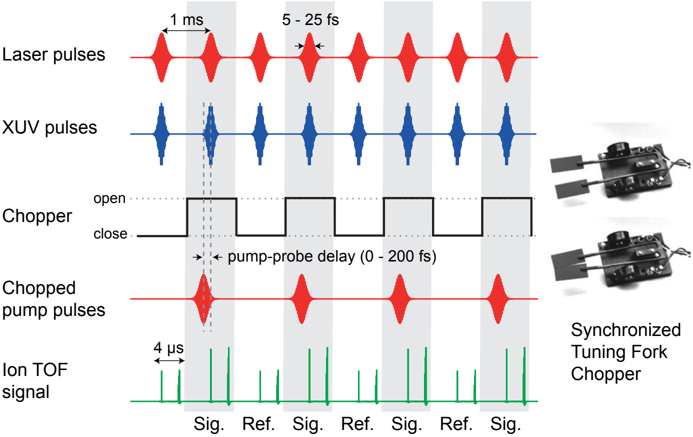

Figure 3.11: The generation of high-order harmonic radiation is intrinsically phase-locked to the IR pulses. A variable delay on the IR beam path enables pump-probe measurements with attosecond resolution. The tuning-fork chopper that is synchronized to the laser system operates at half its repetition rate and thus blocks every second IR pulse. The resulting signal consists of alternating parts containing XUV-only and full XUV-IR-pump-probe data that can be acquired separately by a fast acquisition card.

Significant contributions to the quality of the acquired data and the signal-to-noise ratio (SNR) include long-term effects caused by temperature drifts of the environment and mechanical shifts over the day as well as short-term fluctuations of the signal due to vibrations caused by the indispensable turbo pumps, fluctuations in the laser pulses or the generation gas pressure. One technique that has been implemented to increase the SNR of the measured data from the TOF, is the integration of a tuning-fork chopper into the IR beam path. This tuning-fork chopper is oscillating at a frequency of half the laser repetition rate synchronized to the laser system. It thus blocks every second IR pulse which allows us to acquire reference (XUV only) data in alternation with full pump-probe data (Fig. 3.11). This principle is based on the fast digitizer card that receives the current status (open or closed) from the chopper in parallel with the data and is thus able to sort and tag it accordingly. The separate averaging and treatment of the data is then performed in real-time by a homebuilt software on the data acquisition computer.

For experiments, where the IR-induced effect on the signal is very small compared to the overall signal amplitude, this acquisition scheme leads to a significant increase in the data quality and enabled the studies presented in Chapter 7.

Chapter 4

Breakdown of the Dipole Approximation in Strong-Field Ionization

In this chapter, we explore effects in the long-wavelength regime in strong-field ionization. We therefore apply the mid-IR OPCPA source in order to ionize noble gases at a wavelength of 3.4 µm and intensities on the order of 10^{13} W/cm^2. Photoelectron momentum distributions were recorded by velocity map imaging and projected onto the beam propagation axis. We observe an increasing shift of the peak of this projection opposite to the beam propagation direction with increasing laser intensities. From a comparison with semiclassical calculations, we identify the combined action of the magnetic field of the laser pulse and the Coulomb potential as origin of our observations. The significance of the magnetic field component of the laser pulses implies the breakdown of the dipole approximation at surprisingly low intensities. Parts of this chapter have been published in [95].

4.1 Introduction

The electric dipole approximation is a concept widely used to facilitate calculations and the understanding of processes involved in light-matter interactions in atomic, molecular and optical physics. In its essence, it assumes that the relevant length scales associated with the target are small compared to the wavelength of light. In particular, theoretical descriptions

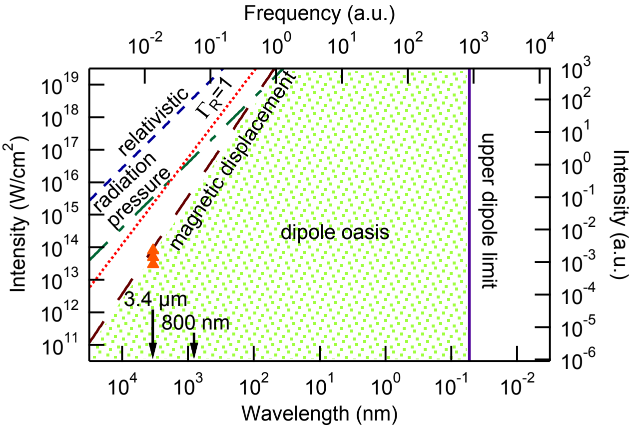

Figure 4.1: Illustration of the wavelength-intensity parameter space in strong-field ionization, taking the magnetic field component into account. The area where the dipole approximation is considered as valid (“dipole oasis”) is depicted as green dotted region. The well-known short-wavelength dipole limit arises for wavelengths on the order of the atomic scale, i.e., for $\lambda = 1\,$a.u.. The long-wavelength limit arises due to the laser magnetic field component, and is characterized by the ratio $U_\mathrm{p}/2\omega c = 1\,$a.u.. The experiment presented in this chapter was performed at a wavelength of 3.4 µm at intensities close to this limit (orange triangles). The radiation pressure limit arises for $U_\mathrm{p}^2/2c^2 = 0.5\,$a.u., and true relativistic effects start to occur around $2U_\mathrm{p}/c^2 = 1\,$a.u. [26]. The parameter $\Gamma_\mathrm{R} = (U_\mathrm{p}^3 I_\mathrm{p})^{1/2}/3c^2\omega$ indicates the limit where the spatially spread electron wave packet essentially misses the ion under the influence of the magnetic field [97]. Adapted from [95].

of strong-field ionization build heavily on this approximation and it usually holds well for the most commonly used near-infrared laser sources and intensities [96]. While the breakdown of the dipole approximation towards short wavelengths, where the wavelength becomes comparable to the target size, can be expected, a lesser-known limit also exists towards long wavelengths [24, 25, 26].

In the dipole approximation, the vector potential $\boldsymbol{A}(t)$ that describes the laser field is spatially homogenous and thus, the magnetic field component of the laser field is zero, since $\boldsymbol{B} = \nabla \times \boldsymbol{A}(t) = 0$. Consequently, the magnetic field component of the laser field is neglected in all considerations building on this approximation. However, because the magnetic-field component of the Lorentz force acting on the electrons exposed to the laser light depends linearly on the ratio p/c with the electron’s momentum p and the speed of light in vacuum c, high-energy electrons are strongly influenced by the magnetic field. Moreover, such high-energy electrons inevitably occur in strong-field ionization using intense long-wavelength driving lasers. Thus, at long wavelengths, the dipole approximation is expected to break down in strong-field ionization due to the onset of magnetic field effects.

Criteria that characterize the onset of magnetic field effects as well as the onset for fully relativistic treatment of the ionization process have been formulated [24, 25, 98, 26]. The commencement of fully relativistic behavior can be characterized by twice the ponderomotive energy approaching the rest energy of the electron, i.e.,

$$\frac{2U_\mathrm{p}}{c^2} = \frac{I}{2\omega^2 c^2} = 1 \tag{4.1}$$

with I the peak intensity and ω the carrier frequency of the laser pulse.

The onset of the influence of the magnetic field effects, however, becomes noticeable already at significantly smaller intensities and higher frequencies than those required to achieve this condition. In particular, the limit of the dipole approximation for long wavelengths is reached when the magnetic field induced amplitude of a free electron's motion in the frame where the electron is in average at rest becomes 1 a.u. [24, 25, 26], i.e.,

$$\frac{U_\mathrm{p}}{2\omega c} = 1\,\text{a.u.} \tag{4.2}$$

These relativistic and non-relativistic limits of the dipole regime are shown in Fig. 4.1.

Due to the widespread deployment of Ti:sapphire laser systems, the majority of experiments in strong field science are performed at wavelengths around 800 nm, where the dipole approximation is considered to be valid for intensities of at least $5\times10^{15}\,\mathrm{W/cm^2}$ [24].

Non-dipole effects in strong-field ionization have been subject to a number of works by various groups. Such effects have been observed experimentally for the case of multiply charged ions in ultra-high-intensity beams at wavelengths of 800 nm [99, 100, 101] and 1053 nm [102, 103]. They have been studied purely theoretically for XUV pulses [104], in the frame of calculations on photoelectron rescattering processes [97, 105, 106, 107], and laser driven ion dynamics [108]. Furthermore, studies of non-dipole effects have often assumed a negligible influence of the Coulomb potential, as was recently the case in an experiment for circularly polarized light at 800 nm and 1.4 µm [27], and in theoretical investigations [24, 25, 109]. Here, we present an experimental study of non-dipole strong-field ionization for the important case of linearly polarized light with few-cycle pulses at a mid-infrared (mid-IR) wavelength, where the Coulomb potential of the residual ion is of significant importance as well as the laser's magnetic field. A solid understanding of the case of linearly polarized light at long wavelengths is of considerable importance for all phenomena relying on electron recollision processes such as the generation of x-ray high harmonic radiation and attosecond pulses [22], holography with photoelectrons [19] and laser-induced diffraction [110, 37].

4.2 Experiment

In this chapter, we study non-dipole effects on complete photoelectron momentum distributions (PMDs) from strong-field ionization of noble gases with few-cycle mid-IR pulses at moderate intensities. We show that these PMDs exhibit clear evidence for the influence of the magnetic field component of the laser pulse. To access the long-wavelength limit of the dipole approximation, we developed a state-of-the-art optical parametric chirped-pulse amplifier (OPCPA) system based on chirped quasi-phase-matching (QPM) devices, as described in detail in Sec. 3.1.1 and in [79, 78].

The pulses with a duration of 44 fs, and a pulse energy of 21.8 µJ and a center wavelength of 3.4 µm at a high repetition rate of 50 kHz were guided into the velocity map imaging spectrometer (VMIS) described in Sec. 3.1.2 [82, 84, 81] and focused into the interaction region by a dielectric mirror with a focal length of 15 mm. The resulting photoelectrons were mapped onto a micro-channel plate, imaged by a successive phosphor screen and recorded with the help of a charge-coupled device (CCD) camera.

We recorded PMDs from the noble gases xenon, argon, neon and helium in an intensity range of 2–8$\times 10^{13}$ W/cm^2 and observed an asymmetry of the photoelectron images along the beam propagation axis with

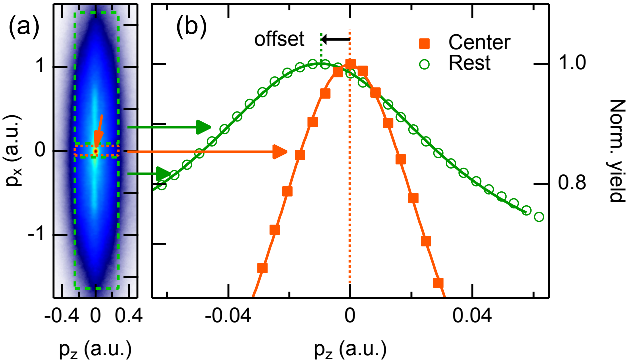

Figure 4.2: (a) Typical projected photoelectron momentum distribution (PMD) of xenon recorded at an intensity of 6×10^{13} W/cm^2 with linear polarization using a VMIS at a center wavelength of 3.4 µm. We show the plane spanned by the laser polarization (labeled p_x) and propagation (labeled p_z) direction. The orange arrow depicts the center spot resulting from field-ionization of highly-excited Rydberg states used as reference for p_z=0 a.u., and the dashed boxes indicate the areas taken for the momentum-offset analysis. (b) Projections of the PMD onto the beam propagation direction together with Lorentzian fits. The orange curve (squares) is used to set the p_z=0 a.u. reference and the offset of the maximum of the photoelectron distribution is extracted from the fit on the green markers (circles). Adapted from [95].

respect to our reference, which is the center spot as marked in Fig. 4.2(a). The center spot location corresponds to low-energy electrons that originate from highly excited states that remain after the interaction with the laser pulse [27, 111, 112]. The electric field of the spectrometer ranges from 0.5–1 kV/cm and can thus field-ionize excited states with a binding energy that corresponds to a principal quantum number of n=21 or higher [113]. As these electrons do not gain kinetic energy in the detector plane and do not interact with the laser pulse after ionization, they can be used as a reference point for zero momentum of the photoelectrons [27].

In order to quantify the asymmetry in the experiment we projected the two-dimensional PMDs onto the axis of beam propagation z and extracted the offset of the peak of the projected distribution with respect to the central reference spot as depicted in Fig. 4.2(a). For that reason the PMDs were split along the laser polarization direction x into a central slice with a width of $\Delta p_x = 0.05$ a.u. (to isolate the central spot), and the two outer regions (that exhibit the offset of the peak in beam propagation direction). As illustrated in Fig. 4.2(b) the positions of the maxima were extracted by fitting the peak regions in a range of $\Delta p_z \approx 0.05\,\text{a.u.}$ with a Lorentzian function in each case. Here the peak of the central slice simply defines p_z=0 a.u. so we further concentrate our analysis on the offset of the peak of the rest of the PMDs as function of laser intensity. The error of this procedure was estimated from the camera pixel size. The intensity was calibrated via the longitudinal width of the PMDs on the basis of semiclassical calculations described in the following section. In order to prevent the influence of interferences that occur for linear polarization, this longitudinal width was calibrated with measurements and simulations performed for circularly polarized light.

4.3 Simulation

For comparison with the data we performed classical trajectory Monte Carlo (CTMC) simulations of electrons using an established semiclassical two-step model [114, 47, 115, 116]. As initial conditions, we used the tunnel exit as it is calculated in parabolic coordinates [117, 118] with the ionization rate and the initial momentum distribution from the ADK-theory [119, 120]. Here, the tunnel ionization probability is

$$W_{\text{ADK}}\,(E) = \frac{C_l^2}{2^{|m|}|m|!}\frac{(2l+1)(l+|m|)!}{2(l-|m|)!}\cdot \frac{1}{\kappa^{(2Z/\kappa)-1}}\left(\frac{2\kappa^3}{E}\right)^{(2Z/\kappa)-|m|-1} e^{-2\kappa^3/3E} \tag{4.3}$$

as a function of the electric field E, the nuclear charge number Z, the quantum numbers l and m and $\kappa = \sqrt{2I_\text{p}}$. The coefficient C_l is the amplitude of the electron wave function in the tunneling region [121]. Barrier suppression for high intensities was accounted for by the correction

$$W_{\text{BS}}\,(E) = W_{\text{ADK}}\,(E) e^{-\alpha(Z^2/I_\text{p})(E/\kappa^3)} \tag{4.4}$$

with the empirical factor α tabulated in [121]. Figure 4.3 shows an example of the ionization rate calculated for the experimental laser parameters and an intensity of $6 \times 10^{13}\,\text{W/cm}^2$.

The initial momentum spread in the direction perpendicular to the tun-

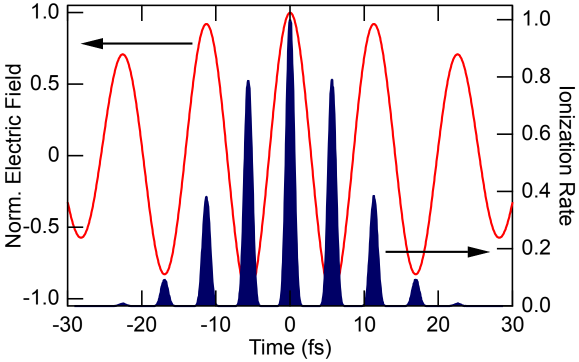

Figure 4.3: Calculated ADK ionization rate for xenon and a laser pulse matching the experimental conditions at an intensity of $6 \times 10^{13}\,\mathrm{W/cm^2}$. The high non-linearity effectively limits ionization to the strong central cycles of the field.

neling direction is

$$\sigma_\perp = \sqrt{\frac{\omega}{2\gamma}} \tag{4.5}$$

based on the Keldysh parameter γ.

Despite theoretical models that describe tunnel ionization beyond the dipole approximation [122, 123, 124], the validity of this model, that provides our initial conditions for the CTMC simulations, was questioned [24, 26]. Thus, we tested the robustness of our simulation results against variations of the spatial starting point for the propagation and variations in the ionization rate considerably beyond the change expected for relativistic tunneling. We therefore varied the exit point between 60 and 300% and the ionization rate by at least 5 orders of magnitude.

As the outcome was found to be robust against these variations, we can exclude any significant influence due to deviations from the initial conditions. The robustness of our results against details in the geometry or dynamics of the ionization step is further emphasized by the similarity of the data for the different gas species, whose ionization threshold varies considerably. Therefore, we can conclude that the dominant contribution to the observed asymmetry of the PMDs rather originates from the propagation of the liberated electrons under the influence of the combined Coulomb and laser field.

In our model, the magnetic field component of the laser pulse is fully included during the propagation in the combined fields of the laser pulse and the residual ion:

$$\ddot{\boldsymbol{x}} = -\nabla V_{\mathrm{i}}(\boldsymbol{x}) - \boldsymbol{E} - \dot{\boldsymbol{x}} \times \boldsymbol{B}. \tag{4.6}$$

Each electron trajectory was propagated until the end of the pulse and the asymptotic momenta were calculated via Kepler's analytical formula [125, 126].

To circumvent numerical problems with the $1/r$ Coulomb potential we filter out electrons that come closer than 0.5 a.u. to the parent ion. This just affects as few as 0.25% of the trajectories and was verified not to alter the outcome of the simulation. For each laser intensity, 10^6 trajectories were calculated and subsequently binned in momentum space with a bin size of 10^{-3} a.u.. In analogy to the procedure with the experimental data, the maxima of the resulting photoelectron images projected onto the beam propagation direction were identified by Lorentzian fits of the central part of the momentum distributions.

We would like to mention that the central spot in the simulated PMDs is absent since we did not include the field ionization of highly excited states by the spectrometer field. However, in the simulations, the reference for zero momentum is intrinsically known. For the simulations the error was estimated from the bin size used.

4.4 Results

In the experiment, the extracted offset of the peak of the PMDs in beam propagation direction shows a clear trend with respect to intensity: in the studied intensity range we observe an increase of the offset for higher intensities. This behavior is also directly visible in the photoelectron momentum images (Fig. 4.4(a)). Furthermore, we observe that the offset is shifted towards negative values on the beam propagation axis, i.e., opposite to the beam propagation direction. This behavior appears to be counterintuitive as it contradicts the expectation for a free electron, i.e., without any influence of the Coulomb potential: the behavior of a free electron is expected to be governed by the radiation pressure that is exerted onto it by the

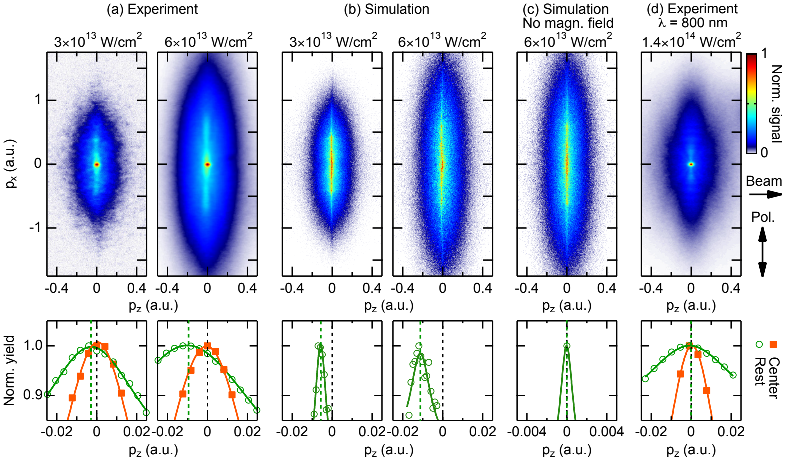

Figure 4.4: PMDs and their projections recorded in xenon and helium at different intensities. Upper figures: measured and simulated PMDs. Lower figures: projections of these PMDs onto the beam propagation, as used to extract the momentum offset (see Fig. 2). (a) Experimentally-measured PMDs of xenon recorded at 3 and 6×10^{13} W/cm^2. (b) Corresponding simulated PMDs at same intensities than (a) reproducing the negative offset through the combined influence of the Coulomb potential and the full electromagnetic laser field. (c) Simulated PMD excluding the magnetic field. The projection exhibits no offset. (d) Measured PMD of helium at 800 nm and an intensity of 1.4×10^{14} W/cm^2. Due to the shorter wavelength, the dipole approximation is valid and no offset is visible. Adapted from [95].

Lorentz force. This picture was also utilized in Ref. [27] for the interpretation of an observed shift of the photoelectron momentum distributions in the beam propagation direction.

In contrast, we show that the behavior in the case of linearly polarized light is caused by the influence of the magnetic field and the Coulomb potential. In this case, the electron can be driven back to the ion core by the laser field and can interact with the ion's Coulomb potential [47, 115]. As a simplified intuitive picture for the observed asymmetric momentum distribution, one might think of electrons first being pushed in the beam propagation direction by the magnetic field, and then being scattered in the opposite direction by the Coulomb potential when the electrons subsequently pass by the parent ion (Fig. 4.5).

To explain our observations, the experimental data are compared to the CTMC calculations including both the magnetic field component of

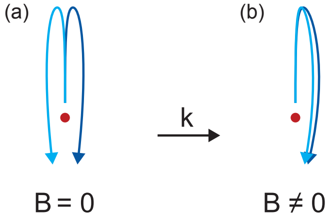

Figure 4.5: Sketch of two electron trajectories under the influence of the combined Coulomb and laser field to illustrate the momentum shift opposite to the beam propagation direction k. a) Without magnetic field, the electron momentum distribution is symmetric with respect the propagation axis as a results of the symmetric distribution of initial momenta and symmetric forces acting onto the electron wave packet. b) The Lorentz force due to the magnetic field component results in a shift of the electrons in beam propagation direction. This shift in combination with consecutive passes close to the ion lead to a backscattering resulting in a shift of the peak of the momentum distribution opposite to the beam propagation direction.

the laser pulse and the Coulomb potential of the residual ion. We observe a good agreement between the simulated PMDs and the experimental data Fig. 4.4(b). When the magnetic field component is neglected in the calculations, the asymmetry along the beam propagation direction vanishes (Fig. 4.4(c)). In order to rule out the possibility that our observed momentum shifts were introduced as an experimental artifact, PMDs were recorded in the same geometry at a wavelength of 800 nm and are shown in Fig. 4.4(d). The intensity used in this photoelectron image was 1.4×10^{14} W/cm^2, i.e., an intensity that is significantly higher then the ones used for our experiments at mid-IR wavelengths. Nonetheless, this photoelectron image does not show any measurable asymmetry.

In Fig. 4.6 the offsets extracted from the experiments with different gases are plotted together with the ones from the simulations. We observe an excellent agreement of the offsets between experiment and our simple semiclassical theory. For our parameter range, we see an increase of the momentum offset with increasing intensity. Our data demonstrate that the offset is not sensitive to the target gas within the sensitivity limits of the experiment.

A further aspect of strong-field ionization beyond the dipole approximation that has been discussed in recent articles is a possible momentum transfer of the order I_p/c onto either the ionized electron, the ion or the electron-ion system. In the work of Smeenk et al. [27], the authors

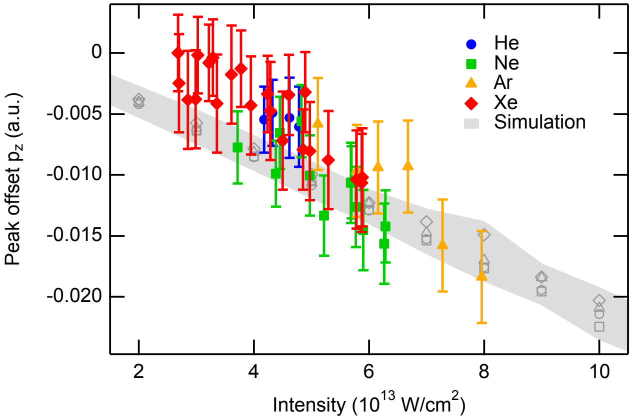

Figure 4.6: Extracted peak offsets along the laser propagation direction as function of laser intensity for different target gases from experiment (filled markers) and semiclassical simulation (open markers). The points show a clear trend towards increasing negative offsets (i.e. opposite to the beam propagation direction) for increasing laser intensities. The uncertainties are indicated as error bars and the gray shaded area, respectively. Adapted from [95].

concluded that a momentum I_p/c is transferred to the electron-ion system before the electron dynamics is governed mainly by the laser field. Other works suggest an initial kick of the electron in the direction of the beam [122, 123]. From comparison of simulations where we included a momentum kick of the electron in z-direction with the ones without, we find that in the case of linearly polarized light our measurements are not sensitive enough to resolve consequent signatures in the photoelectron spectra.

To finalize the study, we compare our results to those obtained in circular polarization [127]. In contrast to the momentum distributions acquired in linear polarization, those acquired in circular polarization exhibit a symmetry along the beam propagation direction and lack the central peak stemming from Rydberg atoms. The calibration for zero electron momentum was thus taken in linear polarization just before the measurement. The symmetry of the distribution simplifies the analysis as it allows us to fit a Gaussian function to the complete projected distribution (Fig. 4.7) in order to extract the offset. Based on this analysis we find an increasing shift of the distribution in beam propagation direction with increas-

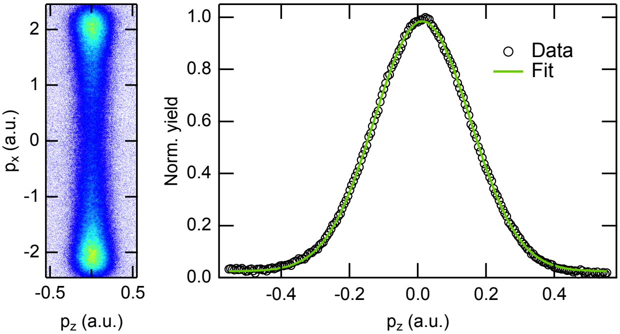

Figure 4.7: Experimental photoelectron momentum distribution for the case of circular polarization. The projected distribution is fitted with a Gaussian function in order to extract the offset in positive beam propagation direction following the analysis in [27]. Adapted from [127].

ing intensity which is in perfect agreement with the prediction based on radiation pressure and a negligible Coulomb potential [27]. The results obtained in linear and circular polarization are shown together in Fig. 4.8.

4.5 Conclusion

In conclusion, we observed the breakdown of the dipole approximation in its long-wavelength limit for moderate laser intensities in the mid-IR. We showed that for our experimental parameters, the electron dynamics is significantly influenced not only by the magnetic field component of the laser field but also by the Coulomb potential of the parent ion. The action of the Coulomb potential yields rather complicated electron dynamics which challenge the previously-used radiation pressure picture. Thus, concepts [105, 106] to compensate for non-dipole effects need to be revisited to take the Coulomb field into account. As the results from our simulations are largely robust against the starting conditions, we conclude that our observations are mainly induced during the quasi-classical dynamics in the continuum which obstructs a direct insight into the nature of the initial ionization step.

Our results pose new challenges for the theoretical description of strong-field processes in the long wavelength limit, which is presently of high interest in this research field. However, our findings also open up new

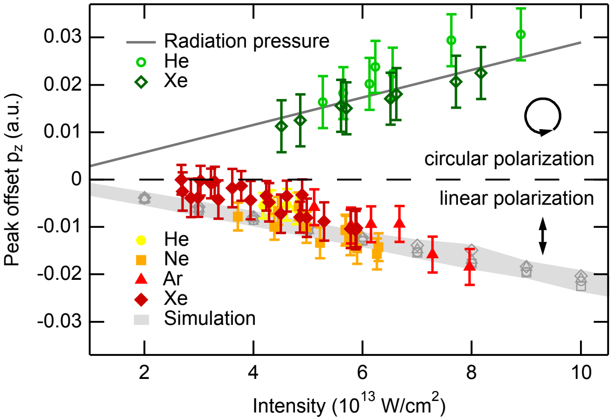

Figure 4.8: Comparison of the results obtained with linear and circular polarization. The results for the case of linear polarization are identical to Fig. 4.6. For the case of circular polarization, the peaks of the projected momentum distributions are shifted in (positive) beam propagation direction as expected in the simple picture based on a negligible Coulomb potential and the radiation pressure [27]. Adapted from [127].

possibilities for studying the response of the target system to the magnetic field component inherently present in the laser pulse.

Recently, Chelkowski et al. could fully confirm the observed negative offset of the peak of the momentum distribution with ab initio calculations of the time-dependent Schrödinger equation in the velocity gauge [128].

Chapter 5

Ptychographic Reconstruction of Attosecond Pulses

In this chapter, we will introduce and characterize a new procedure for the reconstruction of attosecond pulses based on attosecond streaking spectrograms (Sec. 2.5.2). It imposes substantially lower requirements on the sampling of the spectrogram and is able to correctly retrieve the complex pulse and the gate even for extreme cases of coarse sampling and low signal-to-noise ratios. Parts of this chapter have been published in [129].

5.1 Introduction

The ptychographic reconstruction of attosecond pulses is a new modality for attosecond pulse characterization which is derived from a phase retrieval scheme widely used in lensless imaging, namely ptychography. It is related to the solution of the phase problem in crystallography as proposed by Hoppe [130] and was first demonstrated experimentally at visible wavelengths [131]. In ptychography a real space object, in particular its amplitude and phase, is reconstructed iteratively from a series of far-field diffraction measurements. Each of those is recorded after either moving the object or the coherent illumination beam in a plane perpendicular to the propagation direction of the illumination beam. The transverse shift of the illumination beam is smaller than its spatial support, so that subsequent far-field diffraction patterns result from different but overlapping regions of the object. The spatial resolution is limited by the positioning accuracy, the stability of the entire setup and the angular range of scattered wave vectors that can be recorded with a sufficiently high signal-to-noise ratio. Ptychography has been proven to produce the correct real space image if the illumination beam is known [132] but works even if the illumination beam is unknown in which case its profile is reconstructed together with the object [133, 134]. Applying ptychography to the reconstruction of temporal rather than spatial objects requires operating in one dimension with the conjugated variables time and frequency [135]. The unknown temporal object is to be reconstructed iteratively from a series of far-field diffraction measurements, i.e., spectra. Each of those is recorded after delaying the coherent illumination pulse with respect to the temporal object with the time delay being smaller than the temporal support of the illumination pulse. The temporal resolution is primarily limited by the range of spectral amplitudes which can be recorded with a sufficiently high signal-to-noise ratio (SNR).

Recently, it was shown that ptychography can indeed be applied to reconstruct temporal objects if the illumination pulse is fully characterized [136]. It could subsequently be shown that ptychography is a very powerful technique for ultrafast pulse characterization [137]. Here, we show that the concept can be extended to attosecond pulse characterization or photoelectron streaking experiments in general.

5.2 Methodology

The ptychographic reconstruction, as well as PCGPA and LSGPA, is based on the equation for the streaking spectrogram $S(\omega, \tau)$ introduced in Equation 2.20. As this equation represents the spectrum of the product field $P(t)G(t-\tau)$, it should be possible to use the extended ptychographic iterative engine (ePIE) to reconstruct $P(t)$ if $G(t)$ is known [132] or the ePIE to reconstruct both the XUV pulse as well as the streaking field [133, 134].

Ptychography operates on two sampling grids which are largely independent from each other. The XUV pulse and the streaking field are sampled on an equidistant temporal grid, with M samples equally spaced by δt, which is solely determined by the resolution and total spectral range of the spectrometer used – or by the spectral range which can be detected with a sufficient SNR. The second grid is that of the time delays and consists of N samples equally spaced by $\delta\tau$. Both grids may but do not necessarily have to span the same time window. If they span the same time window the frequency increment of both grids $\delta\omega$ is identical and we find $\delta\omega\delta t = 2\pi/M$ and $\delta\omega\delta\tau = 2\pi/N$, respectively. The only constraint on the two integers M and N is $N \leq M$, but typically N is orders of magnitudes smaller than M. Ptychography requires N spectra $I_n(\omega)$ which are recorded at different time delays τ_n ($n = 1 \dots N$) between the XUV pulse and the streaking field. All spectra combined result in a spectrogram $S(\omega, \tau)$ sampled on an $M \times N$ grid. As a starting point for the reconstruction algorithm we assume white noise for the XUV pulse, i.e., $P_{j=1,n=1}(t)$, and a reasonable gate function $G_{j=1,n=1}(t)$ obtained from the streaking trace itself using the center of mass method [138]. In every iteration j all measured spectra are processed. For ascending N the algorithm first updates the current estimate of the XUV pulse and hereafter the estimate of the gate function. It calculates the exit field $\xi_{j,n}(t, \tau_n)$ for a particular time delay τ_n between the gate function $G_{j,n}(t)$ and the XUV pulse $P_{j,n}(t)$

$$\xi_{j,n}(t, \tau_n) = P_{j,n}(t) G_{j,n}(t - \tau_n) \tag{5.1}$$

From $\xi_{j,n}(t, \tau_n)$ we calculate the Fourier transform $\xi_{j,n}(\omega, \tau_n)$ and replace its modulus by the square root of the corresponding experimental/simulated spectrum $I_n(\omega)$ while preserving its phase. After an inverse Fourier transformation the new function $\xi'_{j,n}(t, \tau_n)$ differs from the initial estimate and the difference is used to update the current estimate of the XUV pulse

$$P_{j,n+1}(t) = P_{j,n}(t) + \beta_{\mathrm{P}} U_{j,n}(t - \tau_n) \left[\xi'_{j,n}(t, \tau_n) - \xi_{j,n}(t, \tau_n)\right] \tag{5.2}$$

with the weight or window function based on the complex conjugate $G^*_{j,n}(t)$

$$U_{j,n}(t) = \frac{G^*_{j,n}(t)}{\max\left[|G_{j,n}(t)|^2\right]} \tag{5.3}$$

and the weighting constant $\beta_{\mathrm{P}} \in]0, 1]$.

Similarly, the algorithm updates the gate function starting from

$$\xi_{j,n}(t, \tau_n) = P_{j,n}(t + \tau_n) G_{j,n}(t) \tag{5.4}$$

As before, $\xi_{j,n}(t,\tau_n)$ is Fourier transformed, the modulus is replaced by the square root of the corresponding spectrum $I_n(\omega)$ and the new function $\xi'_{j,n}(t,\tau_n)$, obtained after an inverse Fourier transformation, is used to update the current estimate of the gate function

$$G_{j,n+1}(t) = G_{j,n}(t) + \beta_{\mathrm{G}} V_{j,n}(t+\tau_n) \left[\xi'_{j,n}(t,\tau_n) - \xi_{j,n}(t,\tau_n)\right] \tag{5.5}$$

with the weight or window function based on the complex conjugate $P^*_{j,n}(t)$

$$V_{j,n}(t) = \frac{P^*_{j,n}(t)}{\max\left[|P_{j,n}(t)|^2\right]} \tag{5.6}$$

and the weighting constant $\beta_{\mathrm{G}} \in]0,1]$. Since the gate function has to be a pure phase gate we can impose an additional constraint, i.e.,

$$G_{j,n+1}(t) = \exp(\mathrm{i}\arg[G_{j,n+1}(t)]). \tag{5.7}$$

In a typical attosecond streaking experiment the absolute value of the pump-probe time delay is not a priori known, but for ePIE the actual value of the time delay axis is meaningful and its zero cannot be arbitrarily defined. This, however, does not constitute a limitation. A shift of time delay zero will result in a shift of the time axis of both reconstructed fields, i.e., $P(t)$ and $G(t)$. Therefore, as long as the absolute value of the time delay at which the streaking trace is centered does not fall outside the total time window, the algorithm converges to the correct but temporally shifted solution.

The ptychographic scheme differs from the other attosecond reconstruction modalities introduced in Sec. 2.5.2, such as the principal component generalized projections algorithm (PCGPA) [77] or the least-squares generalized projections algorithm (LSGPA) [72, 139], specifically:

i The time delay increment is not related to the desired temporal resolution or the wavelength sampling of the spectrometer, but only to the duration of streaking field $G(t)$. The time delays do not even have to be equidistant

ii Typically, only a few spectra have to be recorded iii The small number of spectra to process and the robust algorithm result in an extremely fast convergence of the retrieval algorithm

As discussed in Sec. 2.5.2, the PCGPA algorithm relies on a spectrogram sampled on an $M \times M$ grid that satisfies $\delta\omega\delta\tau = 2\pi/M$. Typically the spectral axis has a higher sampling rate than the delay axis, and as a consequence the delay axis needs to be interpolated. Naturally, interpolation will neglect any temporal structure finer than the original sampling, thus PCGPA cannot accurately reconstruct temporal features which vary more rapidly than the time delay increment. With the LSGPA algorithm this problem is somewhat relaxed to $\delta\omega\delta\tau = 2\pi L/M$, with $L \geq 1$ being an integer, as long as two constraints are considered. Firstly, the spectrogram has to be recorded at equidistant time delays (this constraint might be overcome by using a variable L [72]), and secondly, the time delay has to be smaller than the temporal support of the XUV pulse.

In contrast to both, the ptychographic scheme has no direct link between temporal sampling and time delay as explained above. The time delay increment $\delta\tau$ is related only to the duration of the slowly varying envelope of the streaking field $G(t)$. The relevant quantity in ptychography is the fundamental sampling ratio. It is defined as the ratio of the full width at half maximum (FWHM) duration of the streaking field over the time delay increment, i.e.,

$$R = \mathrm{FWHM}[G(t)]/\delta\tau, \tag{5.8}$$

and if both are identical the fundamental sampling ratio is equal to one. For a fundamental sampling ratio $R > 1$ the streaking field overlaps with parts of the XUV pulse several times and this overlap increases the redundancy in the data recorded. It is well known that this redundancy can be used to not only reconstruct the XUV pulse but also the streaking field [133, 134]. Therefore, we expect attosecond ptychography to work for $R > 1$ and indeed we find that $R > 5$ gives accurate reconstruction results for both the XUV pulse and the streaking field.

Somewhat more challenging is to identify suitable values for β_{P} and β_{G} since no theoretical framework exists which can hint to their optimal values. Through dedicated simulations we can estimate that β_{P} scales approximately inverse with R. For example, a streaking field duration of

5 fs and a time delay increment of 0.2 fs result in $R = 25$ and consequently β_{P} should be approximately 0.2. In order to estimate β_{G} we resorted to numerical simulations through which we found that $\beta_{\mathrm{G}} \leq 0.1$ gives excellent results. A small β_{G} value, i.e., a small update rate of the streaking field, does make sense given the fact that the shape of the streaking field is already relatively well defined through the center of mass method [138] introduced in Eq. 2.25.

5.3 Simulation

We first demonstrate that the ePIE algorithm produces accurate reconstruction results for different XUV pulses. We then proceed to identify the optimal reconstruction parameters, i.e., the time delays τ_n, the number of spectra N, as well as β_{P} and β_{G}. Next we show that only very few spectra are required to obtain accurate reconstruction results and finally we compare the algorithm to PCGPA and LSGPA and analyze its sensitivity with respect to noise.

In all examples presented hereafter the streaking field is an IR pulse centered at 800 nm. Its spectrum is Gaussian with a FWHM of 180 nm corresponding to a FWHM pulse duration of approximately 5 fs. The pulses are focused to intensities between $10^{11}\,\mathrm{W/cm^2}$ and $10^{13}\,\mathrm{W/cm^2}$ which is sufficiently low to invoke the central momentum approximation. The XUV pulses and the streaking field are sampled on a temporal grid extending ±50 fs around time zero with a resolution of $\delta t = 24$ as and $M = 4096$. The corresponding energy grid is centered around 86.25 eV with a resolution of 0.042 eV. The transform limited XUV pulse has a FWHM duration of 240 as and we analyze individual pulses with and without phase modulation as well as trains of pulses consisting of two or nine such pulses with different amplitudes and a separation given by one half of the IR driver laser's oscillation period. As a measure for the quality of the reconstruction we use the root mean square E_{rms} between the original and the reconstructed spectrogram after a finite number of iterations:

$$E_{\mathrm{rms}} = \min_{\alpha} \sqrt{\frac{1}{MN} \sum_{\omega,\tau} \left| S_j(\omega,\tau) - \alpha S_{\mathrm{exp}}(\omega,\tau) \right|^2}, \tag{5.9}$$

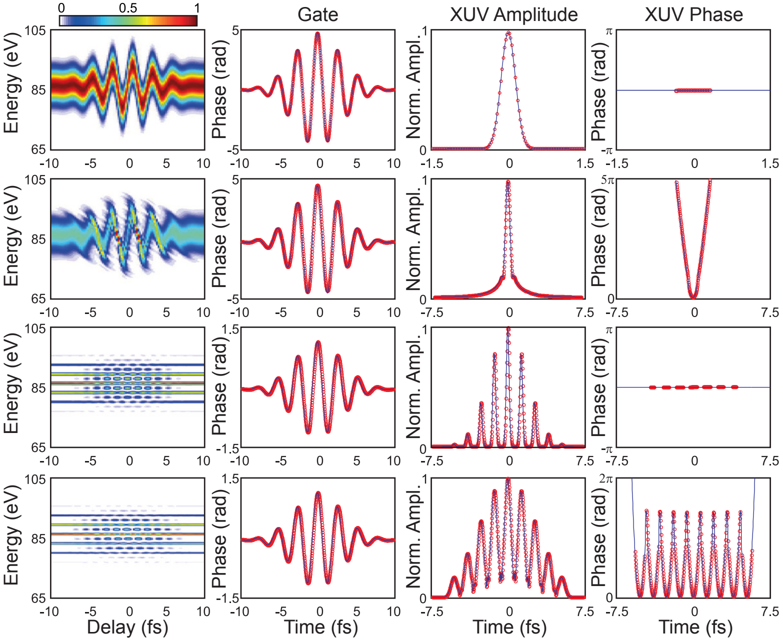

Figure 5.1: Spectrogram, streaking field, XUV amplitude and phase versus time. Theoretical (blue curves) and ePIE reconstructed (red open circles) results. First row: Isolated bandwidth-limited attosecond pulse of 240 as duration. Second row: Same attosecond pulse with a quartic phase of $2{\times}10^{-4}\,\mathrm{fs}^4$. Third row: Pulse train consisting of nine unchirped pulses each 240 as long. Fourth row: Same pulse train with a quadratic phase of $2\times10^{-2}\,\mathrm{fs}^2$. Adapted from [129].

with the spectrogram $S_j(\omega,\tau)$ after j iterations calculated from the actual estimate of the XUV pulse and streaking field, and α being a normalization constant that minimizes the difference in intensities between the simulated/measured and the reconstructed spectrograms [73].

Figure 5.1 shows the reconstruction results assuming four different XUV pulses. The first row compares simulations (solid blue curve) and reconstruction (red open circles) results for an isolated bandwidth-limited attosecond pulse of 240 as duration. The agreement obtained after 1000 iterations of the ePIE algorithm is excellent. The reconstructed streaking field as well as the reconstructed XUV pulse are practically indistinguishable from the fields used to calculate the spectrogram.

The second example (Fig. 5.1 second row) is the same attosecond pulse

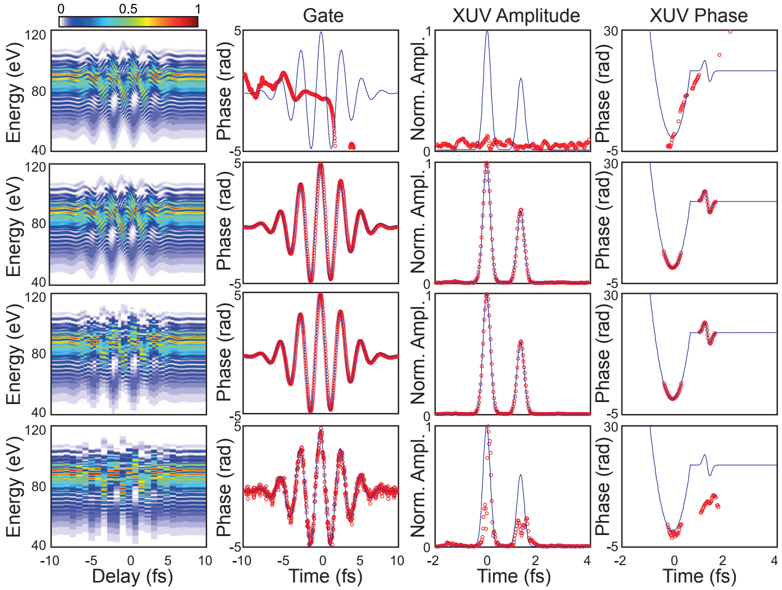

Figure 5.2: Reconstruction of pulse with satellite with fixed parameters and different numbers of time delays. Spectrogram, streaking field, XUV amplitude and XUV phase. Theoretical (blue curves) and reconstructed (red open circles) results for a double pulse. First row: $N = 401$, $\delta\tau = 50\,\mathrm{as}$. Second row: $N = 201$, $\delta\tau = 100\,\mathrm{as}$. Third row: $N = 51$, $\delta\tau = 400\,\mathrm{as}$. Fourth row: $N = 25$, $\delta\tau = 800\,\mathrm{as}$. Adapted from [129].

with a quartic phase of $2 \times 10^{-4}\,\mathrm{fs}^4$. The third and the fourth examples are trains of attosecond pulses without and with a quadratic phase of $2 \times 10^{-2}\,\mathrm{fs}^2$. This shows that the ePIE algorithm is able to reconstruct both single attosecond pulses and attosecond pulse trains, independently of their spectral phase. Henceforth we concentrate on a double pulse with identical pulse duration and an intensity ratio of 1:0.6, similar to the one used in [72], in order to show that ePIE can correctly discern between single attosecond pulses and those with a satellite. The phase modulations of the main pulse and the satellite are $40t^2$ and $-50(t - T_\mathrm{p}/2)\exp(-2(t - T_\mathrm{p}/2)/0.2)^2)$, with T_p being the oscillation period of the IR driver field and the time t is to be inserted in femtoseconds.

Figure 5.2 shows the spectrogram and the reconstructed XUV pulse and streaking field for different time delay increments. The number of spectra simulated was adjusted such that the total time window remains

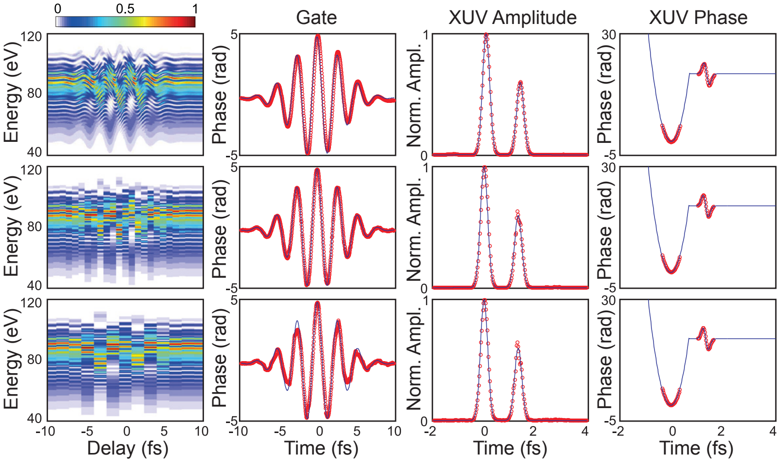

Figure 5.3: Reconstruction of pulse with satellite with adapted parameters for different numbers of time delays. Spectrogram, streaking field, XUV amplitude and XUV phase. Theoretical (blue curves) and reconstructed (red open circles) results for a double pulse. First row: $N = 401$, $\delta\tau = 50\,\mathrm{as}$, $\beta_\mathrm{P} = 0.15$. Second row: $N = 25$, $\delta\tau = 800\,\mathrm{as}$, $\beta_\mathrm{P} = 0.65$. Third row: $N = 13$, $\delta\tau = 1.6\,\mathrm{fs}$, $\beta_\mathrm{P} = 0.85$. Adapted from [129].

constant (20 fs). A too small or too big time increment leads to erroneous reconstruction results. From time domain ptychography it is known that there is a link between the time delay increment $\delta\tau$ and the reconstruction parameter β_P. Generally, the larger the time delay increment the larger β_P has to be chosen in order to obtain convergence and accurate results. Therefore, the unsuccessful reconstructions of the spectrograms shown in Fig. 5.2 were repeated but this time with an optimal β_P value. The resulting XUV pulses and streaking fields are shown in Fig. 5.3. When adjusting β_P accordingly, we find excellent agreement for all time delay increments. Note that for $\delta\tau = 1.6\,\mathrm{fs}$ (Fig. 5.3 third row) only 13 spectra are sufficient for an accurate pulse reconstruction.

In the following we explore the size of the streak window required for a sufficiently accurate reconstruction result. For this purpose, we fix the number of spectra and decrease the time delay step from 800 as to 50 as. Figure 5.4 shows the reconstruction results. For 50 as we cover a total streak window of only 1.25 fs which corresponds to roughly one half of the streaking field period and is comparable to the separation between the two attosecond pulses. Despite the small streak window, which just about extends over the double pulse waveform, the reconstruction of the XUV pulse works surprisingly well. For isolated attosecond pulses an even shorter total streak window may be sufficient. The PCGPA algorithm, requiring periodic boundary conditions, fails to converge if the streaking field is only partially covered by the range of time delays. In LSGPA the problem is somewhat relaxed. In stark contrast, the ePIE algorithm only requires a range of time delays that covers the XUV pulse to be reconstructed but not the entire streaking field. Of course the reconstruction of the streaking field outside the streak window is arbitrary and without relevance.

Next we investigate ePIE's performance in comparison to other algorithms commonly used in attosecond streaking, i.e., PCGPA or LSGPA. Figure 5.5 compares the results of PCGPA and LSGPA to those of ePIE for the case of the double attosecond pulse with a phase modulation of $60t^2$ for the main pulse and $-20(t - T_\mathrm{p}/2)\exp(-2((t - T_\mathrm{p}/2)/0.2)^2)$ for the satellite. The IR streaking field intensity is $5.5 \times 10^{12}\,\mathrm{W/cm^2}$. The simulated spectrogram (Fig. 5.5 top-left panel) is composed of $N = 105$ spectra which are simulated with a time delay increment of $\delta\tau = 200\,\mathrm{as}$. The black curves in the right column of the Fig. 5.5 show the amplitude (top) and phase (center) of the simulated XUV pulse. The lower panel displays the IR streaking field. The reconstruction results presented are after 20000 iterations for all three algorithms. The second spectrogram from the top shows the ePIE reconstruction. The extracted XUV pulse and streaking field are marked with red circles in the respective panels. The third spectrogram from the top shows the PCGPA results and the bottom one the reconstruction of the LSGPA (corresponding to blue open squares and orange open triangles in the right column).

For the case of ePIE the entire generated spectrogram is used in the reconstruction algorithm. In order to keep the computation time reasonable, the spectrogram as been reduced in size to a square matrix composed of 1024×1024 points for PCGPA. In the case of LSGPA only the energy axis has been reduced to 1024 points which results in a delay-energy step ratio of $L = 5$. By comparing the different results, it is possible to conclude that, while all the algorithms correctly reconstruct the main pulse, only the

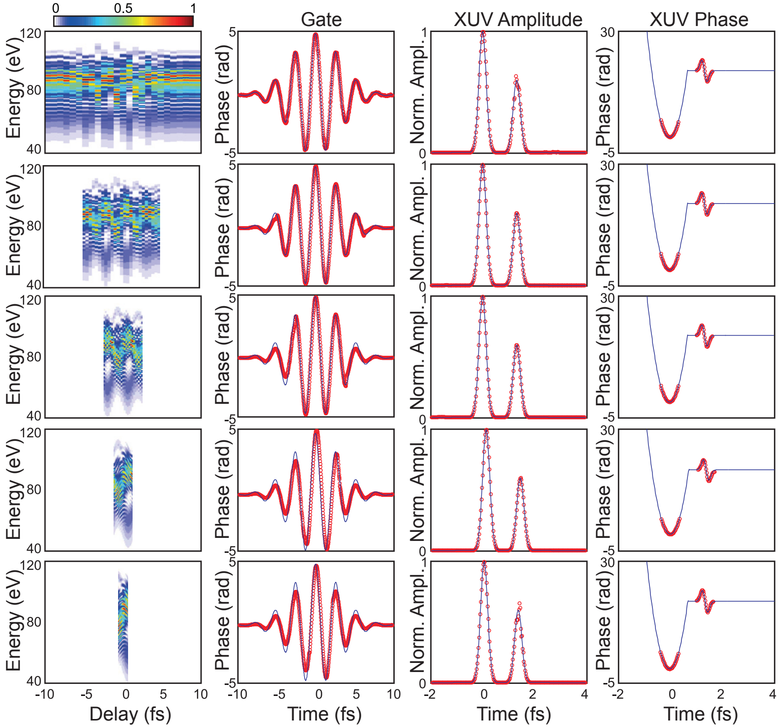

Figure 5.4: Reconstruction of pulse with satellite with adapted parameters for decreasing coverage of the spectrogram. Spectrogram, streaking field, XUV amplitude and XUV phase. Theoretical (blue curves) and reconstructed (red open circles) results for a double pulse. First row: $\delta\tau = 800\,\mathrm{as}$, $\beta_\mathrm{P} = 0.65$. Second row: $\delta\tau = 400\,\mathrm{as}$, $\beta_\mathrm{P} = 0.55$. Third row: $\delta\tau = 200\,\mathrm{as}$, $\beta_\mathrm{P} = 0.45$. Fourth row: $\delta\tau = 100\,\mathrm{as}$, $\beta_\mathrm{P} = 0.35$. Fifth row: $\delta\tau = 50\,\mathrm{as}$, $\beta_\mathrm{P} = 0.25$. Adapted from [129].

ePIE algorithm properly resolves the satellite and the IR field. Moreover, there are a number of marked advantages using ePIE. First, convergence is usually much faster and takes less time as the computational effort is smaller. Second, ePIE produces accurate results even for very few spectra recorded as already discussed above while the two other algorithms fail to converge.

Lastly, we analyze the reconstruction results in the presence of noise. For that purpose, we add white noise to the simulated trace in the top-left panel of Fig. 5.5 prior to the reconstruction. Specifically, we add to each pixel of the spectrogram, which we assume is normalized to a maximum

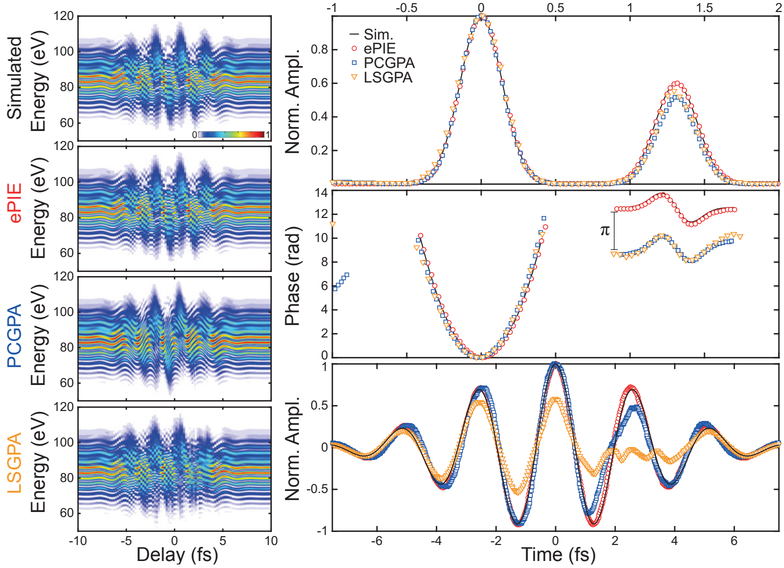

Figure 5.5: Comparison of ePIE with PCGPA and LSGPA for the double attosecond pulse. Left column: Simulated and reconstructed spectrograms; Right column: Retrieved time dependent amplitude and phase of the XUV pulse and the streaking field. First top-left panel and the black solid curves: Simulated data. Reconstructed pulses in red circles, blue squares and orange triangles for ePIE, PCGPA and LSGPA. Each reconstruction is after 20000 iterations, resulting in final errors of 1.4×10^{-4}, 2.5×10^{-2}, and 3.4×10^{-2} for ePIE, PCGPA and LSGPA. Adapted from [129].

of one, rand$[-1,1]$/SNR, with rand$[-1,1]$ being a random number with Gaussian distribution between -1 and 1. Figure 5.6 shows three examples with a SNR of 5, 4 and 3. For a SNR $= 5$ the ePIE algorithm successfully reconstructs both the double pulse and the IR streaking field while the PCGPA results are already very noisy. For a SNR of 4, also the reconstruction of the ePIE starts to become noisy and to underestimate the amplitude of the satellite. Nevertheless, the results are still reasonable since the main characteristics of both XUV and IR are retrieved. With a SNR $= 3$ the ePIE algorithm still converges and gives comparable results. Only for a SNR as low as 2 the convergence is severely compromised. Note that for the example presented in Fig. 5.6 the streaking trace is reconstructed without the need for any further interpolation, while in the case of PCGPA the spectrogram has to be interpolated to a square matrix of 1024×1024

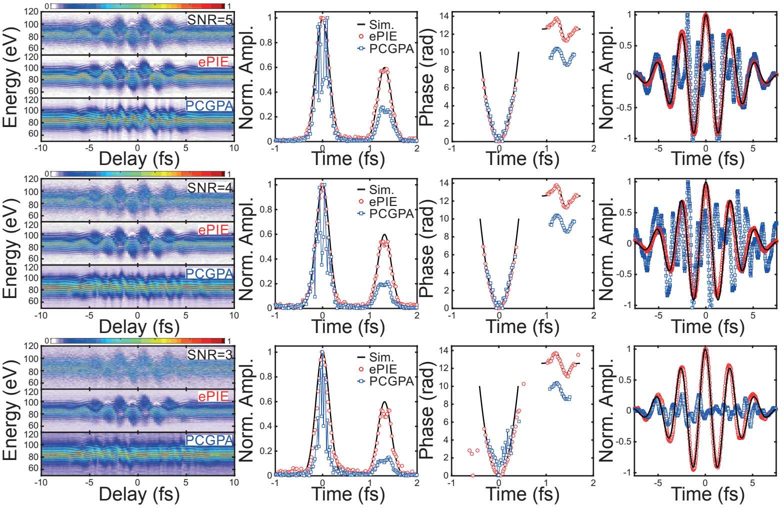

Figure 5.6: Comparison between ePIE and PCGPA reconstructions in the presence of noise. The first two rows show the data for SNR = 5. The third and fourth rows the case of SNR = 4 and the last two the case of SNR = 3. The simulated XUV and IR pulses are in black curves. Blue squares and red circles display the PCGPA and ePIE reconstruction results. Adapted from [129].

points.

5.4 Experiment

We conclude with the ePIE reconstruction of an experimental spectrogram and compare the results with the PCGPA and LSGPA algorithms. The experimental data was acquired at the attoline (Sec. 3.2.2) [90] by ionization of neon with single attosecond XUV pulses which were generated in an argon gas target by means of polarization gating (Sec. 2.4). Consecutive streaking of the resulting electrons was induced by a co-propagating near-infrared field with a peak intensity of $6.6 \times 10^{12}\,\mathrm{W/cm^2}$.

The photoelectron energy was measured with a time-of-flight spectrometer for different time delays between the XUV pulse and the streaking field at increments of 200 as. The resulting spectrogram was used to reconstruct the amplitude and the phase of the XUV pulse as well as the streaking field. The PCGPA algorithm requires an interpolation of the

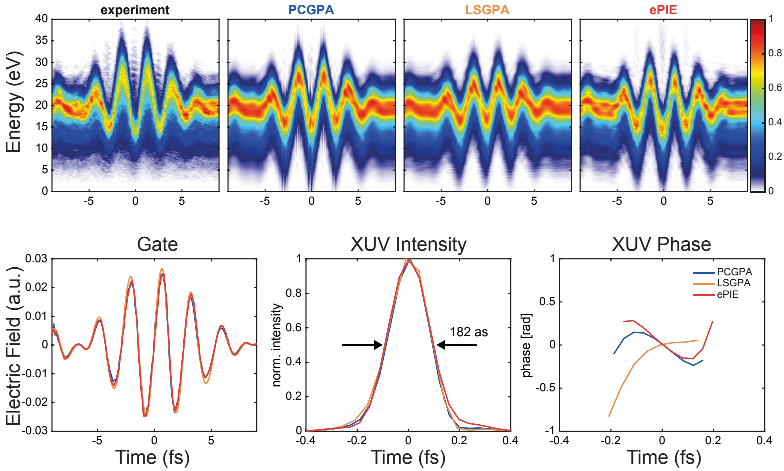

Figure 5.7: Comparison of reconstruction between PCGPA, LSGPA and ePIE applied to an experimental streaking trace. Top row: Reconstructed spectrograms after 20000 iterations for PCGPA, LSGPA and ePIE. Lower panels: retrieved streaking fields and XUV pulse intensities and phases. Adapted from [129].

experimental spectrogram along the time delay axis prior to reconstruction. We therefore interpolate the spectrogram on a square grid of size 512 × 512 fulfilling the Fourier condition $\delta\omega\delta\tau = 2\pi/M$. It is known that this interpolation can lead to artifacts in the reconstruction [140]. The LSGPA ($L = 4$) as well as ePIE do not require an interpolation and operate on a grid of 512 × 100. The results after 20000 iterations are shown in Fig. 5.7. The errors E_{rms} of PCGPA, LSGPA, and ePIE are 3.7×10^{-2}, 5.6×10^{-2}, and 4.6×10^{-2}, respectively.

The reconstructed streaking fields, the XUV intensities with a duration of 182 as and the XUV phases are almost identical. Due to the center of mass approximation applied in all algorithms, the reconstructions cannot account for the asymmetric streaking of the experimental trace. The ePIE reconstruction results are virtually identical to those of PCGPA but require considerably less computational effort due to the lack of constraints on the time delay axis. Thus, we demonstrated that ePIE is suitable for an accurate reconstruction of experimental spectrograms and the characterization of single attosecond pulses.

5.5 Conclusion

In conclusion, we have demonstrated a new modality for attosecond pulse reconstruction based on a retrieval algorithm derived from ptychography which requires to record only a small number of spectra and converges extremely fast and reliably. It reconstructs single attosecond pulses as well as trains of attosecond pulses with an unprecedented degree of accuracy. With a judicious choice of the reconstruction constants it works for a large range of time delay increments and a surprisingly small amount of data.

In contrast to all other algorithms, the range of time delays needs to extend only over the temporal support of the XUV pulse but not the streaking field. Of course this is true only if the exact shape of the streaking field is irrelevant beyond the extent of the XUV pulse. The ePIE generally performs superior to algorithms based on general projections, requires considerable less computational effort and is much less susceptible to noise.

The atto-ePIE algorithm introduced and discussed in this chapter is freely available as MATLAB implementation including some example spectrogram files. It is available for download[1] as part of the original publication [129].

---

[1] Free atto-ePIE download: http://dx.doi.org/10.6084/m9.figshare.1601876

Chapter 6

Anisotropy in Quantum Beat Spectroscopy of Helium Excited States

In this chapter, we present an XUV-pump-IR-probe study of helium excited states performed with the attoline setup. We limit the excitation spectrum to energies just below the ionization potential and thus achieve unperturbed access to the quantum beat signal arising from interference of different ionization pathways. A comparison to the solution of the time-dependent Schrödinger equation unveils an angular dependence of the quantum beat signal caused by the parity of the final states involved. We show that this anisotropy can be exploited to control the emission direction by varying the CEP of the IR probe pulse. Parts of this chapter have been published in [141].

6.1 Introduction

Quantum beat (QB) spectroscopy is a powerful tool employed in femtochemistry [5] to study electronic and vibrational properties of atoms and molecules [142, 143]. Here we used QB spectroscopy in combination with high-order harmonic (HH) excitation [144] in order to study the evolution of an electron wave packet (EWP) composed of high-lying states of helium (He). The harmonic radiation corresponds to attosecond pulses in time domain (Sec. 2.3), which sustain a bandwidth of several electronvolts and are centered in the vacuum ultraviolet (VUV) or extreme ultraviolet

(XUV) [9, 46]. Attosecond QB spectroscopy may therefore be used to study broad excitation bandwidths and tightly bound energy levels that are not reachable with infrared (IR) femtosecond excitation with unprecedented time resolution [145, 146, 147].

So far attosecond wave packet dynamics involving such bound states have only been studied using attosecond transient absorption spectroscopy (ATAS) [148, 149, 14, 150], which recently demonstrated its possibility to investigate QBs in He [151] and neon (Ne) [152]. Here we show that phenomena like non-adiabatic Stark shift [153], population of light-induced states [154] and "direct-indirect" interference of different excitation pathways [155, 54] can, in principle, also be observed in the QB signal. In contrast to ATAS, QB spectroscopy can be used to study the angular content of the EWP.

Furthermore, the energy resolution is, in principle, limited only by the natural linewidth of the excited state levels. In this paper we present the experimental observation of QBs in He obtained by exciting the EWP with a tailored XUV pump, situated below the He ionization potential. This renders the measurement background-free and allows for a complete study of the EWP, including the region of pump-probe overlap where the evolution of the system is strongly influenced by the IR probing field [156, 157].

Moreover, measuring the electron yield as a function of the carrier-envelope phase (CEP) [158] of the driving pulses and comparing with the solution of the time-dependent Schrödinger equation (TDSE), we reveal the existence of QBs with mixed parity, characterized by an asymmetric emission.

6.2 Two-Color Photoemission

Both direct ionization and excitation of bound EWP can be observed when using XUV pulses with a broad spectrum centered on the atomic ionization potential. In a pump-probe experiment, the probe can subsequently ionize the excited part of the EWP and give an electron yield that oscillates with the pump-probe delay. In this case, two main contributions

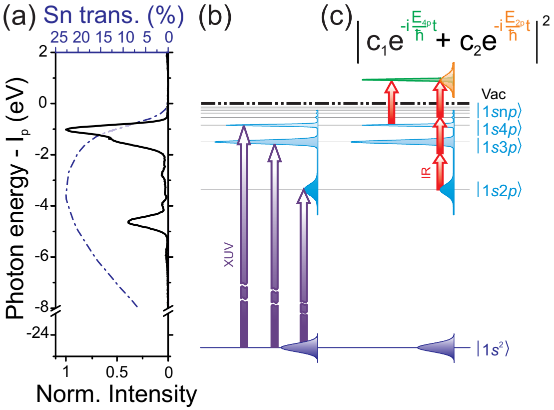

Figure 6.1: Schematic of the quantum beating mechanism. (a) Experimental high-order harmonic spectrum composed of only two harmonics obtained with a 200-nm thick Sn filter. (b) Direct excitation of a coherent superposition of 1s*n*p levels by absorption of XUV photons. (c) Subsequent ionization by IR photons leading, e.g., to the 4p-2p beating signal. Adapted from [141].

to the modulations are expected: (i) quantum beats [159, 160, 161] and (ii) "direct-indirect" interference [162, 28]. QBs arise from the interference of different ionization pathways involving two atomic states (i, j), which give the same final electron energy. If E_i and E_j are the energies of the two excited states then the condition $E_i + n\omega = E_j + n'\omega'$ has to be satisfied. Here n and n' are two integer numbers describing the number of absorbed photons of energy ω and ω', respectively (with ω and ω' within the spectral bandwidth of the IR pulse).

A schematic of the process is presented in Fig. 6.1. The XUV pulse first populates the excited states of He (Fig. 6.1(b)), which are subsequently ionized by the IR pulse (Fig. 6.1(c)). The photoionization probability as a function of delay is thus modulated with a frequency $\omega_{ji} = E_j - E_i$ proportional to the relative energy separation of the states involved and does not depend on the final electron energy.

Conversely, mechanism (i) happens when direct XUV ionization interferes with indirect two-color ionization. The phase accumulated by the directly ionized electron depends on the final velocity. This leads to the appearance of interference fringes following hyperbolic curves [163] in the time domain or, equivalently, lines at 45° in the Fourier transform of the spectrogram.

The role of mechanisms (i) and (ii) in the photoemission from He atoms was first investigated by Mauritsson et al. in Ref. [28]. The authors employed single attosecond pulses in combination with short IR pulses in a pump-probe scheme and angular detection of the photoelectron. By performing an expansion of the full angularly resolved photoelectron distribution as a sum of Legendre polynomials they could disentangle the beating signal coming from ionization processes that end in a state of defined or mixed parity (i.e., appearing in the even or odd coefficients of the expansion). In their particular experimental configuration, the authors claim that "direct-indirect" interference is expected to involve electrons that have absorbed a different number of photons. Since an odd total number of IR photons is thus absorbed by the two interfering pathways, the signature of their interference will appear in the odd coefficients of the expansion. On the other hand, QBs were predicted to dominate in the even coefficients. As a result, this symmetry property could in principle be applied to isolate the QBs even if direct ionization of the target takes place.

Here we show that this is not generally the case. In the presence of probe pulses characterized by a broad bandwidth, both mechanisms (i) and (ii) can indeed give final states with even or odd parity. For example, the "direct-indirect" interference between electrons directly ionized by the 17^{th} harmonic and those which have absorbed one photon from HH15 plus two IR photons, will be characterized by a final state with even parity and thus appear in the even coefficients of the expansion. Concerning mechanism (i), our results obtained without direct ionization show that QBs can as well arise from final states with mixed (odd) parity which will appear in the odd coefficients of the expansion. Furthermore, we show that the parity of the final state is strongly influenced by the probe field in the region of temporal overlap. It follows that the above-mentioned procedure cannot be applied to disentangle the contribution of mechanisms (i) and (ii) in this case.

After the first results obtained with single attosecond pulses, theoret-

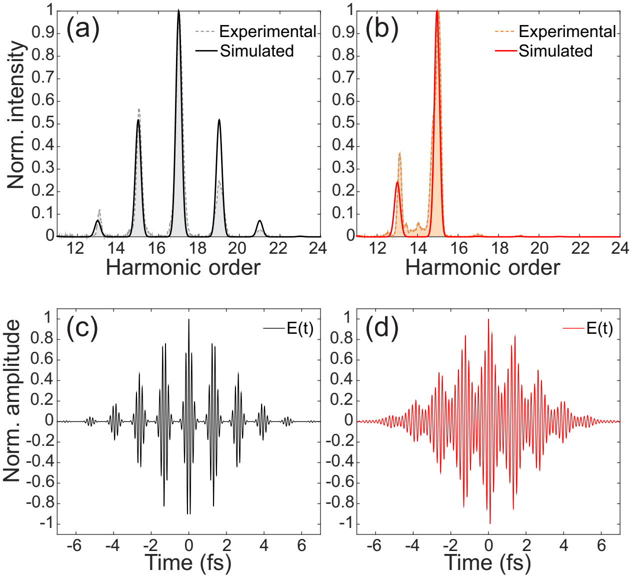

Figure 6.2: (a) Spectrum of the XUV radiation without the Sn filter. Solid line represents the simulated APT, dashed line and shaded area the experimental one. The simulated train has a Gaussian envelope with 5 fs FWHM. The pulses are characterized by a time duration of 400 as. (b), same as in (a), but after filtering with the Sn foil. (c), (d) temporal behavior of the respective simulated spectra shown in (a) and (b). As expected the filtering procedure reduces the contrast of the individual attosecond pulses in the train, but preserves a sub-cycle intensity pulsation. Adapted from [141].

ical and experimental investigations have shown that the same kind of information can be obtained with APTs [144, 164, 165]. Nevertheless, also in these works, direct ionization by the XUV radiation prevented a direct study of the evolution of the EWP for every value of pump-probe delay. In the next section we will show how it is possible to tailor the pump spectrum in order to minimize the effect of mechanism (ii) and overcome this limitation.

6.3 Methodology

In order to obtain a background-free measurement of QBs, we generated a comb of high-order harmonics in Xe with 15-fs IR pulses at a central wavelength of 789 nm. Details of the setup can be found in Sec. 3.2.2 and

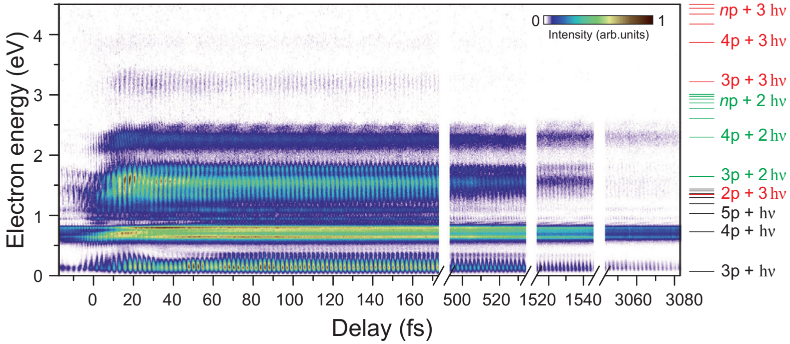

Figure 6.3: Experimental photoelectron spectra as a function of the delay between the IR femtosecond pulse and the XUV APT (positive delays correspond to XUV arriving first). Oscillations of the emission lines clearly appear in the region of pump-probe overlap and extend to positive delays. These spectral features can be attributed to two-color ionization involving one XUV photon and one to three IR photons, as underlined by the theoretical transition lines on the right. The delay axis has been calibrated by looking at the maximum electron yield in two-color ionization using the full harmonic spectrum. Adapted from [141].

in Ref. [90]. The generated HHs were subsequently filtered with a 200-nm thick tin (Sn) foil to select only HH13 and HH15, which lie below the ionization potential of He at 24.59 eV (see Fig. 6.1(a)). This procedure reduces the contrast of the APT and transforms it into a few-femtosecond XUV pulse modulated at twice the fundamental IR frequency but still allows for sub-cycle resolution. Figure 6.2 shows the effect of the Sn filter on a numerically generated APT that resembles the experimental one. The XUV radiation was then recombined with a delayed portion of the IR pulse. Both beams were focused on a He target placed in front of the time-of-flight (TOF) spectrometer in the first experimental region which collected the electrons emitted towards the detector in a cone with an opening angle of 30°. The IR intensity at the focus was varied between $0.9 - 1.5 \times 10^{12}$ W/cm^2. The CEP of the IR pulses was actively stabilized.

Figure 6.3 shows the recorded photoelectron spectra as a function of the delay between the XUV and IR pulses. Each spectrum has been acquired averaging over 20'000 laser shots. A background signal with no pump was acquired every 20 delay steps. When the IR pulse arrives after XUV excitation (positive delays), peaks at the energy position of *n*p states plus an integer number of IR photons appear. These lines correspond to a sequential two-color transition where the XUV photons first populate excited states of He and subsequently the IR ionizes them (see the horizontal lines on the right hand side of Fig. 6.3).

The main features appearing at 0.07, 0.73, 1.64, 2.30, 3.21 and 3.87 eV correspond to ionization of 3p and 4p states via one, two or three IR photons, respectively. A signature of the 5p ionization appears at 1.03 eV. As it is possible to see already in the raw data, the signal associated with these peaks oscillates periodically with the pump-probe delay.

6.4 Time-Frequency Analysis and Theory

A deeper understating of the atomic states forming the EWP can be obtained looking at the spectral content of the QBs. Figures 6.4(a) and (b) show the Fourier transform of the experimental data in Fig. 6.3 along the delay axis for the full delay range and for delays bigger than 70 fs, respectively. QBs of the 3p to 7p states with the 2p state are visible as vertical lines in both cases and are marked with blue arrows in Fig. 6.4(b). The total Fourier transform in Fig. 6.4(a) shows some additional features: firstly, weak tilted lines, marked with red arrows, due to the “direct-indirect” interference involving residual HH17 that is not completely suppressed by the Sn foil and, secondly, stronger broad features around $\omega_0 \sim 1.55$ eV predominantly positioned at the peak of the 3p state. Both features may be observed only when pump and probe overlap in time (small delays around zero) and contain information about the behavior of the IR-dressed states, as we will discuss later on.

The time-frequency (Gabor) analysis of some selected emission lines is presented in Fig. 6.4(c). It shows that the QB frequencies match the unperturbed theoretical values only for long delays. For short delays, the IR field perturbs the system, polarizes the EWP and modifies its spectral content. The strongest effect is observed in case of the 3p-2p QB which moves from a broad feature around $\omega_0 \simeq 1.55$ eV for short delays to its unperturbed value at 1.87 eV for long delays. A relatively strong shift may be seen also in case of the 6p-2p QB with the unperturbed value of 2.99 eV, which is close to $2\omega_0$.

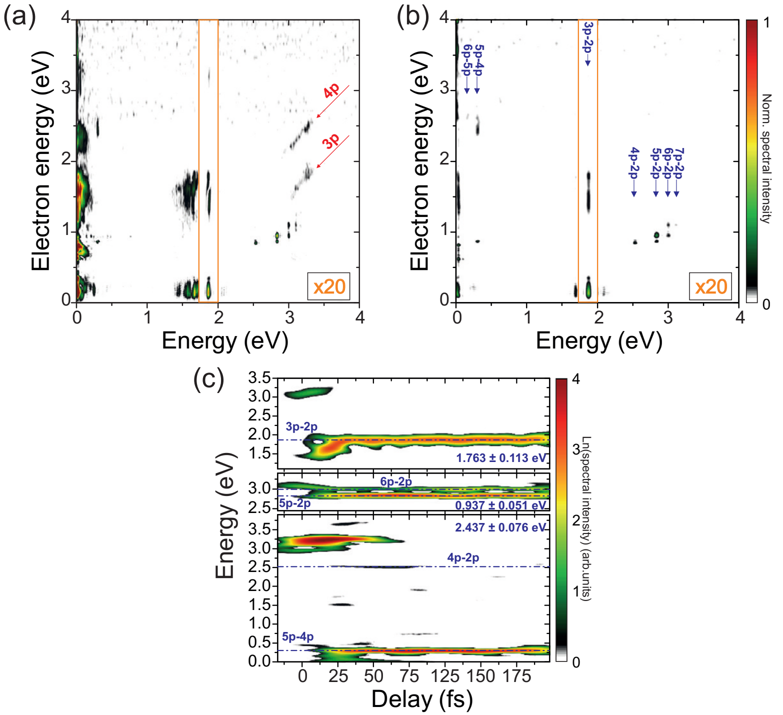

Figure 6.4: Fourier transform of the spectrogram presented in Fig. 6.3 along the delay axis, which allows for the identification of the states forming the EWP. (a) Total signal, (b) signal only for delays bigger than 70 fs excluding the pulse overlap region. In both cases the spectral intensity has been multiplied by a factor of 20 outside the orange box centered around the 3p-2p QB line to better visualize the different spectral components. The QB signals involving states from 2p to 7p appear as vertical lines in both pictures. Blue arrows mark the QB energies based on the unperturbed theoretical atomic levels. In (a), the features around 3.2 eV with 45° tilt represent a signature of the "direct-indirect" interference. These spectral features, as well as the peaks at $\omega_0 \sim 1.55\,\text{eV}$ disappear for large delays, (b). (c) A Gabor analysis of selected QBs shows how the spectral components of the EWP evolve with the delay between the pump and probe. Central energy and integration range are indicated in the three subpanels. The horizontal dot-dashed blue lines mark the theoretical position of the QBs based on an unperturbed He atom. Adapted from [141].

It is important to point out that in order to observe QBs with a periodicity that is non-commensurate with the frequency of the IR probe field, the starting APT (its envelope) has to be short enough. This ensures on one side enough bandwidth to efficiently populate the atomic state. On the other side, it minimizes the reduction in modulation contrast following

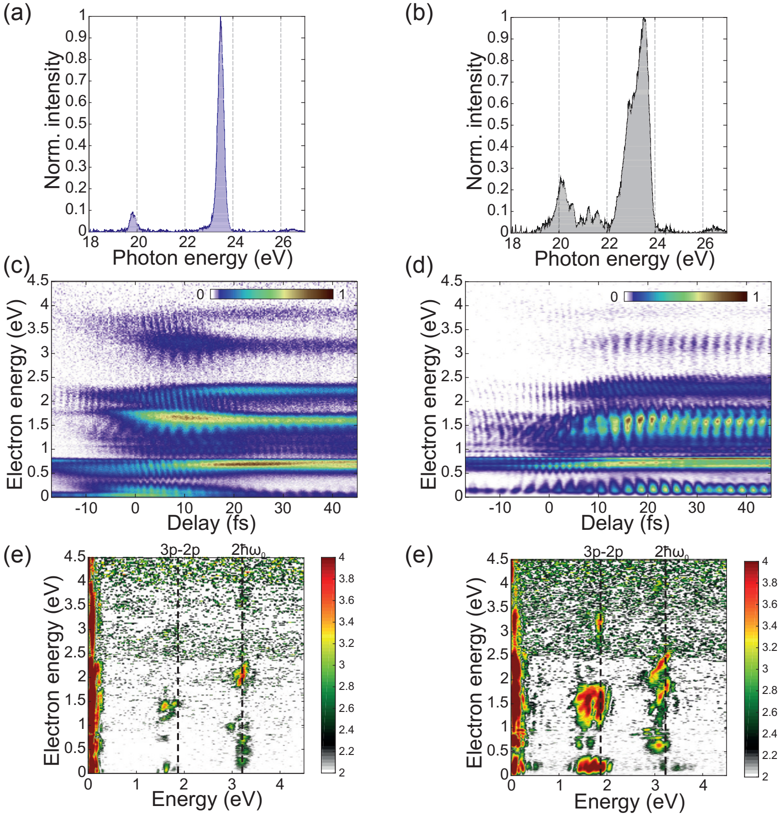

Figure 6.5: Comparison between long and short XUV excitation pulses. (a), (b), Spectra of the pump XUV pulse obtained by selecting HHs 15 and 13 from an APT generated with 25-fs and 15-fs IR pulses, respectively. (c), (e) photoelectron spectra as a function of pump-probe delay and their Fourier analysis for the XUV pump in (a) in logarithmic color scale. (d), (f), same for the excitation pulse displayed in (b). Adapted from [141].

the excitation of QBs by different pulses in the XUV pulse train.

Figure 6.5 depicts a comparison of photoelectron spectra obtained with two different APTs, subsequently filtered to select only HHs 15 and 13. As it is possible to observe, the use of 25-fs driving pulses instead of 15-fs (first row vs. second row in Fig. 6.5), already strongly reduces the amplitude of the QB signals. The more the beating frequency differs from $2\omega_0$, the more the QB signal is suppressed with longer excitation pulses.

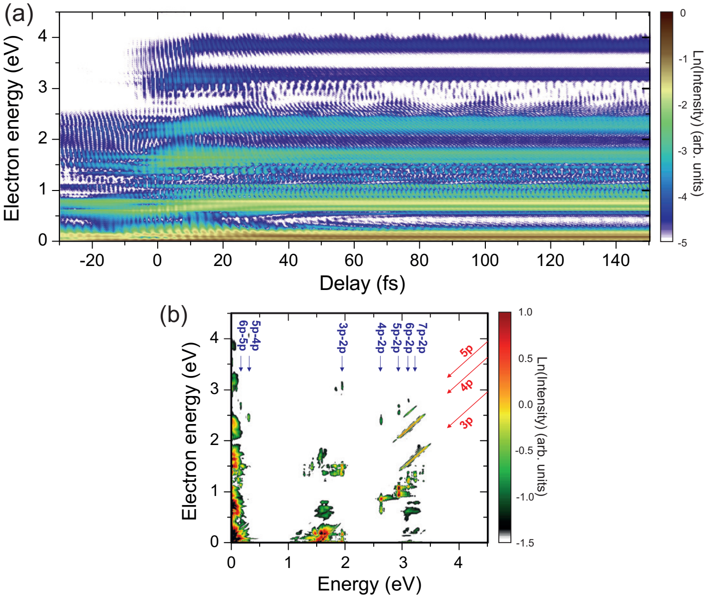

Figure 6.6: Results of the TDSE calculations. Calculated spectrogram and its Fourier transform are displayed in (a) and (b), respectively. To better compare the calculated data with the experimental results, a logarithmic color-map has been adopted in both. This partially compensates for the reduced collection efficiency of slow electrons in the experiment. All the experimental features are well reproduced by the calculations. Adapted from [141].

This can be seen in the 3p-2p QB marked by the vertical black dashed line in Figs. 6.5(e) and 6.5(f). The stronger reduction of these beats can be easily understood in terms of subsequent excitation by different pulses of the XUV radiation. During the interaction, each of the attosecond pump pulses separated in time by $T_0/2 = \pi/\omega_0$ starts a QB, which oscillates with its characteristic frequency. If this frequency is closer to ω_0, QB contributions from subsequent excitations will be out of phase, thus giving a constant total electron yield.

On the other hand, QBs which oscillate with a frequency close to twice the IR-probe frequency, will be in phase and sum up constructively. Therefore, the fingerprint of the latter QBs can still be detected also with relatively long excitation XUV pulses (see Fig. 6.5(e)). We want to stress that the longer the IR probe pulses, the narrower their bandwidth and the less likely the requirement for a common final electron energy will be met. Long IR pulses may therefore reduce the strength of the QB signals independently from the pumping mechanism.

In order to confirm and interpret our observations we solved the time-dependent Schrödinger equation (TDSE). The simulations were performed using the single-electron model of He with the pseudo-potential $V(r) = -(1 + \exp[-\alpha r])/r$, where $\alpha = 2.1325$. The solution was obtained in the velocity gauge using the adaptive-step fourth-order Runge-Kutta method with a high (12^{th}) order finite elements radial basis of size 192 and spherical harmonics with the degree l up to eight. Photoelectron spectra were calculated by the time-dependent surface flux (tSURFF) method [166, 167] integrating the wave function flux at the boundary of the simulation region with the diameter $R = 100\,\text{a.u.}$. The shapes of both pulses were taken directly from experimental measurements. The spectrum of the filtered pump consisting of only two harmonics was assumed to be equal to the experimental one in Fig. 6.2(b).

The phase relation between the two harmonics was retrieved performing a RABBITT [168] measurement (Sec. 2.5.1) with the full spectrum in Fig. 2(a) in Ar and subsequently applying the transmission of the Sn filter numerically [93]. The intensity of the filtered XUV pulse was set to $4.2 \times 10^8\,\text{W/cm}^2$. The IR pulse was characterized with spectral phase interferometry for direct electric-field reconstruction (SPIDER) [89] giving a time duration of 15 fs. Its peak intensity was set to $1.72 \times 10^{12}\,\text{W/cm}^2$. The vector potential of both pulses was then obtained by numerical integration using the trapezoidal rule. The time step of pump-probe delays in the calculation was 0.25 fs.

The results of the numerical calculations are reported in Fig. 6.6. All the major features observed experimentally are reproduced both in time domain (Fig. 6.6(a)) and frequency domain (Fig. 6.6(b)). Furthermore, our calculations give access to the angular dependence of the electron yield in the polarization plane. In particular, they show that the ω_0 signal appearing at pump-probe temporal overlap in Fig. 6.6(a) disappears when photoelectrons are simultaneously detected in opposite directions.

This asymmetric signal, mainly detected in the 3p-2p QB, is caused

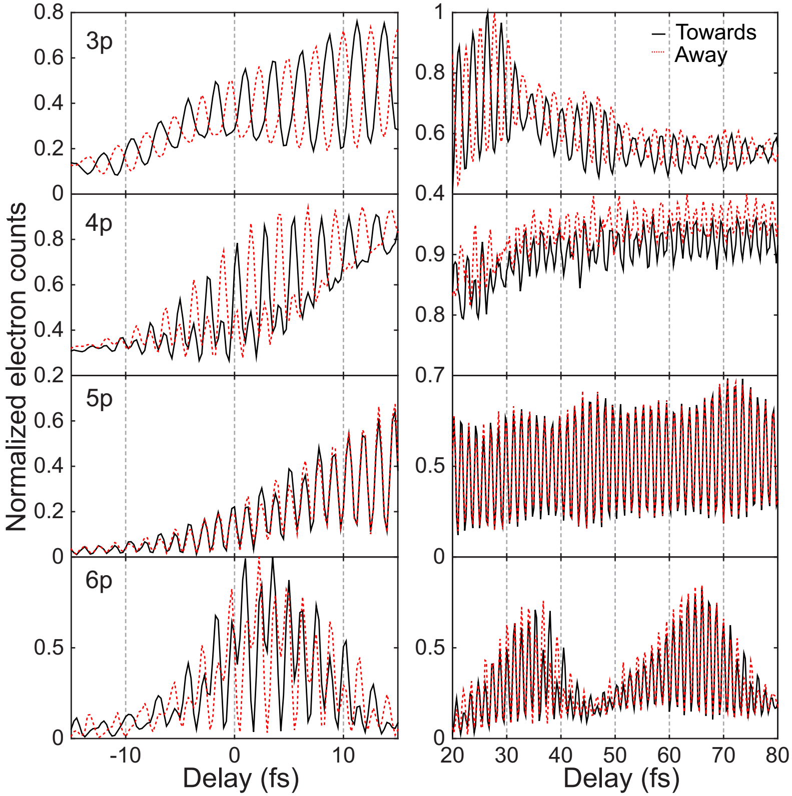

Figure 6.7: Calculated pump-probe signals for 3p to 6p ionization via one IR photon, yielding electrons at 0.21 ± 0.1 eV, 0.68 ± 0.19 eV, 1.02 ± 0.125 eV and 1.23 ± 0.05 eV. The curves represent electrons integrated in a cone with 30° opening angle. The solid black line corresponds to the cone pointing towards the detector whereas for the red dashed line it points in the opposite direction. In contrast to the other QBs, the 3p-2p QB signals emitted in opposite directions are out of phase also for big pump-probe delays (panels on the right column). Adapted from [141].

by two mechanisms: different number of IR photons absorbed in the two ionization pathways and IR induced coupling with nearby dark states. In the case of the signal corresponding to the 3p-2p QB, the electrons originating from the 2p state absorb one photon more than those from the 3p state in order to have the same final energy. As the final states of these two channels have different parity, the resulting signal depends on the direction of detection and therefore oscillates with ω_0 instead of $2\omega_0$.

In contrast, QBs between 2p and the higher lying states (4p, 5p, and 6p), where the same final energy can be reached with the 2p electrons absorbing two additional IR photons, are characterized by a unique parity of the final state and thus symmetric emission. However, this simple picture can be complicated by the coupling with nearby dark states. Indeed, the coupling of the 2p state with the dark 3s and 3d states through the IR field can result in a nonadiabatic polarization of the excited WP leading to an asymmetric emission, which enhances the ω_0 signal. A population analysis performed projecting out the dark 3s and 3d states during the calculations shows a partial suppression of the ω_0 signal corresponding to 3p-2p interference and confirms our picture.

This second source of emission asymmetry can also be detected in the QBs involving the higher states even though the same number of IR photons is absorbed in this case. As it can be seen in Fig. 6.6, a weaker ω_0 component coming from this latter mechanism but involving the dark states 4s and 4d is present also in the emission from the 4p state with two IR photons. Although this signal is weak, it is still observed in the experimental data with short IR pulses (see Fig. 6.5(f)).

Figure 6.7 offers a more detailed view on the induced asymmetries. It shows a comparison between the electrons emitted in a cone with a 30° opening angle pointing either towards the detector (as in the experiment, black solid line) or in opposite direction (red dashed line). At this point, it is convenient to make a distinction between the region of pump-probe overlap (left panels) and the region outside overlap (right panels). At the overlap, some asymmetry in the emission direction is observed for most QBs. The asymmetric signal oscillates with the laser frequency, in agreement with the previous considerations. Outside the overlap, all the QBs besides the 3p-2p signal do not strongly depend on the detection direction.

The asymmetry of the 3p-2p signal lasts even for long pump-probe delays with the frequency gradually shifting from ω_0 towards the 3p-2p beating frequency as the overlap of pulses diminishes (see also Fig. 6.4(c)). This demonstrates that even outside of the region of pulse overlap the QBs can differ in parity. Performing a Legendre polynomial expansion of the

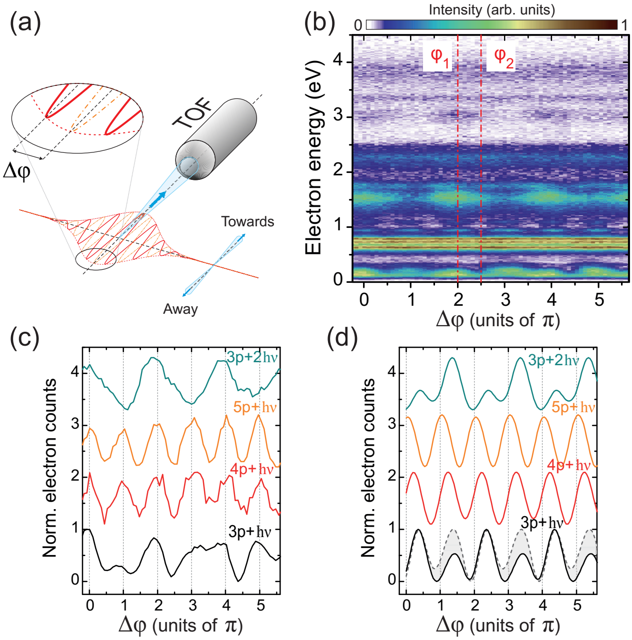

Figure 6.8: CEP dependence of the photoelectron yield at a fixed delay of 90 fs. (a) Schematic of the CEP variation inducing an effective change in the direction of detection. (b) Experimental results. (c)-(d) Comparison between experiment and calculations for selected QBs. The normalized lineouts are separated by an arbitrary offset. A clear 2π periodicity is observed in the 3p-2p QB. Calculations with 3s and 3d states projected out (gray dashed line in (d)) show that the ratio between 2π and π periodicities is strongly influenced by these states. The experimental IR intensity is $\simeq 1.5 \times 10^{12}$ W/cm^2 and 1.72×10^{12} W/cm^2 in the calculations. Adapted from [141].

photoelectron yield, the QBs corresponding to 4p-2p, 5p-2p, and 6p-2p will dominantly appear within the even coefficients, whereas the asymmetric 3p-2p signal will contribute mostly to the odd terms. Thus the previously proposed procedure of Legendre polynomial expansion (reported, e.g., in Ref. [28]) is unable to reliably disentangle the QB signal from the "direct-indirect" interference.

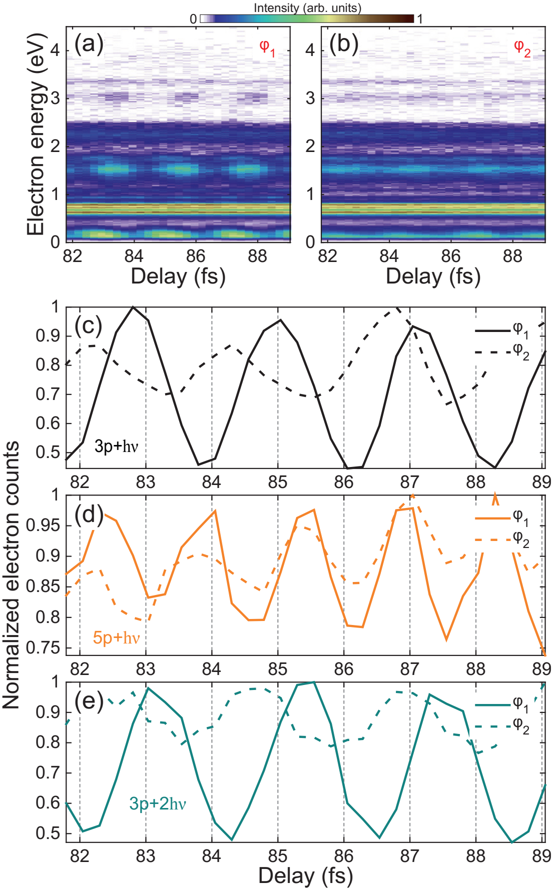

Figure 6.9: Experimental photoelectron spectra as a function of pump-probe delay and for two different values of the CEP, φ_1 (a) and φ_2 (b) marked with vertical red-dashed lines in Fig. 6.8(b). (c)-(e) Selected QBs corresponding to the peak in the electron yield coming from $3\text{p} + h\nu$, $5\text{p} + h\nu$ and $3\text{p} + 2h\nu$ transitions, respectively. Adapted from [141].

6.5 Role of the Carrier-Envelope Phase

Although the experimental setup does not allow us to detect photoelectron spectra in opposite directions, we can probe the same effect by controlling the CEP of the generating IR field. As a CEP shift of π effectively reverses the direction of detection, we expect the amplitude of the 3p-2p QB to modulate with 2π periodicity outside of the pump-probe overlap, while the other QBs should be π-periodic. The experimental results reported in Fig. 6.8 confirm this picture. In addition, the calculations reveal that the non-adiabatic polarization of the EWP is important also for long delays and that the 2π-periodic component of 3p-2p QB is strongly enhanced by the presence of both 3s and 3d states.

By changing the CEP of the driving field, it is also possible to change the position of the attosecond pulses under the envelope of an APT and generate a cosine-like or a sine-like train. As discussed in the previous section, since the periodicity of the QBs is generally not a multiple of the IR cycle, one will expect the observed modulation contrast to strongly depend on the shape of the pump pulse train below the envelope. In order to observe this effect, we performed a delay scan for two values of the CEP differing by $\pi/2$. The values of the CEP correspond to a maximum, φ_1, and a minimum, φ_2, of the 5p yield and are marked by the vertical red dashed lines in Fig. 6.8(b).

The results are presented in the spectrograms shown in Figs. 6.9(a) and 6.9(b). As one can observe, the contrast of the QBs changes strongly with the value of the CEP in a non-uniform way. The QBs which display a strong asymmetric emission (e.g., the 3p-2p QB in Fig. 6.9(c) and Fig. 6.9(e)) is more affected by the shape of the pump pulse, while the signals of the other QBs (e.g., 5p-2p in Fig. 6.9(d)) change less. Furthermore, for QBs characterized by a final state of mixed parity, a change in the CEP produces not only a change in the modulation contrast but also in the timing of the oscillations. This latter effect counteracts the rotation of the IR probe field caused by a change in the CEP

6.6 Conclusion

In conclusion, our results demonstrate that proper tailoring of the harmonic spectrum associated with an APT allows for selective excitation of electronic states, thereby excluding direct ionization. This paves the way for a detailed, background-free study of the EWP evolution in the time window where pump and probe overlap. During this time window, the dynamics of the formed EWP is deeply modified by the intense IR field, which mixes the angular components of the electronic wave function.

Our results show that not all the QBs are characterized by final states of the same parity. In these particular cases, one can control not only the amplitude of the QBs by varying the pump-probe delay but also the preferred direction of photoelectron emission. Comparison with the solution of the TDSE shows that the IR field strongly influences the angular properties of the EWP even when pump and probe do not overlap in time.

Finally, the high photon energies of the high-order harmonics make this technique suitable to study states with binding energies not accessible with IR pulses, e.g., metastable states of molecular dications. Furthermore, the combination of HH excitation with a tunable pump should pave the way for quantum-carpet spectroscopy [169] with attosecond and picometer resolution.

Chapter 7

Ultrafast Fragmentation Dynamics of Ethylene Cation $C_2H_4^+$

In this chapter, we present an experimental study of the fragmentation dynamics of the ethylene cation $C_2H_4^+$ in an XUV-pump-IR-probe scheme that permits us to resolve time-scales on the order of few femtoseconds. The photoexcitation of ethylene above the first ionization threshold followed by an IR probe pulse leads to a rich structure in the ion yields reflecting the fast response of the molecule and the underlying nuclear arrangement. The temporal resolution of our setup enables us to pinpoint dynamics in a temporal window of 200 fs and to set an upper limit of 30 ± 3 fs for the isomerization time to the ethylidene configuration. Additionally, we demonstrate a route to optical control of the important fragmentation pathways leading to dissociation and expulsion of H or H_2.

7.1 Introduction

For the past several decades, the ethylene molecule (C_2H_4) and its photochemical reactions have undergone intense research as they serve as a reference system for organic molecules based on a C=C double bond. This class of molecules plays an important role in chemistry, biology and in the human body [29, 170, 171]. It is known that photoexcitation of ethylene and its cation leads to ultrafast internal conversion processes and rearrangement like twisting, pyramidalization, and isomerization on the femtosecond timescale [172, 173, 174, 175] (Fig. 7.1). In particular, it could be shown that coupling of the potential energy surfaces (PES) through conical intersections (CIs) plays an important role during the evolution of the excited wave packet towards the ground state [176, 177, 178, 179] (Fig. 7.2). Specific attention has been paid to the cation fragmentation channels $C_2H_4^+ \longrightarrow C_2H_3^+ + H$ and $C_2H_4^+ \longrightarrow C_2H_2^+ + H_2$ and the underlying mechanism that influences the associated branching ratios [180, 179].

Lorquet and coworkers [172, 173] identified a CI along the local CH stretch coordinate at the origin of the relaxation and fragmentation dynamics. This CI couples the first excited state of the ethylene cation $\tilde{A}$ with the ground state of the $C_2H_3^+$ ion whose excited state correlates with the ethylene cation ground state $\tilde{X}$. Along this relaxation pathway, the nuclear wave packet can either relax to the ground state or lead to the dissociation $C_2H_3^+ + H$. On the other hand, a more complex sequence interconnects the $\tilde{A}$ and $\tilde{X}$ state by a bridged structure and a consecutive degenerate ethylidene configuration CH_3CH with a vanishing barrier

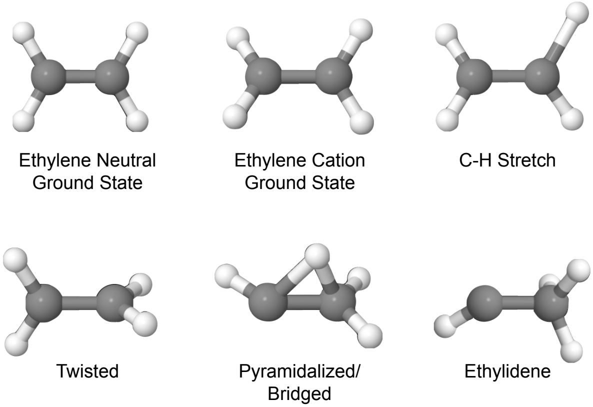

Figure 7.1: Geometrical configurations of ethylene and its cation. The ground state of the ethylene cation differs from the ground state of the neutral in a slight twist angle and elongated bond distances. The C-H stretch and twisted geometries are important contributions to the relaxation pathways whereas the bridged structure is an intermediate state towards the ethylidene configuration and H or H_2 expulsion.

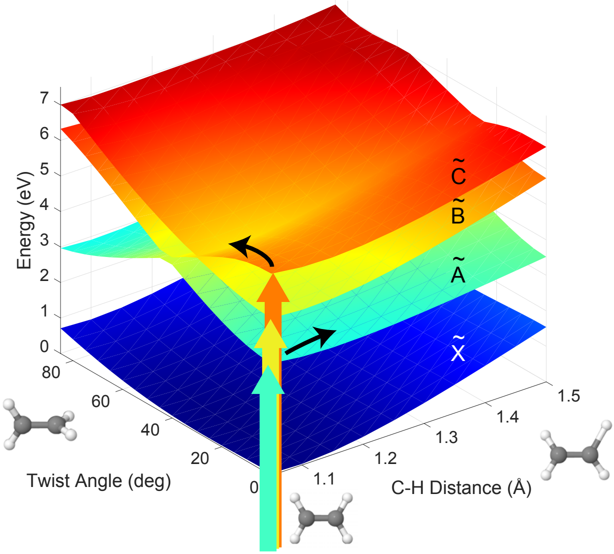

Figure 7.2: Illustration of the potential energy surfaces (PES) along the dihedral twist angle and the C-H stretch coordinate. After excitation (vertical arrows) from the neutral ground state to the first three excited states of the ethylene cation (planar geometry) the nuclear wave packets start evolving on their respective PES along different coordinates leading to changes in the geometry.

towards $C_2H_2^+ + H_2$ [173].

Recently, Suits and coworkers presented a different interpretation in a fully non-adiabatic study based on the ab initio multiple spawning (AIMS) method in which they analyze two distinct classes of CIs along the relaxation pathways, in planar and twisted geometry [179]. For the relaxation to the ground state they proposed a competition between these two channels separated by a barrier of about 3.5 eV. Here, the planar CI was associated with subsequent interconversion to a bridged structure facilitating loss of a H_2 molecule whereas the twisted CI is supposed to lead to torsional vibrations hindering this process. The dependence of the H/H_2 ratio on the internal energy of the molecule that was observed in experiment [181] was linked to the barrier between the planar and torsional CIs and thus the opening of the torsional channel for higher internal energies.

In contrast to theoretical studies, time-dependent experimental investigations on the femtosecond timescale have been rare so far and mostly concentrated on the V state ($\pi\pi^*$, about 7 eV excitation energy) dynamics of ethylene [182, 175, 183]. In a recent study Tilborg et al. [184] presented investigations on the ethylene cation $C_2H_4{}^+$ dynamics in an XUV-pump-IR-probe scheme similar to ours. Their work focused on the delay of the $CH_3{}^+$ peak stemming from breakup of the C=C bond after isomerization of the ethylene cation to the ethylidene cation ($HCCH_3{}^+$) configuration and led to the estimation of an isomerization time of 50 ± 25 fs.

Here, we present a combined experimental and theoretical study of the excited ethylene cation fragmentation dynamics with an improved temporal resolution on the order of few femtoseconds. This temporal resolution allows us to observe unexpected dynamics in a broad set of fragments and allows us to shed light on the control of the previously discussed dissociation channels leading to loss of a hydrogen atom or molecule.

7.2 Experiment

We recorded delay-dependent ion mass spectra in a XUV-pump-IR-probe experiment at the attoline [90] (Sec. 3.2.2) profiting from the high temporal resolution of this attosecond beamline (see section Experimental Methods and Fig. 7.3a)). We use attosecond pulse trains with photon energies in the range of 20 to 30 eV (Fig. 7.3b)) to ionize ethylene molecules from the ground state to different excited states of the cation $C_2H_4{}^+$ (Fig.7.3c)) and probe the evolution of the nuclear wave packets on the PES by means of a delayed IR probe pulse (photon energy 1.6 eV) of variable intensity.

The static ion yield resulting from ionization by the XUV pulses (Fig. 7.4) exhibits three dominant peaks of the cation $C_2H_4{}^+$ and the largest fragments $C_2H_3{}^+$ and $C_2H_2{}^+$ accompanied by the smaller fragments that feature two orders of magnitude lower peak heights. The additional strong peak at 4 u stems from ionization of He that we use as buffer gas with a ratio C_2H_4:He of about 1:10. The static fragment distribution is in good agreement with asymptotic measurements on ethylene at variable photon energies that we use to estimate the initial population of the different excited states [186, 187] (Fig.7.3d)). To achieve a precise time zero calibration

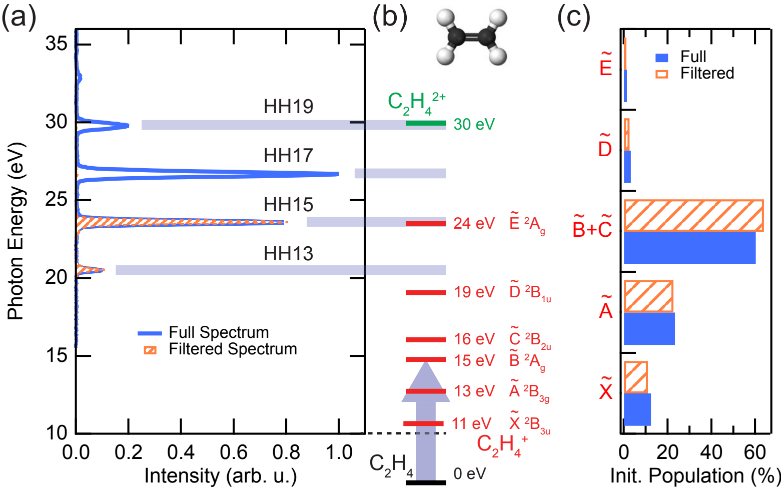

Figure 7.3: (a) Full harmonic excitation spectrum with peaks between 20 and 30 eV (solid line) and spectrum limited below 24.5 eV by using a tin foil (dashed line). (b) Ionization from the ground state (black) to a manifold of cation excited states (red) [185]. (c) Initial relative population of the cation states calculated for both XUV spectra [186].

for pump-probe delay, we analyze the IR-induced oscillations in the He^+ yield from the buffer gas in the region of temporal overlap [188] (Section Experimental Methods) as shown in Fig. 7.5. The narrow $4\omega_{IR}$ contribution is therefore fitted with a Gaussian function.

In order to interpret the observed dynamics in the various fragment yields, we apply and extend a model that has recently been introduced for the description of ultrafast fragmentation dynamics of ethylene [184]. To account for the delayed population of IR-active configurations we fit the acquired data with the sum of Gaussian functions convoluted with exponential decays. We use sums of exponentially modified Gaussian functions (EMGs) [189] as analytic approximation of this convolution. Each fragment yield is fitted individually with a combination of a minimal number of constituting EMGs necessary to reach a good agreement with the data. We estimate the error of the obtained peak positions based on the fitting error of the position of the Gaussian part of the convoluted fitting function and find it to be ±3 fs for all peaks except for CH+ where it increases to

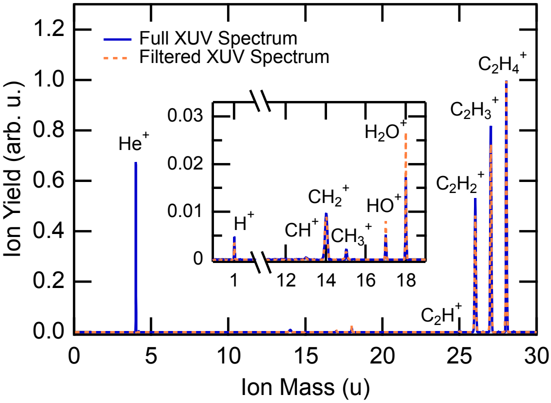

Figure 7.4: Measured reference ion fragment spectra of the applied He/C_2H_4 gas mix for ionization with the XUV spectra shown in Fig. 7.3. The yields of the smaller fragments are shown as inset with a scale enlarged by two orders of magnitude.

±10 fs due to the noise level of this fragment data.

7.3 Results

In Fig. 7.6 we present the measured IR-induced relative ion yields as a function of pump-probe delay for an IR intensity of $2.5\times10^{12}\,\mathrm{W/cm^2}$, a delay step size of 2 fs and accumulation over an average of 20000 laser shots per data point. The relative ion yield depicts the relative change of each fragment yield induced by the IR probe pulse at a certain delay with the XUV-only yield as reference. For positive delays the IR pulses arrive after the XUV pulses. The data points of all ion yields that show a dynamic behavior are plotted as markers together with their respective fit that we use to extract the delay position of the peaks. Pleas note that for the sake of clearness some curves have been shifted by an arbitrary vertical offset that is indicated next to the data points. We observe diverse dynamics in all ion yields with peaks that range from temporal overlap of the pump and probe pulse up to about 60 fs.

Before turning to the discussion of the most important features in the experimental data, we would like to study the dependence of the observed

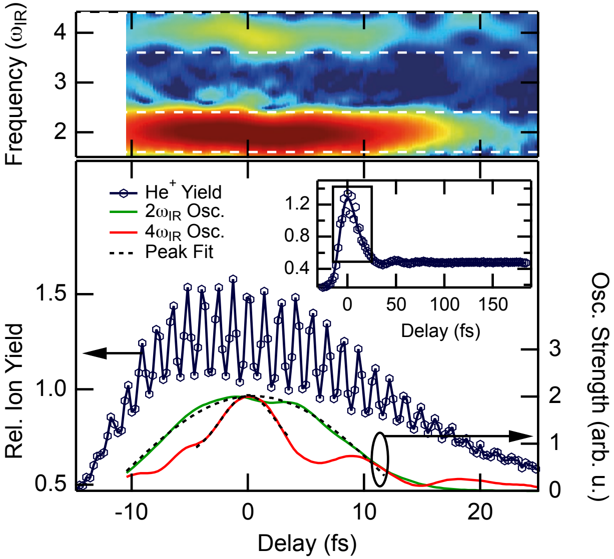

Figure 7.5: Lower panel: The oscillations in the He$^+$ yield visible in a fine scan around temporal pump and probe overlap can be used to precisely calibrate the delay-zero [188]. For this, we perform a time-frequency analysis of the oscillating yield and use the confined $4\omega_{IR}$ contribution, fitted by a Gaussian function, to calibrate the delay axis in our experiment.

ion yields on the pump and probe characteristics. We therefore perform identical scans at decreasing IR intensities of 1.9, 1.2, and 0.6×10^{12} W/cm^2 (Fig. 7.7a)-c)) and one additional scan for an excitation spectrum with photon energies limited to below 24.5 eV less than the second ionization threshold of ethylene at 30 eV in order to rule out possible contribution from the dication (Fig. 7.7d)).

For the case of reduced IR intensities, we observe very similar shapes of the fragment yields and unchanged time constants. The main difference stems from the decrease in peak height of the features with decreasing intensity. In order to characterize the IR probe process in detail, we extract the peak height of the different relative ion yields as function of IR intensity (Fig. 7.8). The height of the peaks shows a clear linear decrease with decreasing intensity which indicates a probe process that is essentially based on one-IR-photon transitions.

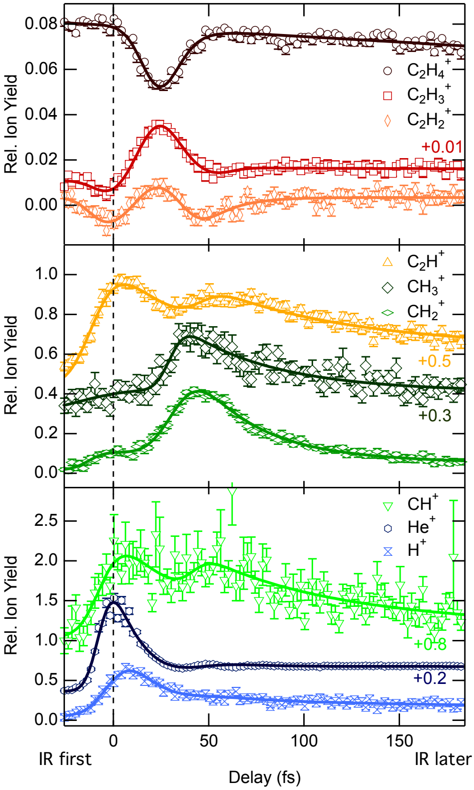

Figure 7.6: IR-induced relative change of the ion yields for all observable species at an IR intensity of 2.5×10^{12} W/cm^2. Markers represent the measured data, solid lines represent the fits using a model as described in the main text. Negative delays stand for IR pulses that arrive before the XUV. Some curves are shifted vertically for better visibility, indicated by the numbers next to the curves. The error bars indicated the standard deviation of the mean value of 10 identical scans.

The use of a filtered XUV spectrum below 24.5 eV strongly reduces the total ion yield due to much lower XUV flux (25% maximal transmittance of the employed tin foil) but also results in similar dynamics in the ion yields compared to the case of excitation with the full spectrum. We can therefore exclude contributions from the dissociation of ethylene dications due to the proximity of the second ionization threshold to the highest photon energies. This observation is in good agreement with the similarity of

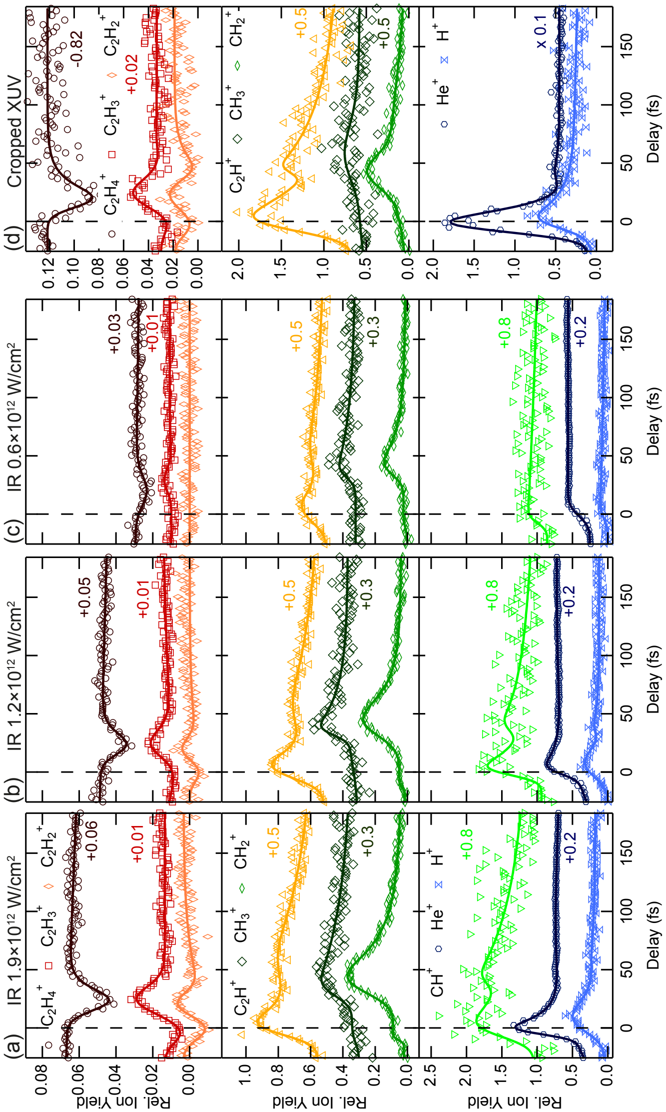

Figure 7.7: IR-induced changes of the ion yields as in Fig. 7.6, but for decreasing IR intensities in the probe pulse (a)-(c) and for the case of the cropped XUV pump spectrum at an IR intensity of 2.5×10^{12} W/cm^2 (d). The main features and their time constants are unaffected by the change in intensity and the XUV excitation spectrum.

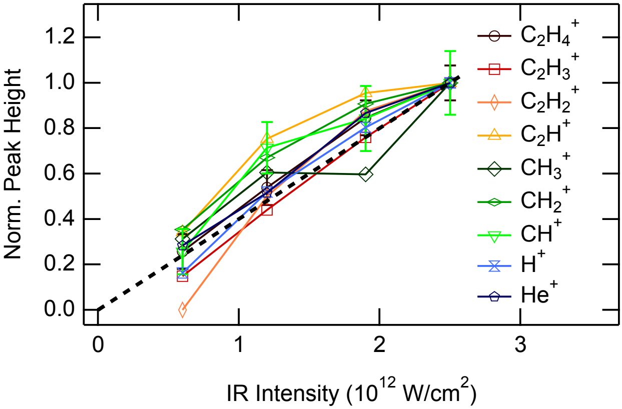

Figure 7.8: Peak heights of the ion yields representing the signal strength as function of the IR intensity, normalized to their value at the highest intensity. The strength of the signal shows a linear increase with increasing IR intensities indicating that the probe process represents a single photon process. For clarity, error bars are only shown for two representative fragments $C_2H_4{}^+$ and CH^+.

the calculated initial populations for both excitation spectra as shown in Fig. 7.3d).

In this work, we concentrate our analysis on two main features in the observed yields. One is the dynamics in the $C_2H_4{}^+$, $C_2H_3{}^+$, and $C_2H_2{}^+$ ion yields that are closely linked through the dissociation channels leading to the loss of a hydrogen atom or molecule. The other feature is the evolution of the $CH_3{}^+$, $CH_2{}^+$, and CH^+ yields resulting from breakup of the C=C bond.

We observe a comparable behavior in the ion yields of the mono-carbon fragments CH^+, $CH_2{}^+$ and $CH_3{}^+$ that all exhibit maxima around 40 fs. Among them, the presence of $CH_3{}^+$ fragments is particularly interesting since it is an unambiguous signature of the isomerization to the ethylidene configuration and was previously used to extract the isomerization time of the ethylene cation [184]. The extraction of the isomerization time in a pump-probe experiment essentially constitutes a three-step process: The ionization is succeeded by the isomerization to ethylidene $CH{=}CH_3{}^+$ via a bridged or twisted-pyramidalized structure which takes place with a certain time constant. This interconversion is followed by the IR-induced breaking of the C=C bond which might require an additional time delay before the molecule reaches a configuration that is more susceptible to the probe pulse.

Our observation of the peak in the CH_3^+ yield thus restricts us to the extraction of an upper limit for the isomerization time. In contrast to previous studies on the isomerization time [184] based on the same probe channel, we profit from our precise time-zero calibration, the time resolution and the good statistics of our measurements. Therefore, we can use a fit to the peak to derive an upper limit of the $C_2H_4^+$ to ethylidene $CH_3^+{=}CH$ isomerization time of 30 ± 3 fs. After convolution with the instrument response function, that is mainly given by the probe pulse duration, this leads to the observed maximum yield at 40 fs.

A more fundamental process than the isomerization is the loss of one or two H atoms after photoexcitation of the molecule. A signature of this process in the static case are the two dominant peaks at masses of 26 u and 27 u stemming from $C_2H_3^+$ and $C_2H_2^+$, respectively (Fig. 7.4). In our pump-probe experiment we observe delay-dependent features belonging to these channels, namely the decrease in the $C_2H_4^+$ ion yield around 25 fs which coincides with peaks in the $C_2H_3^+$ and $C_2H_2^+$ yields. The correlation of these channels and the boundedness of the features to the early pump-probe delays suggest the following interpretation:

After ionization of the molecule by the XUV, a nuclear wave packet evolves on the PESs towards the cation ground state. During its trajectory, it passes a junction that leads to a statistical splitting with parts relaxing to the ground state $C_2H_4^+$ on the one hand and to dissociative channels leading to $C_2H_3^+$ and $C_2H_2^+$ on the other hand. The interaction of the IR pulse with the nuclear wave packet at this specific configuration enhances the branching ratio in favor of the dissociative channels. In our pump-probe experiment this is visible as a depletion in the $C_2H_4^+$ yield and simultaneous increase of the fragments $C_2H_3^+$ and $C_2H_2^+$ (Fig. 7.6). We therefore demonstrate the control of this dissociation channel by means of a delayed IR pulse at moderate intensities.

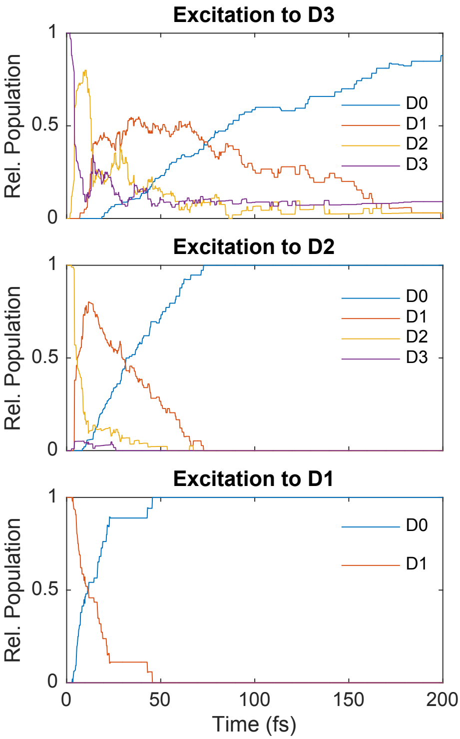

Figure 7.9: Calculated population of the four lowest PES of the ethylene cation as a function of time for initial excitation on the three lowest excited states D1 to D3. The calculations were performed by the group of U. Rothlisberger (EPF Lausanne).

7.4 Simulation

In order to gain further insight into the dynamics of the excited ethylene cation, the group of U. Rothlisberger (EPF Lausanne) performed trajectory surface hopping (TSH) calculations based on time-dependent density functional theory (TDDFT) and the 6-31G** basis set on the PBE0-TDDFT level of theory using an initial population of 100 per excited state [190]. We verified a good agreement of the representation of the spectroscopic states ($\tilde{X}^2B_{3u}$, $\tilde{A}^2B_{3g}$, $\tilde{B}^2A_g$, and $\tilde{C}^2B_{2u}$) based on the neutral molecule and the theoretical states (D0, D1, D2, and D3) calculated for the cation.

The calculations allow us to link experimentally observed dynamics to the evolution of the nuclear wave packets in the theoretical model. It is worth noting that the experimental IR-induced changes are prominent, but still affect only few percent of the overall dynamics that lead to dissociation to $C_2H_3{}^+$ and $C_2H_2{}^+$. Thus, only a small fraction of the evolving trajectories is expected to be susceptible to the IR probe pulse, which renders this analysis challenging. We calculate the initial population of the ethylene cation states based on the experimental XUV spectrum [186, 187] and find a population of above 95% confined to the cation ground state $\tilde{X}^2\mathrm{B}_{3\mathrm{u}}$ and the first three excited states $\tilde{A}^2\mathrm{B}_{3\mathrm{g}}$, $\tilde{B}^2\mathrm{A}_{\mathrm{g}}$, and $\tilde{C}^2\mathrm{B}_{2\mathrm{u}}$ (Fig.7.3d)). We therefore concentrate our calculations on the excitation on the first three excited states (D1, D2, and D3).

The temporal evolution of the nuclear wave packet on the different states (Fig. 7.9) is in good agreement with recent calculations using the AIMS method [179]. We confirm the fast relaxation of the majority of the initial population to the ground state within the first 50 fs after excitation. In contrast to this previous study, we start our calculations from the neutral ground state (planar) geometry to comply with the experiment.

It has been shown that the lowest PES of the ethylene cation is involved in the dynamics leading to the H or H_2 dissociation [173, 172]. We find, that it takes the nuclear wave packet about 20 fs to reach the cation ground state PES starting with an initial excitation to the second or third excited state. Therefore, an IR pulse arriving to this amount of time after the excitation could possibly act on the dynamics and alter the fragmentation ratio. The experimentally observed delay of 25 fs for the IR-induced fragmentation change is in good agreement with this relaxation timescale observed in our theoretical model.

For a further analysis, we extract the dihedral twist angles [191] for all calculated trajectories. In the case of the dihedral angles we observe a rapid increase of the spread after an initially narrow excitation around 0° reflecting the planar geometry (Fig. 7.10(a)). For times later than 25 fs we observe the excitation of torsional modes that are visible as a spread in the dihedral angular distribution. The excitation of rotational vibrations and the redistribution of energy along other coordinates could lead to a

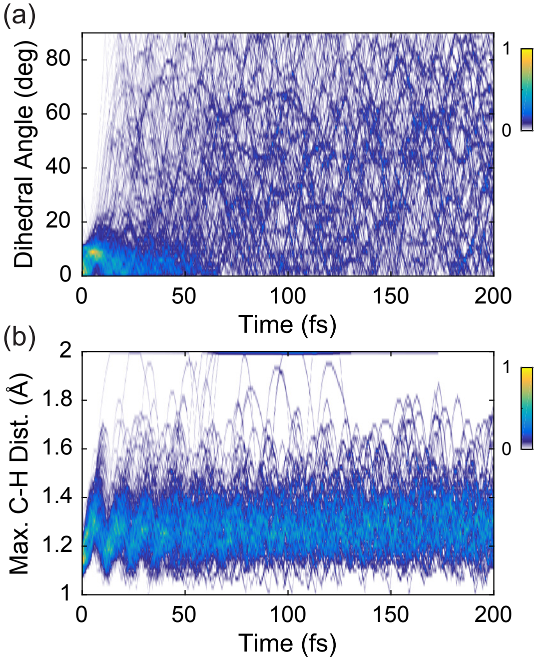

Figure 7.10: Calculated temporal evolution of the dihedral angle (a) and the maximal C-H distances per molecule (b) after equal excitation on the first three excited states of the ethylene cation. (a) At times between 25 fs and 50 fs, the distribution starts to spread over the whole parameter space. (b) After excitation, the C-H bonds exhibit coherent oscillations until around 40 fs. The calculations were performed by the group of U. Rothlisberger (EPF Lausanne).

closing of the channel along the C-H stretch coordinate responsible for H dissociation.

For the case of the C-H stretch coordinate, represented by the maximal C-H distance for each molecule, we observe coherent oscillations up to 40 fs (Fig. 7.10(b)). Based on the period of these oscillation, the excited molecule could oscillate twice along the C-H stretch coordinate within the experimentally observed delay time of the IR-induced increase of the H channel.

Additionally, we extract from our simulations the geometries of the molecule when the wave packet undergoes a transition from one PES to another (hopping). We present the distributions of C-H stretch coordi-

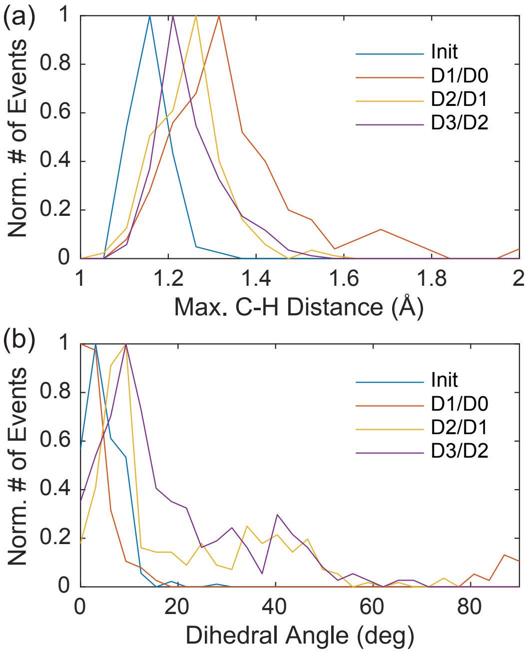

Figure 7.11: Distribution of the maximal C-H distances (a) per molecule and the dihedral angle (b) for initial excitation (Init) and hopping events to different PES (D0, D1, and D2). The transitions to PES D0 occur favorably for stretched C-H coordinates and are confined to angles around 0° and 90°. The calculations were performed by the group of U. Rothlisberger (EPF Lausanne).

nates and dihedral angles of hopping events for transitions to different PES together with the initial excitation geometry in Fig. 7.11(a) and (b). We observe the largest C-H distances for the transitions D1/D0 to the cation ground state, underlining the involvement of this transition in the dissociation channel leading to loss of an H atom. For the dihedral angle, we observe a partitioning of the hopping geometries to D0 around planar and few events around twisted geometry in contrast to a broad spread from 0° to 60° for the transitions to D2 and D1. From our calculations we can see that for early times transitions to the ground state dominantly occur close to the initial geometry (planar configuration). Just after 30 fs, the twisted channel described by Suits and coworkers [179] with a dihedral angle around 90° starts to play a role in the hopping to D0. This is supposed to be mainly due to the excitation of twist vibrations that open this channel.

A complete understanding of the unique mechanism leading to the IR-induced enhancement of the H/H_2 dissociation channels requires a more advanced theoretical study including the probe pulse. This is necessary to identify the specific configuration of the molecule enhancing this dissociation channel. Experimentally, we demonstrated the use of the IR pulse as a precise stop watch for the nuclear wave packet dynamics reaching this specific region on the PES.

7.5 Conclusion

In summary, we present investigations of the ultrafast photodissociation dynamics of the ethylene cation $C_2H_4{}^+$ excited by a XUV pulse train and probed with a delayed near-infrared pulse. The recorded delay-dependent fragment yields exhibit rich dynamics on timescales between 5 and 60 fs that we link to calculations based on the TSH method in a PBE0-TDDFT theory. We observe a localized IR-induced enhancement in the $C_2H_3{}^+ + H$ and $C_2H_2{}^+ + H_2$ channels after 25 fs that we attribute to wave packets reaching the conical intersection leading to the ground state $\tilde{X}^2B_{3u}$. Thus we present experimental evidence for the ultrafast timescale of the relaxation processes and demonstrate the optical control of this dissociation pathway. The peak of the $CH_3{}^+$ ion around 40 fs, which is a signature of the ethylene to ethylidene isomerization, allows us to pin-point an upper limit of the isomerization time of 30 ± 3 fs. Our measurements represent, to the best of our knowledge, the studies of fragmentation dynamics of the ethylene cation with the highest temporal resolution thus far. They reveal dynamics on the timescale on the order of 10 fs that were previously inaccessible due to larger instrument response times. Thus, our findings pave the way for a comparison with more detailed theoretical analyses of the fragmentation process in order to assign clear quantum trajectories to the emerging fragment peaks.

Chapter 8

Conclusion and Outlook

The results presented in this thesis cover four different aspects in the frame of ultrafast ionization dynamics in atoms and molecules. These aspects can be assigned to two different physical regimes, namely strong-field ionization and single-photon excitation or ionization. Therefore, the experiments used and improved upon two preexisting setups. The first experiment is based on laser systems directly applied in the strong-field experiments at wavelengths of 800 nm and 3.4 µm. The second setup is the attosecond beamline "the attoline" based on the generation of high-order harmonics of wavelengths between 15 and 70 nm. After shortly introducing the basic physical principles in Chapter 2, in Chapter 3 we presented the experimental setups that were extended and applied in the frame of this thesis.

In the first experimental part in Chapter 4, we conducted a study of strong-field ionization in the long-wavelength regime at mid-infrared (MIR) wavelengths. We therefore used a state-of-the-art OPCPA source capable of delivering laser pulses at a wavelength of 3.4 µm with pulse durations of 44 fs and energies up to 21.8 µJ. We applied these laser pulses in the ionization of noble gases at intensities on the order of 10^{13} W/cm^2. We recorded the resulting photoelectron momentum distributions (PMDs) by means of a velocity map imaging spectrometer optimized for the acquisition of high-energy electrons. The resulting PMDs exhibited a clear signature of non-dipole magnetic field effects visible as asymmetry along the beam propagation direction. We quantified this asymmetry as offset of the peak of the distribution opposite to the beam propagation direction. We also performed semi-classical calculations of the ionization process for the experimental parameter range. The experimental observation could only be reproduced by simulations by taking into account the dynamics in the combined full electromagnetic and Coulomb potential. We therefore concluded that the onset of magnetic field effects at MIR wavelengths, and thus the breakdown of the electric dipole approximation, occurs at surprisingly low intensities. Long-wavelength laser fields are considered to be a promising tool for the extension of table-top spectroscopy methods to the keV range with zeptosecond resolution [21, 22, 23]. Therefore, our findings have important implications for the theoretical treatment of ionization processes in the frame of high-order harmonic generation.

Further investigations of non-dipole effects in strong-field ionization in the long-wavelength regime could cover possible asymmetries in the holographic or low-energy structure [19, 36] in 2D photoelectron spectra. This structure contains information about the scattering of electron wave packets on sub-cycle timescales as well as Ångström length scales. As such it constitutes a promising tool for investigations of molecular ionization dynamics. Additionally, a tomographic study involving different ellipticities of the MIR pulses could potentially reveal the mechanism and the exact contributions to the offset of the momentum distribution. Here, the full 3D momentum distribution is accessible and allows for the separate analysis of different regions of the momentum distribution, e.g., the isolation of the central part.

The second part of this thesis covered experiments in the frame of attosecond science. In Chapter 5 we demonstrated a new iterative scheme for the complete temporal reconstruction of attosecond pulses based on ptychography. A basic requirement for the measurement of ultrafast ionization dynamics in atoms, molecules, and solid-state targets is the extraction of temporal information of the pulses used in attosecond experiments. Our new scheme for reconstruction is based on attosecond streaking spectrograms as is the case for the established algorithms PCGPA and LSGPA. Attosecond streaking spectrograms are photoelectron momentum distributions resulting from ionization of a noble gas target in an XUV-IR cross-correlation measurement. It requires combining the field of a single attosecond pulse and a time-delayed infrared pulse acting as a gating function that modulates the final energy of the electrons. The temporal information of the ionizing XUV pulse is encoded in this delay-dependent spectrogram and can be extracted by reconstructing the spectrogram as is the case of optical blind FROG measurements. The advantage of our new ptychographic reconstruction scheme is its flexibility and the low requirements it imposes on the measured streaking spectrograms. In contrast to PCGPA and LSGPA, it requires neither equidistant nor fine sampling of the delay steps and functions even for data with a low signal-to-noise level. We showed the robustness of the scheme towards coarse delay-sampling, low signal-to-noise ratios and interference resulting from multiple attosecond pulses. This was based on sets of simulated traces in a comparison with PCGPA and LSGPA. We further proved its functioning and reliability with an experimental streaking spectrogram. The ptychographic reconstruction of attosecond pulses introduced in this thesis enables improved results with reduced computational effort and allows for a faster complete temporal characterization of attosecond pulses.

The release of this reconstruction algorithm as a free download paves the way for broad applications in attosecond experiments where it will prove its versatility. Possible extensions include the consideration of non-constant ionization cross sections inherent in experimental data. This could enhance the precision of the temporal characterization, assist experiments involving attosecond streaking for the extraction of ionization time-delays, and allow for this information to be measured.

In Chapter 6, we performed an attosecond quantum beat spectroscopy study of helium excited states. To do so we applied a specially tailored harmonic spectrum confined below the ionization threshold together with a time-delayed infrared probe-pulse. We recorded photoelectron spectra as a function of the XUV-IR delay and found clear oscillating quantum beat signals differing in frequency and phase. We were able to assign these signals to the involved excited states based on a time-frequency analysis. We presented calculations of the time-dependent Schrödinger equation matching the experimental parameters and found a very good agreement between the experimental and theoretical photoelectron spectra. The calculated photoelectron spectra revealed an angular dependence of the quantum beat amplitudes. This results from the difference in parity of the final states involved as well as contributions from a coupling of the np to dark s and d states in the pump-probe overlap. We proved this emission anisotropy in the experiment by switching the CEP of the IR probe pulse by π which effectively inverted the detection direction of our time-of-flight detector. We demonstrated that the angular dependence can successfully be exploited in a scheme where the CEP and the delay of the IR field is used to control not only the amplitude but also the photoelectron emission direction at energies involving final states with different parity. Our findings provide the first evidence of anisotropy in the quantum beat signal that was previously assumed to be isotropic [28].

For future studies, the demonstration of direct-ionization-free attosecond quantum beat spectroscopy of states with energies in the XUV range opens the way towards applications in molecular systems [192]. This includes attosecond quantum carpet spectroscopy with attosecond precision and picometer resolution [169].

In Chapter 7 we presented a study of ultrafast fragmentation dynamics of the ethylene cation ${C_2H_4}^+$ after excitation with an XUV pulses below the second ionization threshold of ethylene. In order to conduct this experiment, we extended the attoline for applications in photoion detection by means of ion-mass spectrometry based on a time-of-flight spectrometer including a repeller electrode. First, we ionized ethylene molecules by XUV pulses leading to the population of the first three excited cationic states. Next, we probed the evolution of the resulting nuclear wave packet by an IR-induced transition to different dissociative channels. We were therefore able to resolve dynamics in the fragment ion yields with unprecedented temporal resolution. We demonstrated the optical control of a channel leading to enhanced dissociation and the expulsion of H and H_2 at a pump-probe delay of about 25 fs. Additionally, we were able to pin-point the isomerization time to ethylidene to 30 ± 3 fs in agreement with the previously observed isomerization time of 50 ± 25 fs. Our findings yield direct insight into the ultrafast relaxation, isomerization and fragmentation dynamics of ethylene and pose new challenges for the theoretical description of dynamics in excited hydrocarbon systems.

Further investigations of the ionization dynamics of ethylene could include kinematically complete measurements of the resulting fragments, e.g., in a COLTRIMS apparatus [68]. This would allow the extraction of the delay-dependent fragment momenta and kinetic energy release as additional parameters for the reconstruction of the nuclear wave packet dynamics. One challenge for such measurements based on coincidence detection is the requirement of good statistics and thus long acquisition times and high-repetition sources with repetition rates in the MHz regime [193, 194].

To conclude, this thesis presents advancements in the understanding of atomic and molecular ionization dynamics centered around elementary prototype systems. It opens promising paths for future studies and the extension of the applied techniques to more complex structures in combination with sophisticated theoretical models.

References

[1] I. Bars and J. Terning, Extra Dimensions in Space and Time, Springer New York, New York, NY (2010)

[2] E. Muybridge, “The Horse in Motion,” (1878)

[3] H. E. Edgerton, “Bullet through Apple,” (1964)

[4] T. H. Maiman, “Stimulated Optical Radiation in Ruby,” Nature 187 (4736), 493 (1960)

[5] A. H. Zewail, “Femtochemistry: Atomic-Scale Dynamics of the Chemical Bond,” J. Phys. Chem. A 104 (24), 5660 (2000)

[6] M. Dantus, M. J. Rosker, and A. H. Zewail, “Real-time femtosecond probing of “transition states” in chemical reactions,” J. Chem. Phys. 87 (4), 2395 (1987)

[7] M. T. Hassan, A. Wirth, I. Grguras, A. Moulet, T. T. Luu, J. Gagnon, V. Pervak, and E. Goulielmakis, “Invited Article: Attosecond photonics: Synthesis and control of light transients,” Rev. Sci. Instrum. 83 (11), 111301 (2012)

[8] A. McPherson, G. Gibson, H. Jara, U. Johann, T. S. Luk, I. A. McIntyre, K. Boyer, and C. K. Rhodes, “Studies of multiphoton production of vacuum-ultraviolet radiation in the rare gases,” J. Opt. Soc. Am. B 4 (4), 595 (1987)

[9] M. Ferray, A. L’Huillier, X. F. Li, L. A. Lompre, G. Mainfray, C. Manus, and L. A. Lompré, “Multiple-harmonic conversion of 1064 nm radiation in rare gases,” J. Phys. B: At. Mol. Opt. Phys. 21 (3), 31 (1988)

[10] E. Goulielmakis, Z.-H. Loh, A. Wirth, R. Santra, N. Rohringer, V. S. Yakovlev, S. Zherebtsov, T. Pfeifer, A. M. Azzeer, M. F. Kling, S. R. Leone, and F. Krausz, “Real-time observation of valence electron motion,” Nature 466 (7307), 739 (2010)

[11] M. Schultze, M. Fieß, N. Karpowicz, J. Gagnon, M. Korbman, M. Hofstetter, S. Neppl, A. L. Cavalieri, Y. Komninos, T. Mercouris, C. A. Nicolaides,

R. Pazourek, S. Nagele, J. Feist, J. Burgdörfer, A. M. Azzeer, R. Ernstorfer, R. Kienberger, U. Kleineberg, E. Goulielmakis, F. Krausz, and V. S. Yakovlev, "Delay in photoemission," Science 328, 1658 (2010)

[12] F. Calegari, D. Ayuso, A. Trabattoni, L. Belshaw, S. De Camillis, S. Anumula, F. Frassetto, L. Poletto, A. Palacios, P. Decleva, J. B. Greenwood, F. Martín, and M. Nisoli, "Ultrafast electron dynamics in phenylalanine initiated by attosecond pulses," Science 346 (6207), 336 (2014)

[13] P. M. Kraus, B. Mignolet, D. Baykusheva, A. Rupenyan, L. Horny, E. F. Penka, G. Grassi, O. I. Tolstikhin, J. Schneider, F. Jensen, L. B. Madsen, A. D. Bandrauk, F. Remacle, and H. J. Worner, "Measurement and laser control of attosecond charge migration in ionized iodoacetylene," Science 350 (6262), 790 (2015)

[14] C. Ott, A. Kaldun, L. Argenti, P. Raith, K. Meyer, M. Laux, Y. Zhang, A. Blättermann, S. Hagstotz, T. Ding, R. Heck, J. Madroñero, F. Martín, and T. Pfeifer, "Reconstruction and control of a time-dependent two-electron wave packet," Nature 516 (7531), 374 (2014)

[15] M. Schultze, E. M. Bothschafter, A. Sommer, S. Holzner, W. Schweinberger, M. Fiess, M. Hofstetter, R. Kienberger, V. Apalkov, V. S. Yakovlev, M. I. Stockman, and F. Krausz, "Controlling dielectrics with the electric field of light," Nature 493 (7430), 75 (2013)

[16] M. Schultze, K. Ramasesha, C. Pemmaraju, S. Sato, D. Whitmore, A. Gandman, J. S. Prell, L. J. Borja, D. Prendergast, K. Yabana, D. M. Neumark, and S. R. Leone, "Attosecond band-gap dynamics in silicon," Science 346 (6215), 1348 (2014)

[17] R. Locher, L. Castiglioni, M. Lucchini, M. Greif, L. Gallmann, J. Osterwalder, M. Hengsberger, and U. Keller, "Energy-dependent photoemission delays from noble metal surfaces by attosecond interferometry," Optica 2 (5), 405 (2015)

[18] C. I. Blaga, F. Catoire, P. Colosimo, G. G. Paulus, H. G. Muller, P. Agostini, and L. F. DiMauro, "Strong-field photoionization revisited," Nat. Phys. 5 (5), 335 (2009)

[19] Y. Huismans, A. Rouzee, A. Gijsbertsen, J. H. Jungmann, A. S. Smolkowska, P. S. W. M. Logman, F. Lepine, C. Cauchy, S. Zamith, T. Marchenko, J. M. Bakker, G. Berden, B. Redlich, A. F. G. van der Meer, H. G. Muller, W. Vermin, K. J. Schafer, M. Spanner, M. Y. Ivanov, O. Smirnova, D. Bauer, S. V. Popruzhenko, and M. J. J. Vrakking, "Time-Resolved Holography with Photoelectrons," Science 331 (6013), 61 (2011)

[20] M. Meckel, A. Staudte, S. Patchkovskii, D. M. Villeneuve, P. B. Corkum, R. Dörner, and M. Spanner, "Signatures of the continuum electron phase in molecular strong-field photoelectron holography," Nat. Phys. 10 (8), 594 (2014)

[21] T. Popmintchev, M.-C. Chen, P. Arpin, M. M. Murnane, and H. C. Kapteyn, "The attosecond nonlinear optics of bright coherent X-ray generation," Nat. Photonics 4 (12), 822 (2010)

[22] T. Popmintchev, M.-C. Chen, D. Popmintchev, P. Arpin, S. Brown, S. Alisauskas, G. Andriukaitis, T. Balciunas, O. D. Mucke, A. Pugzlys, A. Baltuska, B. Shim, S. E. Schrauth, A. Gaeta, C. Hernandez-Garcia, L. Plaja, A. Becker, A. Jaron-Becker, M. M. Murnane, and H. C. Kapteyn, "Bright Coherent Ultrahigh Harmonics in the keV X-ray Regime from Mid-Infrared Femtosecond Lasers," Science 336 (6086), 1287 (2012)

[23] M.-C. Chen, C. Mancuso, C. Hernandez-Garcia, F. Dollar, B. Galloway, D. Popmintchev, P.-C. Huang, B. Walker, L. Plaja, A. A. Jaro -Becker, A. Becker, M. M. Murnane, H. C. Kapteyn, and T. Popmintchev, "Generation of bright isolated attosecond soft X-ray pulses driven by multicycle midinfrared lasers," Proc. Natl. Acad. Sci. 111 (23), E2361 (2014)

[24] H. R. Reiss, "Limits on Tunneling Theories of Strong-Field Ionization," Phys. Rev. Lett. 101 (4), 043002 (2008)

[25] H. R. Reiss, "Relativistic effects in nonrelativistic ionization," Phys. Rev. A 87 (3), 033421 (2013)

[26] H. R. Reiss, "The tunnelling model of laser-induced ionization and its failure at low frequencies," J. Phys. B: At. Mol. Opt. Phys. 47 (20), 204006 (2014)

[27] C. T. L. Smeenk, L. Arissian, B. Zhou, A. Mysyrowicz, D. M. Villeneuve, A. Staudte, and P. B. Corkum, "Partitioning of the Linear Photon Momentum in Multiphoton Ionization," Phys. Rev. Lett. 106 (19), 193002 (2011)

[28] J. Mauritsson, T. Remetter, M. Swoboda, K. Klünder, A. L'Huillier, K. J. Schafer, O. Ghafur, F. Kelkensberg, W. Siu, P. Johnsson, M. J. J. Vrakking, I. Znakovskaya, T. Uphues, S. Zherebtsov, M. F. Kling, F. Lépine, E. Benedetti, F. Ferrari, G. Sansone, and M. Nisoli, "Attosecond Electron Spectroscopy Using a Novel Interferometric Pump-Probe Technique," Phys. Rev. Lett. 105 (5), 053001 (2010)

[29] R. Schoenlein, L. Peteanu, R. Mathies, and C. Shank, "The first step in vision: femtosecond isomerization of rhodopsin," Science 254 (5030), 412 (1991)

[30] S. Hahn and G. Stock, "Quantum-Mechanical Modeling of the Femtosecond Isomerization in Rhodopsin," J. Phys. Chem. B 104 (6), 1146 (2000)

[31] A. Einstein, "Über einen die Erzeugung und Verwandlung des Lichtes betreffenden heuristischen Gesichtspunkt," Ann. Phys. 322 (6), 132 (1905)

[32] M. Göppert-Mayer, "Über Elementarakte mit zwei Quantensprüngen," Ann. Phys. 401 (3), 273 (1931)

[33] L. V. Keldysh, "Ionization in the field of a strong electromagnetic wave," Sov. Phys. JETP 20 (5), 1307 (1965)

[34] P. Eckle, A. N. Pfeiffer, C. Cirelli, A. Staudte, R. Dörner, H. G. Muller, M. Buttiker, and U. Keller, "Attosecond Ionization and Tunneling Delay Time Measurements in Helium," Science 322 (5907), 1525 (2008)

[35] A. N. Pfeiffer, C. Cirelli, M. Smolarski, R. Dörner, and U. Keller, "Timing the release in sequential double ionization," Nat. Phys. 7 (5), 428 (2011)

[36] D. D. Hickstein, P. Ranitovic, S. Witte, X.-M. Tong, Y. Huismans, P. Arpin, X. Zhou, K. E. Keister, C. W. Hogle, B. Zhang, C. Ding, P. Johnsson, N. Toshima, M. J. J. Vrakking, M. M. Murnane, and H. C. Kapteyn, "Direct Visualization of Laser-Driven Electron Multiple Scattering and Tunneling Distance in Strong-Field Ionization," Phys. Rev. Lett. 109 (7), 073004 (2012)

[37] C. I. Blaga, J. Xu, A. D. DiChiara, E. Sistrunk, K. Zhang, P. Agostini, T. A. Miller, L. F. DiMauro, and C.-D. Lin, "Imaging ultrafast molecular dynamics with laser-induced electron diffraction," Nature 483 (7388), 194 (2012)

[38] A. S. Landsman, M. Weger, J. Maurer, R. Boge, A. Ludwig, S. Heuser, C. Cirelli, L. Gallmann, and U. Keller, "Ultrafast resolution of tunneling delay time," Optica 1 (5), 343 (2014)

[39] W. E. Lamb, "Theory of an Optical Maser," Phys. Rev. 134 (6A), A1429 (1964)

[40] L. E. Hargrove, R. L. Fork, and M. A. Pollack, "Locking of He-Ne Laser Modes Induced by Synchronous Intracavity Modulation," Appl. Phys. Lett. 5 (1), 4 (1964)

[41] D. E. Spence, P. N. Kean, and W. Sibbett, "60-fsec pulse generation from a self-mode-locked Ti:sapphire laser." Opt. Lett. 16 (1), 42 (1991)

[42] U. Keller, G. W. 'tHooft, W. H. Knox, and J. E. Cunningham, "Femtosecond pulses from a continuously self-starting passively mode-locked Ti:sapphire laser," Opt. Lett. 16 (13), 1022 (1991)

[43] U. Keller, D. A. B. Miller, G. D. Boyd, T. H. Chiu, J. F. Ferguson, and M. T. Asom, "Solid-state low-loss intracavity saturable absorber for Nd:YLF lasers: an antiresonant semiconductor Fabry–Perot saturable absorber," Opt. Lett. 17 (7), 505 (1992)

[44] U. Keller, K. J. Weingarten, F. X. Kärtner, D. Kopf, B. Braun, I. D. Jung, R. Fluck, C. Hönninger, N. Matuschek, and J. Aus Der Au, "Semiconductor saturable absorber mirrors (SESAM's) for femtosecond to nanosecond pulse generation in solid-state lasers," IEEE J. Sel. Top. Quantum Electron. 2 (3), 435 (1996)

[45] U. Morgner, F. X. Kärtner, S. H. Cho, Y. Chen, H. a. Haus, J. G. Fujimoto, E. P. Ippen, V. Scheuer, G. Angelow, and T. Tschudi, "Sub-two-cycle pulses from a Kerr-lens mode-locked Ti:sapphire laser." Opt. Lett. 24 (6), 411 (1999)

[46] A. L'Huillier, K. J. Schafer, and K. C. Kulander, "Higher-Order harmonic Generation in Xenon at 1064 nm: The Role of Phase Matching," Phys. Rev. Lett. 66 (17), 2200 (1991)

[47] P. B. Corkum, "Plasma perspective on strong field multiphoton ionization," Phys. Rev. Lett. 71 (13), 1994 (1993)

[48] J. L. Krause, K. Schafer, and K. Kulander, "High-order harmonic generation from atoms and ions in the high intensity regime," Phys. Rev. Lett. 68 (24), 3535 (1992)

[49] T. Pfeifer, L. Gallmann, M. J. Abel, P. M. Nagel, D. M. Neumark, and S. R. Leone, “Heterodyne Mixing of Laser Fields for Temporal Gating of High-Order Harmonic Generation,” Phys. Rev. Lett. 97 (16), 163901 (2006)

[50] M. Lewenstein, P. Balcou, M. Y. Ivanov, A. L’Huillier, and P. B. Corkum, “Theory of high-harmonic generation by low-frequency laser fields,” Phys. Rev. A 49 (3), 2117 (1994)

[51] P. Balcou, P. Salières, A. L’Huillier, and M. Lewenstein, “Generalized phase-matching conditions for high harmonics: The role of field-gradient forces,” Phys. Rev. A 55 (4), 3204 (1997)

[52] P. Salières, A. L’Huillier, and M. Lewenstein, “Coherence Control of High-Order Harmonics,” Phys. Rev. Lett. 74 (19), 3776 (1995)

[53] P. M. Paul, E. S. Toma, P. Breger, G. Mullot, F. Auge, P. Balcou, H. G. Muller, and P. Agostini, “Observation of a train of attosecond pulses from high harmonic generation,” Science 292 (5522), 1689 (2001)

[54] M. Lucchini, J. Herrmann, A. Ludwig, R. Locher, M. Sabbar, L. Gallmann, and U. Keller, “Role of electron wavepacket interference in the optical response of helium atoms,” New J. Phys. 15 (10), 103010 (2013)

[55] M. Hentschel, R. Kienberger, C. Spielmann, G. a. Reider, N. Milosevic, T. Brabec, P. B. Corkum, U. Heinzmann, M. Drescher, and F. Krausz, “Attosecond metrology.” Nature 414 (6863), 509 (2001)

[56] G. Sansone, E. Benedetti, F. Calegari, C. Vozzi, L. Avaldi, R. Flammini, L. Poletto, P. Villoresi, C. Altucci, R. Velotta, S. Stagira, S. De Silvestri, and M. Nisoli, “Isolated Single-Cycle Attosecond Pulses,” Science 314 (5798), 443 (2006)

[57] K. Zhao, Q. Zhang, M. Chini, Y. Wu, X. Wang, and Z. Chang, “Tailoring a 67 attosecond pulse through advantageous,” Opt. Lett. 37 (18), 3891 (2012)

[58] T. Pfeifer, A. Jullien, M. J. Abel, P. M. Nagel, L. Gallmann, D. M. Neumark, and S. R. Leone, “Generating coherent broadband continuum soft-x-ray radiation by attosecond ionization gating,” Opt. Express 15 (25), 17120 (2007)

[59] A. Jullien, T. Pfeifer, M. J. Abel, P. M. Nagel, M. J. Bell, D. M. Neumark, and S. R. Leone, “Ionization phase-match gating for wavelength-tunable isolated attosecond pulse generation,” Appl. Phys. B 93 (2-3), 433 (2008)

[60] J. A. Wheeler, A. Borot, S. Monchocé, H. Vincenti, A. Ricci, A. Malvache, R. Lopez-Martens, and F. Quéré, “Attosecond lighthouses from plasma mirrors,” Nat. Photonics 6 (12), 829 (2012)

[61] H. Vincenti and F. Quéré, “Attosecond Lighthouses: How To Use Spatiotemporally Coupled Light Fields To Generate Isolated Attosecond Pulses,” Phys. Rev. Lett. 108 (11), 113904 (2012)

[62] K. T. Kim, C. Zhang, T. Ruchon, J.-F. Hergott, T. Auguste, D. M. Villeneuve, P. B. Corkum, and F. Quéré, “Photonic streaking of attosecond pulse trains,” Nat. Photonics 7 (8), 651 (2013)

[63] M. Chini, K. Zhao, and Z. Chang, "The generation, characterization and applications of broadband isolated attosecond pulses," Nat. Photonics 8 (3), 178 (2014)

[64] K. S. Budil, P. Salières, M. D. Perry, and A. L'Huillier, "Influence of ellipticity on harmonic generation," Phys. Rev. A 48 (5), 3437 (1993)

[65] F. Calegari, M. Lucchini, M. Negro, C. Vozzi, L. Poletto, O. Svelto, S. De Silvestri, G. Sansone, S. Stagira, and M. Nisoli, "Temporal gating methods for the generation of isolated attosecond pulses," J. Phys. B: At. Mol. Opt. Phys. 45 (7), 074002 (2012)

[66] I. J. Sola, E. Mével, L. Elouga, E. Constant, V. Strelkov, L. Poletto, P. Villoresi, E. Benedetti, J.-P. Caumes, S. Stagira, C. Vozzi, G. Sansone, and M. Nisoli, "Controlling attosecond electron dynamics by phase-stabilized polarization gating," Nat. Phys. 2 (5), 319 (2006)

[67] T. Pfeifer, M. J. Abel, P. M. Nagel, W. Boutu, M. J. Bell, Y. Liu, D. M. Neumark, and S. R. Leone, "Measurement and optimization of isolated attosecond pulse contrast," Opt. Lett. 34 (12), 1819 (2009)

[68] M. Sabbar, S. Heuser, R. Boge, M. Lucchini, L. Gallmann, C. Cirelli, and U. Keller, "Combining attosecond XUV pulses with coincidence spectroscopy." Rev. Sci. Instrum. 85 (10), 103113 (2014)

[69] M. Kitzler, N. Milosevic, A. Scrinzi, F. Krausz, and T. Brabec, "Quantum Theory of Attosecond XUV Pulse Measurement by Laser Dressed Photoionization," Phys. Rev. Lett. 88 (17), 173904 (2002)

[70] J. Itatani, F. Quéré, G. L. Yudin, M. Y. Ivanov, F. Krausz, and P. B. Corkum, "Attosecond Streak Camera," Phys. Rev. Lett. 88 (17), 173903 (2002)

[71] J. Gagnon, Attosecond Electron Spectroscopy - Theory and its Applications, Ph.D. thesis, Ludwig Maximilian University of Munich (2010)

[72] J. Gagnon, E. Goulielmakis, and V. Yakovlev, "The accurate FROG characterization of attosecond pulses from streaking measurements," Appl. Phys. B: Lasers Opt. 92 (1), 25 (2008)

[73] R. Trebino, K. W. DeLong, D. N. Fittinghoff, J. N. Sweetser, M. A. Krumbügel, B. A. Richman, and D. J. Kane, "Measuring ultrashort laser pulses in the time-frequency domain using frequency-resolved optical gating," Rev. Sci. Instrum. 68 (9), 3277 (1997)

[74] Y. Mairesse and F. Quéré, "Frequency-resolved optical gating for complete reconstruction of attosecond bursts," Phys. Rev. A 71, 011401(R) (2005)

[75] D. J. Kane, G. Rodriguez, A. J. Taylor, and T. S. Clement, "Simultaneous measurement of two ultrashort laser pulses from a single spectrogram in a single shot," J. Opt. Soc. Am. B 14 (4), 935 (1997)

[76] D. J. Kane, "Real-time measurement of ultrashort laser pulses using principal component generalized projections," IEEE J. Sel. Top. Quantum Electron. 4 (2), 278 (1998)

[77] D. J. Kane, "Recent progress toward real-time measurement of ultrashort laser pulses," IEEE J. Quantum Electron. 35 (4), 421 (1999)

[78] B. W. Mayer, C. R. Phillips, L. Gallmann, and U. Keller, "Mid-infrared pulse generation via achromatic quasi-phase-matched OPCPA," Opt. Express 22 (17), 20798 (2014)

[79] B. W. Mayer, C. R. Phillips, L. Gallmann, M. M. Fejer, and U. Keller, "Sub-four-cycle laser pulses directly from a high-repetition-rate optical parametric chirped-pulse amplifier at 3.4 um," Opt. Lett. 38 (21), 4265 (2013)

[80] C. R. Phillips, B. W. Mayer, L. Gallmann, and U. Keller, "Frequency-domain nonlinear optics in two-dimensionally patterned quasi-phase-matching media," arXiv (2015)

[81] M. Weger, J. Maurer, A. Ludwig, L. Gallmann, and U. Keller, "Transferring the attoclock technique to velocity map imaging," Opt. Express 21 (19), 21981 (2013)

[82] A. T. J. B. Eppink and D. H. Parker, "Velocity map imaging of ions and electrons using electrostatic lenses: Application in photoelectron and photofragment ion imaging of molecular oxygen," Rev. Sci. Instrum. 68 (9), 3477 (1997)

[83] D. H. Parker and A. T. J. B. Eppink, "Photoelectron and photofragment velocity map imaging of state-selected molecular oxygen dissociation/ionization dynamics," J. Chem. Phys. 107 (7), 2357 (1997)

[84] O. Ghafur, W. Siu, P. Johnsson, M. F. Kling, M. Drescher, and M. J. J. Vrakking, "A velocity map imaging detector with an integrated gas injection system." Rev. Sci. Instrum. 80 (3), 033110 (2009)

[85] C. Smeenk, L. Arissian, A. Staudte, D. M. Villeneuve, and P. B. Corkum, "Momentum space tomographic imaging of photoelectrons," J. Phys. B: At. Mol. Opt. Phys. 42 (18), 185402 (2009)

[86] M. Wollenhaupt, M. Krug, J. Köhler, T. Bayer, C. Sarpe-Tudoran, and T. Baumert, "Three-dimensional tomographic reconstruction of ultrashort free electron wave packets," Appl. Phys. B: Lasers Opt. 95 (4), 647 (2009)

[87] A. C. Kak and M. Slaney, Principles of Computerized Tomographic Imaging, IEEE Press (1988)

[88] R. Boge, C. Cirelli, A. S. Landsman, S. Heuser, A. Ludwig, J. Maurer, M. Weger, L. Gallmann, and U. Keller, "Probing Nonadiabatic Effects in Strong-Field Tunnel Ionization," Phys. Rev. Lett. 111 (10), 103003 (2013)

[89] C. Iaconis and I. A. Walmsley, "Spectral phase interferometry for direct electric-field reconstruction of ultrashort optical pulses," Opt. Lett. 23 (10), 792 (1998)

[90] R. Locher, M. Lucchini, J. Herrmann, M. Sabbar, M. Weger, A. Ludwig, L. Castiglioni, M. Greif, M. Hengsberger, L. Gallmann, and U. Keller, "Versatile attosecond beamline in a two-foci configuration for simultaneous time-resolved measurements," Rev. Sci. Instrum. 85 (1), 013113 (2014)

[91] T. Oksenhendler, S. Coudreau, N. Forget, V. Crozatier, S. Grabielle, R. Herzog, O. Gobert, and D. Kaplan, “Self-referenced spectral interferometry,” Appl. Phys. B 99 (1-2), 7 (2010)

[92] R. López-Martens, K. Varjú, P. Johnsson, J. Mauritsson, Y. Mairesse, P. Salières, M. B. Gaarde, K. J. Schafer, A. Persson, S. Svanberg, C.-G. Wahlström, and A. L’Huillier, “Amplitude and Phase Control of Attosecond Light Pulses,” Phys. Rev. Lett. 94 (3), 033001 (2005)

[93] B. Henke, E. Gullikson, and J. Davis, “X-Ray Interactions: Photoabsorption, Scattering, Transmission, and Reflection at E = 50-30,000 eV, Z = 1-92,” At. Data Nucl. Data Tables 54 (2), 181 (1993)

[94] M. Lucchini, L. Castiglioni, L. Kasmi, P. Kliuiev, A. Ludwig, M. Greif, J. Osterwalder, M. Hengsberger, L. Gallmann, and U. Keller, “Light-Matter Interaction at Surfaces in the Spatiotemporal Limit of Macroscopic Models,” Phys. Rev. Lett. 115 (13), 137401 (2015)

[95] A. Ludwig, J. Maurer, B. W. Mayer, C. R. Phillips, L. Gallmann, and U. Keller, “Breakdown of the Dipole Approximation in Strong-Field Ionization,” Phys. Rev. Lett. 113 (24), 243001 (2014)

[96] D. B. Milosević, G. G. Paulus, D. Bauer, and W. Becker, “Above-threshold ionization by few-cycle pulses,” J. Phys. B: At. Mol. Opt. Phys. 39 (14), 203 (2006)

[97] S. Palaniyappan, I. Ghebregziabher, A. DiChiara, J. MacDonald, and B. C. Walker, “Emergence from nonrelativistic strong-field rescattering to ultrastrong-field laser-atom physics: A semiclassical analysis,” Phys. Rev. A 74 (3), 033403 (2006)

[98] C. J. Joachain, N. J. Kylstra, and R. M. Potvliege, Atoms in Intense Laser Fields, Cambridge University Press (2012)

[99] A. D. DiChiara, I. Ghebregziabher, J. M. Waesche, T. Stanev, N. Ekanayake, L. R. Barclay, S. J. Wells, A. Watts, M. Videtto, C. a. Mancuso, and B. C. Walker, “Photoionization by an ultraintense laser field: Response of atomic xenon,” Phys. Rev. A 81 (4), 043417 (2010)

[100] E. A. Chowdhury and B. C. Walker, “Multielectron ionization processes in ultrastrong laser fields,” J. Opt. Soc. Am. B 20 (1), 109 (2003)

[101] S. Palaniyappan, A. DiChiara, E. Chowdhury, A. Falkowski, G. Ongadi, E. L. Huskins, and B. C. Walker, “Ultrastrong Field Ionization of Neˆn+ (n<=8): Rescattering and the Role of the Magnetic Field,” Phys. Rev. Lett. 94 (24), 243003 (2005)

[102] C. Moore, J. Knauer, and D. Meyerhofer, “Observation of the transition from Thomson to Compton scattering in multiphoton interactions with low-energy electrons,” Phys. Rev. Lett. 74 (13), 2439 (1995)

[103] D. D. Meyerhofer, J. P. Knauer, S. J. McNaught, and C. I. Moore, “Observation of relativistic mass shift effects during high-intensity laser–electron interactions,” J. Opt. Soc. Am. B 13 (1), 113 (1996)

[104] M. Førre, J. Hansen, L. Kocbach, S. Selstø, and L. B. Madsen, “Nondipole Ionization Dynamics of Atoms in Superintense High-Frequency Attosecond Pulses,” Phys. Rev. Lett. 97 (4), 043601 (2006)

[105] M. Klaiber, K. Z. Hatsagortsyan, and C. H. Keitel, “Relativistic ionization rescattering with tailored laser pulses,” Phys. Rev. A 74 (5), 051803 (2006)

[106] C. C. Chirilă, N. J. Kylstra, R. M. Potvliege, and C. J. Joachain, “Nondipole effects in photon emission by laser-driven ions,” Phys. Rev. A 66 (6), 063411 (2002)

[107] M. W. Walser, C. H. Keitel, A. Scrinzi, and T. Brabec, “High harmonic generation beyond the electric dipole approximation,” Phys. Rev. Lett. 85 (24), 5082 (2000)

[108] S. Hu and C. Keitel, “Dynamics of multiply charged ions in intense laser fields,” Phys. Rev. A 63 (5), 053402 (2001)

[109] A. S. Titi and G. W. F. Drake, “Quantum theory of longitudinal momentum transfer in above-threshold ionization,” Phys. Rev. A 85 (4), 041404 (2012)

[110] M. Meckel, D. Comtois, D. Zeidler, A. Staudte, D. Pavicic, H. C. Bandulet, H. Pepin, J. C. Kieffer, R. Dörner, D. M. Villeneuve, P. B. Corkum, and H. Pépin, “Laser-induced electron tunneling and diffraction,” Science 320 (5882), 1478 (2008)

[111] T. Nubbemeyer, K. Gorling, A. Saenz, U. Eichmann, and W. Sandner, “Strong-Field Tunneling without Ionization,” Phys. Rev. Lett. 101 (23), 233001 (2008)

[112] U. Eichmann, A. Saenz, S. Eilzer, T. Nubbemeyer, and W. Sandner, “Observing Rydberg Atoms to Survive Intense Laser Fields,” Phys. Rev. Lett. 110 (20), 203002 (2013)

[113] T. F. Gallagher, “Rydberg atoms,” Reports Prog. Phys. 51 (2), 143 (1988)

[114] T. F. Gallagher, “Above-Threshold Ionization in Low-Frequency Limit,” Phys. Rev. Lett. 61 (20), 2304 (1988)

[115] K. C. Kulander, K. J. Schafer, and J. L. Krause, “Proceedings of the Workshop, Super Intense Laser Atom Physics (SILAP) III,” in B. Piraux (Editor), Super-Intense Laser-Atom Phys., 95–110, Plenum Press, New York (1993)

[116] H. B. van Linden van den Heuvell and H. G. Muller, “Limiting cases of excess-photon ionization,” in S. Smith and P. Knight (Editors), Multiphot. Process., 25–34, Cambridge University Press, Cambridge (1989)

[117] L.-B. Fu, J. Liu, J. Chen, and S.-G. Chen, “Classical collisional trajectories as the source of strong-field double ionization of helium in the knee regime,” Phys. Rev. A 63 (4), 043416 (2001)

[118] A. N. Pfeiffer, C. Cirelli, M. Smolarski, D. Dimitrovski, M. Abu-samha, L. B. Madsen, and U. Keller, “Attoclock reveals natural coordinates of the laser-induced tunnelling current flow in atoms,” Nat. Phys. 8 (1), 76 (2012)

[119] M. V. Ammosov, N. B. Delone, and V. P. Krainov, "Tunnel ionization of complex atoms and of atomic ions in an alternating electromagnetic field," Sov. Phys. JETP 64 (6), 1191 (1986)

[120] N. B. Delone and V. P. Krainov, "Energy and angular electron spectra for the tunnel ionization of atoms by strong low-frequency radiation," J. Opt. Soc. Am. B 8 (6), 1207 (1991)

[121] X. M. Tong and C. D. Lin, "Empirical formula for static field ionization rates of atoms and molecules by lasers in the barrier-suppression regime," J. Phys. B: At. Mol. Opt. Phys. 38 (15), 2593 (2005)

[122] M. Klaiber, E. Yakaboylu, H. Bauke, K. Z. Hatsagortsyan, and C. H. Keitel, "Under-the-Barrier Dynamics in Laser-Induced Relativistic Tunneling," Phys. Rev. Lett. 110 (15), 153004 (2013)

[123] E. Yakaboylu, M. Klaiber, H. Bauke, K. Z. Hatsagortsyan, and C. H. Keitel, "Relativistic features and time delay of laser-induced tunnel ionization," Phys. Rev. A 88 (6), 063421 (2013)

[124] N. Milosevic, V. P. Krainov, and T. Brabec, "Semiclassical Dirac Theory of Tunnel Ionization," Phys. Rev. Lett. 89 (19), 193001 (2002)

[125] N. I. Shvetsov-Shilovski, D. Dimitrovski, and L. B. Madsen, "Ionization in elliptically polarized pulses: Multielectron polarization effects and asymmetry of photoelectron momentum distributions," Phys. Rev. A 85 (2), 023428 (2012)

[126] N. I. Shvetsov-Shilovski, S. P. Goreslavski, S. V. Popruzhenko, and W. Becker, "Capture into rydberg states and momentum distributions of ionized electrons," Laser Phys. 19 (8), 1550 (2009)

[127] J. Maurer, A. Ludwig, B. Mayer, C. R. Phillips, L. Gallmann, and U. Keller, "Breakdown of the dipole approximation in strong field ionization," in Conf. Ultrafast Dyn. Imaging Matter (2015)

[128] S. Chelkowski, A. D. Bandrauk, and P. B. Corkum, "Photon-momentum transfer in multiphoton ionization and in time-resolved holography with photoelectrons," Phys. Rev. A 92 (5), 051401 (2015)

[129] M. Lucchini, M. Brügmann, A. Ludwig, L. Gallmann, U. Keller, and T. Feurer, "Ptychographic reconstruction of attosecond pulses," Opt. Express 23 (23), 29502 (2015)

[130] W. Hoppe, "Beugung im Inhomogenen Primärstrahlwellenfeld. I. Prinzip einer Phasenmessung von Elektronenbeugungsinterferenzen," Acta Crystallogr. Sect. A 25 (4), 495 (1969)

[131] J. M. Rodenburg, A. Hurst, and A. Cullis, "Transmission microscopy without lenses for objects of unlimited size," Ultramicroscopy 107 (2-3), 227 (2007)

[132] B. C. McCallum and J. M. Rodenburg, "Two-dimensional demonstration of Wigner phase-retrieval microscopy in the STEM configuration," Ultramicroscopy 45 (3-4), 371 (1992)

[133] P. Thibault, M. Dierolf, O. Bunk, A. Menzel, and F. Pfeiffer, “Probe retrieval in ptychographic coherent diffractive imaging,” Ultramicroscopy 109 (4), 338 (2009)

[134] A. M. Maiden and J. M. Rodenburg, “An improved ptychographical phase retrieval algorithm for diffractive imaging,” Ultramicroscopy 109 (10), 1256 (2009)

[135] A. Godil, B. Auld, and D. Bloom, “Picosecond time-lenses,” IEEE J. Quantum Electron. 30 (3), 827 (1994)

[136] D. Spangenberg, P. Neethling, E. Rohwer, M. H. Brügmann, and T. Feurer, “Time-domain ptychography,” Phys. Rev. A 91 (2), 021803 (2015)

[137] D. Spangenberg, E. Rohwer, M. H. Brügmann, and T. Feurer, “Ptychographic ultrafast pulse reconstruction,” Opt. Lett. 40 (6), 1002 (2015)

[138] R. Boge, S. Heuser, M. Sabbar, M. Lucchini, L. Gallmann, C. Cirelli, and U. Keller, “Revealing the time-dependent polarization of ultrashort pulses with sub-cycle resolution,” Opt. Express 22 (22), 26967 (2014)

[139] M. Chini, S. Gilbertson, S. D. Khan, and Z. Chang, “Characterizing ultrabroadband attosecond lasers,” Opt. Express 18 (12), 13006 (2010)

[140] J. Gagnon and V. S. Yakovlev, “The robustness of attosecond streaking measurements,” Opt. Express 17 (20), 17678 (2009)

[141] M. Lucchini, A. Ludwig, T. Zimmermann, L. Kasmi, J. Herrmann, A. Scrinzi, A. S. Landsman, L. Gallmann, and U. Keller, “Anisotropic emission in quantum-beat spectroscopy of helium excited states,” Phys. Rev. A 91 (6), 063406 (2015)

[142] R. T. Carter and J. R. Huber, “Quantum beat spectroscopy in chemistry,” Chem. Soc. Rev. 29 (5), 305 (2000)

[143] P. Cörlin, A. Fischer, M. Schönwald, A. Sperl, T. Mizuno, U. Thumm, T. Pfeifer, and R. Moshammer, “Probing calculated O2+ potential-energy curves with an XUV-IR pump-probe experiment,” Phys. Rev. A 91 (4), 043415 (2015)

[144] N. Shivaram, H. Timmers, X.-M. Tong, and A. Sandhu, “Attosecond Quantum Beat Spectroscopy,” in Front. Opt. 2014, LW5H.4, Optical Society of America (2014)

[145] F. Krausz and M. Y. Ivanov, “Attosecond physics,” Rev. Mod. Phys. 81 (1), 163 (2009)

[146] G. Sansone, L. Poletto, and M. Nisoli, “High-energy attosecond light sources,” Nat. Photonics 5, 655 (2011)

[147] L. Gallmann, C. Cirelli, and U. Keller, “Attosecond science: recent highlights and future trends,” Annu. Rev. Phys. Chem. 63 (1), 447 (2012)

[148] L. Gallmann, J. Herrmann, R. Locher, M. Sabbar, A. Ludwig, M. Lucchini, and U. Keller, “Resolving intra-atomic electron dynamics with attosecond transient absorption spectroscopy,” Mol. Phys. 111 (14-15), 2243 (2013)

[149] C. Ott, A. Kaldun, P. Raith, K. Meyer, M. Laux, J. Evers, C. H. Keitel, C. H. Greene, and T. Pfeifer, "Lorentz Meets Fano in Spectral Line Shapes: A Universal Phase and Its Laser Control," Science 340 (6133), 716 (2013)

[150] A. Kaldun, C. Ott, A. Blättermann, M. Laux, K. Meyer, T. Ding, A. Fischer, and T. Pfeifer, "Extracting Phase and Amplitude Modifications of Laser-Coupled Fano Resonances," Phys. Rev. Lett. 112 (10), 103001 (2014)

[151] M. Chini, X. Wang, Y. Cheng, and Z. Chang, "Resonance effects and quantum beats in attosecond transient absorption of helium," J. Phys. B: At. Mol. Opt. Phys. 47 (12), 124009 (2014)

[152] A. R. Beck, B. Bernhardt, E. R. Warrick, M. Wu, S. Chen, M. B. Gaarde, K. J. Schafer, D. M. Neumark, and S. R. Leone, "Attosecond transient absorption probing of electronic superpositions of bound states in neon: detection of quantum beats," New J. Phys. 16 (11), 113016 (2014)

[153] M. Chini, B. Zhao, H. Wang, Y. Cheng, S. X. Hu, and Z. Chang, "Subcycle ac Stark Shift of Helium Excited States Probed with Isolated Attosecond Pulses," Phys. Rev. Lett. 109 (7), 073601 (2012)

[154] S. Chen, M. J. Bell, A. R. Beck, H. Mashiko, M. Wu, A. N. Pfeiffer, M. B. Gaarde, D. M. Neumark, S. R. Leone, and K. J. Schafer, "Light-induced states in attosecond transient absorption spectra of laser-dressed helium," Phys. Rev. A 86 (6), 063408 (2012)

[155] M. Chini, X. Wang, Y. Cheng, Y. Wu, D. Zhao, D. a. Telnov, S.-I. Chu, and Z. Chang, "Sub-cycle Oscillations in Virtual States Brought to Light," Sci. Rep. 3, 1105 (2013)

[156] P. Ranitovic, X. M. Tong, C. W. Hogle, X. Zhou, Y. Liu, N. Toshima, M. M. Murnane, and H. C. Kapteyn, "Controlling the XUV Transparency of Helium Using Two-Pathway Quantum Interference," Phys. Rev. Lett. 106 (19), 193008 (2011)

[157] P. Ranitovic, X. M. Tong, B. Gramkow, S. De Camillis, B. DePaola, K. P. Singh, W. Cao, M. Magrakvelidze, D. Ray, I. Bocharova, H. Mashiko, A. Sandhu, E. Gagnon, M. M. Murnane, H. C. Kapteyn, I. Litvinyuk, and C. L. Cocke, "IR-assisted ionization of helium by attosecond extreme ultraviolet radiation," New J. Phys. 12 (1), 13008 (2010)

[158] H. R. Telle, G. Steinmeyer, A. E. Dunlop, J. Stenger, D. H. Sutter, and U. Keller, "Carrier-envelope offset phase control: A novel concept for absolute optical frequency measurement and ultrashort pulse generation," Appl. Phys. B: Lasers Opt. 69 (4), 327 (1999)

[159] E. T. Jaynes, "Quantum Beats," in A. O. Barut (Editor), Found. Radiat. Theory Quantum Electrodyn., 37–43, Springer US, Boston, MA (1980)

[160] J. A. Yeazell and C. R. Stroud Jr., "Observation of spatially localized atomic electron wave packets," Phys. Rev. Lett. 60 (15), 1494 (1988)

[161] A. ten Wolde, L. D. Noordam, A. Lagendijk, and H. B. van Linden van den Heuvell, "Observation of Radially Localized Atomic Electron Wave Packets," Phys. Rev. Lett. 61 (18), 2099 (1988)

[162] M. Wollenhaupt, A. Assion, D. Liese, C. Sarpe-Tudoran, T. Baumert, S. Zamith, M. A. Bouchene, B. Girard, A. Flettner, U. Weichmann, and G. Gerber, "Interferences of Ultrashort Free Electron Wave Packets," Phys. Rev. Lett. 89 (17), 173001 (2002)

[163] K. Klünder, P. Johnsson, M. Swoboda, A. L'Huillier, G. Sansone, M. Nisoli, M. J. J. Vrakking, K. J. Schafer, J. Mauritsson, and A. L'Huillier, "Reconstruction of attosecond electron wave packets using quantum state holography," Phys. Rev. A 88 (3), 033404 (2013)

[164] N. N. Choi, T. F. Jiang, T. Morishita, M.-H. Lee, and C. D. Lin, "Theory of probing attosecond electron wave packets via two-path interference of angle-resolved photoelectrons," Phys. Rev. A 82 (1), 013409 (2010)

[165] H. Geiseler, H. Rottke, G. Steinmeyer, and W. Sandner, "Quantum beat oscillations in the two-color-photoionization continuum of neon and their dependence on the intensity of the ionizing laser pulse," Phys. Rev. A 84 (3), 033424 (2011)

[166] L. Tao and A. Scrinzi, "Photo-electron momentum spectra from minimal volumes: the time-dependent surface flux method," New J. Phys. 14 (1), 13021 (2012)

[167] V. P. Majety, A. Zielinski, A. Swoboda, and A. Scrinzi, "tRecX - A universal Schrödinger and Maxwell solver," The tRecX Homepage (2015)

[168] H. G. Muller, "Reconstruction of attosecond harmonic beating by interference of two-photon transitions," Appl. Phys. B: Lasers Opt. 74 (9), s17 (2002)

[169] H. Katsuki, H. Chiba, C. Meier, B. Girard, and K. Ohmori, "Wave packet interferometry with attosecond precision and picometric structure," Phys. Chem. Chem. Phys. 12 (20), 5189 (2010)

[170] R. Gonzalez-Luque, M. Garavelli, F. Bernardi, M. Merchan, M. A. Robb, and M. Olivucci, "Computational evidence in favor of a two-state, two-mode model of the retinal chromophore photoisomerization," Proc. Natl. Acad. Sci. 97 (17), 9379 (2000)

[171] D. Polli, P. Altoè, O. Weingart, K. M. Spillane, C. Manzoni, D. Brida, G. Tomasello, G. Orlandi, P. Kukura, R. A. Mathies, M. Garavelli, and G. Cerullo, "Conical intersection dynamics of the primary photoisomerization event in vision," Nature 467 (7314), 440 (2010)

[172] J. C. Lorquet, C. Sannen, and G. Raşeev, "Dissociation of the Ethylene Cation: Mechanism of Energy Randomization," J. Am. Chem. Soc. 102, 7976 (1980)

[173] C. Sannen, G. Raşeev, C. Galley, G. Fauville, and J. C. Lorquet, "Unimolecular decay paths of electronically excited species. II. The C2H4+ ion," J. Chem. Phys. 74 (4), 2402 (1981)

[174] P. Farmanara, V. Stert, and W. Radloff, "Ultrafast internal conversion and fragmentation in electronically excited C2H4 and C2H3Cl molecules," Chem. Phys. Lett. 288, 518 (1998)

[175] H. Tao, T. K. Allison, T. W. Wright, A. M. Stooke, C. Khurmi, J. van Tilborg, Y. Liu, R. W. Falcone, A. Belkacem, and T. J. Martinez, “Ultrafast internal conversion in ethylene. I. The excited state lifetime,” J. Chem. Phys. 134 (24), 244306 (2011)

[176] M. Ben-Nun and T. J. Martínez, “Ab initio molecular dynamics study of cis–trans photoisomerization in ethylene,” Chem. Phys. Lett. 298 (1-3), 57 (1998)

[177] T. J. Martínez, “Insights for light-driven molecular devices from ab initio multiple spawning excited-state dynamics of organic and biological chromophores,” Acc. Chem. Res. 39 (2), 119 (2006)

[178] B. G. Levine and T. J. Martínez, “Isomerization Through Conical Intersections,” Annu. Rev. Phys. Chem. 58 (1), 613 (2007)

[179] B. Joalland, T. Mori, T. J. Martínez, and A. G. Suits, “Photochemical Dynamics of Ethylene Cation C2H4+,” J. Phys. Chem. Lett. 5 (8), 1467 (2014)

[180] M. H. Kim, B. D. Leskiw, L. Shen, and A. G. Suits, “Vibrationally Mediated Photodissociation of C2H4+,” J. Phys. Chem. A 111 (31), 7472 (2007)

[181] M. H. Kim, B. D. Leskiw, and A. G. Suits, “Vibrationally Mediated Photodissociation of Ethylene Cation by Reflectron Multimass Velocity Map Imaging,” J. Phys. Chem. A 109 (35), 7839 (2005)

[182] K. Kosma, S. A. Trushin, W. Fuss, and W. E. Schmid, “Ultrafast Dynamics and Coherent Oscillations in Ethylene and Ethylene- d 4 Excited at 162 nm,” J. Phys. Chem. A 112 (33), 7514 (2008)

[183] T. K. Allison, H. Tao, W. J. Glover, T. W. Wright, A. M. Stooke, C. Khurmi, J. van Tilborg, Y. Liu, R. W. Falcone, T. J. Martínez, and A. Belkacem, “Ultrafast internal conversion in ethylene. II. Mechanisms and pathways for quenching and hydrogen elimination,” J. Chem. Phys. 136 (12), 124317 (2012)

[184] J. V. Tilborg, T. K. Allison, T. W. Wright, M. P. Hertlein, R. W. Falcone, Y. Liu, H. Merdji, and A. Belkacem, “Femtosecond isomerization dynamics in the ethylene cation measured in an EUV-pump NIR-probe configuration,” J. Phys. B: At. Mol. Opt. Phys. 42 (8), 081002 (2009)

[185] R. A. Mackie, S. W. J. Scully, A. M. Sands, R. Browning, K. F. Dunn, and C. J. Latimer, “A photoionization mass spectrometric study of acetylene and ethylene in the VUV spectral region,” Int. J. Mass Spectrom. 223-224, 67 (2003)

[186] T. Ibuki, G. Cooper, and C. Brion, “Absolute dipole oscillator strengths for photoabsorption and the molecular and dissociative photoionization of ethylene,” Chem. Phys. 129 (3), 295 (1989)

[187] J. Berkowitz, “Absolute Partial Cross-Sections of Ethylene (C2H4),” in At. Mol. Photoabs., 442–458, Elsevier, Amsterdam (2015)

[188] J. Herrmann, M. Lucchini, S. Chen, M. Wu, A. Ludwig, L. Kasmi, K. J. Schafer, L. Gallmann, M. B. Gaarde, and U. Keller, “Multiphoton transitions for delay-zero calibration in attosecond spectroscopy,” New J. Phys. 17 (1), 013007 (2015)

[189] Y. Kalambet, Y. Kozmin, K. Mikhailova, I. Nagaev, and P. Tikhonov, “Reconstruction of chromatographic peaks using the exponentially modified Gaussian function,” J. Chemom. 25 (7), 352 (2011)

[190] E. Tapavicza, I. Tavernelli, U. Rothlisberger, C. Filippi, and M. E. Casida, “Mixed time-dependent density-functional theory/classical trajectory surface hopping study of oxirane photochemistry,” J. Chem. Phys. 129 (12), 124108 (2008)

[191] T. Mori, W. J. Glover, M. S. Schuurman, and T. J. Martínez, “Role of Rydberg states in the photochemical dynamics of ethylene,” J. Phys. Chem. A 116 (11), 2808 (2012)

[192] P. Ranitovic, C. W. Hogle, P. Riviere, A. Palacios, X.-M. Tong, N. Toshima, A. Gonzalez-Castrillo, L. Martin, F. Martin, M. M. Murnane, and H. Kapteyn, “Attosecond vacuum UV coherent control of molecular dynamics,” Proc. Natl. Acad. Sci. 111 (3), 912 (2014)

[193] S. Hädrich, A. Klenke, J. Rothhardt, M. Krebs, A. Hoffmann, O. Pronin, V. Pervak, J. Limpert, and A. Tünnermann, “High photon flux table-top coherent extreme-ultraviolet source,” Nat. Photonics 8 (10), 779 (2014)

[194] F. Emaury, A. Diebold, C. J. Saraceno, and U. Keller, “Compact extreme ultraviolet source at megahertz pulse repetition rate with a low-noise ultrafast thin-disk laser oscillator,” Optica 2 (11), 980 (2015)

Acknowledgements

I would like to express my gratitude to all the people I have been working with and who supported and encouraged me during the years of my PhD:

Ursula Keller, for giving me the opportunity to pursue my PhD studies in her group, for providing an excellent environment for research, for her trust in me and the freedom she granted.

Thomas Pfeifer, for being co-examiner of my PhD thesis and coming all the way to Zürich for the thesis defense.

Lukas Gallmann, for the supervision and support, as well as for the patience with corrections of scientific publications.

Our collaborators in different projects: Michael Brügmann, Thomas Feurer, Elisa Liberatore, and Ursula Röthlisberger.

Sandra Schmid, the good soul who keeps the group up and running, for all her support concerning administrative challenges.

The D-PHYS services and workshop team, namely Marcel Baer, Andi Stuker, Bernhard Morath, Hansruedi Scherrer, Sandro Tiegermann, Martin Klöckner, Isabelle Altorfer, and Pierrot Dekumbis, for all the precision mechanical components, glued optics, plumbing support and the gas bottle supply. Christian Herzog and his team from the ISG, for their help on IT-related issues during my time as software administrator of the ULP group.

Matteo, for driving the attoline activities for the past four years, for pushing so many projects at the same time, and for sharing all kinds of ideas. I learned a lot. Sadly, my teaching efforts regarding German and being on time for lunch did somehow not get through.

Jochen, for introducing me to the secrets of velocity map imaging and tomography as well as for all the “Floffs” in the lab.

Bene, for keeping up and running the mid-IR OPCPA. You built our workhorse. We just added an expensive remote control to switch it off.

The attoline team, for sharing intense moments in (fighting against the laser and vacuum leaks) and outside of the labs: Matthias W. (great hikes in the mountains), Reto (the fastest on the slopes), Mazyar (Mr. Filament), Jens (Marburg crew), Lamia (team E11, English grammar, Nordbrücke), Misha (intense debates), and Fabian (my successor in the lab and HPS).

All colleagues from the strong-field and attoscience team: Claudio (1001 tartufis), Sasha, Robert (in bricolage we trust), Sebastian, Cornelia, Tomáš, Jannie (careful with CO!), Laura, and Benni (may the H be with you).

All other current and former members of the ULP group: Matthias G., Mathias S., Hiro, Clemens, Vali, Clara, Oli, Wolfgang, Chrigu, Bauke, Alexander, Cinia, Mario, Florian, Chris, Sandro, Aline, Andreas, Dominik, Cesare, Nico, Michael, Ivan, and Justas.

It was a pleasure working with you in the ULP group. We had a lot of fun in and around the labs, during the windsurfing and skiing weekends, and at all the Friday after-work beer occasions and barbecues. I wish you all the best for your time at ETH and beyond!

Special thanks goes to my family and friends, for all their support and faith in me throughout my time in Marburg, Grenoble and Zürich.

Last, but not least, I want to thank Judith, for moving with me to Zürich, for all support during the highs and lows of my PhD, and for distracting my thoughts in the spare time by sharing my enthusiasm for the mountains.

André

Zürich, January 2016